Seismic characterisation of fracture networks

From a wave-cut platform to an active volcano

By

Thomas Loriaux

School of Earth Sciences
University of Bristol

A dissertation submitted to the University of Bristol in accordance with the requirements of the degree of Doctor of Philosophy in the Faculty of Science.

March 2019

Word count: thirty-five thousand

This project has received funding from the European Union's Horizon 2020 research and innovation programme under the Marie Sklodowska-Curie grant agreement No 642029.

Horizon 2020 - Marie Sklodowska-Curie Actions
Innovative Training Network (ITN)
***C**omplex **RhE**ologies in **E**arth dynamics and industrial **P**rocesses*

Acknowledgements

This part of the thesis was maybe the easiest one I had to write, but definitely not the less important one, and maybe the first (and only) lines that most of the people will ever read.

First, I would like to thank Mike and James, whose supervision throughout these three years has been really appreciated (and very much needed). They allowed me to make this project mine and were always source of useful comments and feedbacks. I'm also very grateful to Berhe for providing me with the dataset from Nabro and JV who's help with the modelling was crucial. Precious help was also provided by Alan, who particularly allowed me to put Gander on the map of the world, along with some pubs on the map of Bristol. I would like to thank Sarah for her help, especially for sorting everything out during the intense last months of this PhD. I would also like to thank my APM panel, Max Werner and Nick Teanby for their helpful comments of my work.

I would like to thank Andrea Tomasi for setting up this entertaining ITN project and all the CREEPers for the constructive meeting and the endless table tennis games. I'm grateful to Phil Meredith, Nicolas Brantut and Emmanuel David from UCL, as well as Snorri Gudbrandsson from Reykjavik Geothermal, who welcomed me for a few weeks.

I'm also very grateful to the entire Bristol Geophysics Group. I enjoyed every single one of the 725 coffee breaks I took part to, as well as the countless biscuits, chocolates (and even cheese) I have been eating during this period, including some bizarre specimens. Special thanks go to Anna I, Mike, JV, Anthony (twice), Tesfaye, Anna II, and Jack, who all joined and helped me on the field. I hope you enjoyed the lovely days spent at the Lilstock beach.

Je voudrais aussi remercier mes parents, qui ont bravé la Manche, la météo britannique et le chocolat à la menthe pour me rendre visite à plusieurs reprises pendant mon séjour à Bristol.

And, last but certainly not least, my biggest thanks go to the one who became my wife during this PhD. She is the one who initially encouraged me to apply to this project. She is the one who continuously pushed me forward. She is the one who waited for me to be done. She is the one.

Author's declaration

I declare that the work in this dissertation was carried out in accordance with the requirements of the University's Regulations and Code of Practice for Research Degree Programmes and that it has not been submitted for any other academic award. Except where indicated by specific reference in the text, the work is the candidate's own work. Work done in collaboration with, or with the assistance of, others, is indicated as such. Any views expressed in the dissertation are those of the author.

SIGNED: ..... DATE: .....

Abstract

Fractures play a major role in reservoir exploitation, as they act as natural pathways for fluid flow in the subsurface. They also change the rheology of rocks, generally weakening them. Knowledge of their geometrical characteristics, as well as their connectivity and fluid fill attributes are key parameters in describing fracture systems. Seismic methods can be used to characterise fractures. For example, aligned fractures are very effective in generating seismic anisotropy in a medium, where elastic wave velocities vary as a function of direction of propagation. Such anisotropy is controlled by the compliance of the fracture, which can be decomposed into normal and tangential components, Z_N and Z_T, respectively. As the compliance of a fracture set depends on the fluid fill properties, as well as the connectivity, the fracture compliance ratio, Z_N/Z_T , is a good indicator of fracture fluid properties. In this thesis, seismic anisotropy is used to characterise fracture networks and quantify Z_N/Z_T in two different settings.

In the first study, seismic velocities are measured as a function of azimuth, at Lilstock, in South West England. Here a wave-cut platform of the Blue Lias sequence of limestone and shale is saturated and drained by the tide, which makes it an ideal location to study time lapse effects due to fluid saturation. A drone is used to characterise the exposed fracture patterns showing a clear E-W set of dominant fractures, but also spatial variations in secondary fracture sets. The measured pattern of seismic anisotropy is consistent with the preferred E-W orientation of the fractures. Seismic velocities increase as the tide retreats, primary due to the reduction in density of the fractured rock. Variations of Z_N/Z_T from 0.18 to 0.40 and 0.48 are observed over three surveys, mainly due to a drop of Z_T. These variations are attributed to a decrease in the water content of the main fracture set as the tide retreats.

The second study uses earthquakes recorded by a temporary array of seismometers deployed following the 12 June 2011 eruption of the Nabro volcano in Eritrea. This was one of the largest volcanic eruptions in the last decade. High b-values are calculated, suggesting the presence of a dense fracture network rich in fluids. Shear-wave splitting measurements highlight an overall trend of the fast shear wave polarisation, ϕ, in the NW-SE direction, parallel to the regional maximum horizontal stress. However, a migration of ϕ from E-W to NW-SE is observed over time. These results are attributed to the presence of two orthogonally oriented sets of fracture, one being activated by the eruption. Delay times between the fast of the slow shear waves, δt, shows that the anisotropy is localised to the upper three kilometres below the surface. Variations in the fracture compliance ratio are also determined from the splitting

parameters. Z_N/Z_T of the eruption-induced fracture set decreases as a function of time. This is attributed to the fracture set closing and becoming less connected as the fluid pressure is reduced in the hydrothermal/magmatic system. These results show the potential of shear-wave splitting measurements as a tool for monitoring volcanic unrest. Furthermore, Nabro volcano is a promising geothermal reservoir in Eritrea, and fracture characterisation provides a means to investigate such potential in a geothermal system.

Table of Contents

List of Tables

Table **Page**

List of Figures

Figure **Page**

List of symbols

Symbol	Definition
σ	Stress tensor
ϵ	Strain tensor
$\mathbf{C}$	Stiffness tensor
$\mathbf{S}$	Compliance tensor
λ	First Lamé parameter
μ	Second Lamé parameter
v_p	*P*-wave velocity
v_s	*S*-wave velocity
ρ	Density
ε	First Thomsen's parameter
γ	Second Thomsen's parameter
δ	Third Thomsen's parameter
E	Young's modulus
ν	Poisson's ratio
μ	Shear modulus
$[u]$	Displacement discontinuity
Z_N	Normal fracture compliance
Z_T	Tangential fracture compliance
Z_N/Z_T	Fracture compliance ratio
B_N	Normal compliance of an individual fracture
B_T	Tangential compliance of an individual fracture
l	Fracture spacing
ϕ	Fast *S*-wave polarisation
δt	Time delay between fast and slow *S*-waves
ξ	Fracture density
P_{21}	Fracture intensity
L	Fracture length
h	Anisotropic normalising factor

CHAPTER 1

Introduction

Seismic methods provide a powerful approach to image fractures in the subsurface in a non-invasive manner. In this thesis, I explore the effects of fractures on seismic properties in two distinct settings. This introductory chapter first defines the concept of cracks, fractures and fracture sets. Their importance in the Earth's shallow crust is highlighted, including their effects on permeability, as well as the effective strength and elasticity of the rock. Finally, the main objectives of this thesis are presented.

1.1 Fractures in rock

A fracture is *"a surface in a material across which there is a loss of continuity, cohesion and, therefore, strength"* (van der Pluijm and Marshak, 2004). Fractures can be defined as mechanical breaks due to strain forming in response to an applied stress, and can be described as poorly bonded interfaces. These discontinuities take multiple forms and a single fracture can be described in many ways (Figure 1.1).

The generic term *'fracture'* contains various sub-categories of brittle discontinuities, with different origins and characteristics. The term *'crack'* is also used, particularly in the engineering

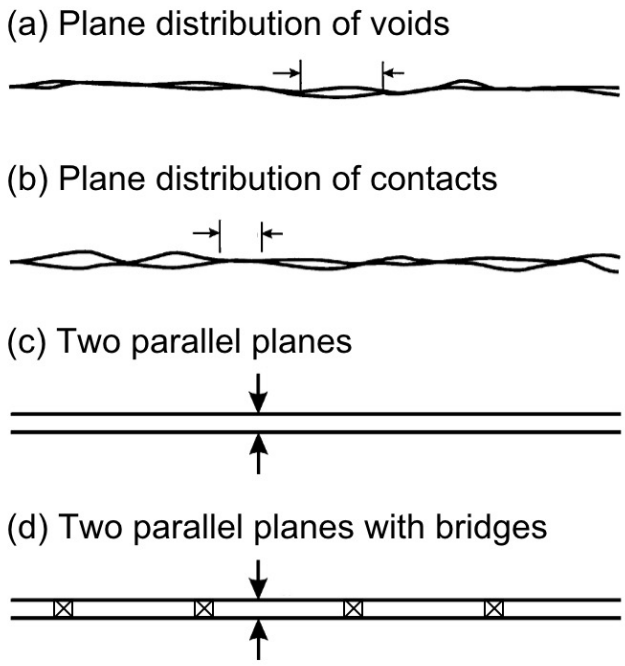

Figure 1.1 Different approaches to represent fractures. Modified from Hudson and Liu (1999) and Sayers et al. (2009).

literature. It does not characterise the mechanical origin of the discontinuity and is sometimes used to refer to small fractures.

The two most abundant fracture types in nature are joints and faults (Figure 1.2; Liu and Martinez, 2013). Joints form in extension or opening mode (Pollard and Aydin, 1988), the planes being pulled apart from each other, with no shear displacement. They generally occur in sets, made of parallel and evenly spaced joints. Multiple sets are often present, forming a joint system. They are a primary mechanism for fluid transport within fractured reservoirs. They also enhance the porosity of rock (i.e., secondary porosity). Due to their role as natural pathway for fluid migration, mineralisation can occur between the joint faces. Fractures that are completely mineralised are called veins (Peacock et al., 2016), and show extremely low permeability.

Faults show shear displacement (Price, 1966). They occur either in clusters or isolated over

a wide range of length scales. Fault tends to not enhance rock permeability as much as joints, and can even form a barrier for fluid flow.

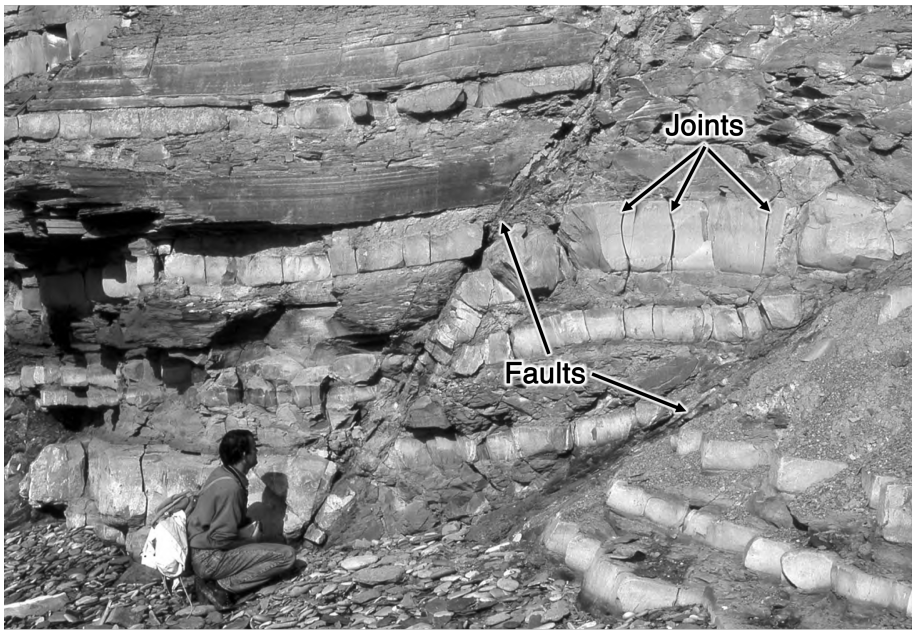

Figure 1.2 Joints and fault at Lilstock Beach, South West England. Adapted from Pollard and Fletcher (2005).

Fracture systems are naturally present in most of the rock formations in the Earth's brittle crust, up to approximately 20 km depth (e.g., Dragoni and Pondrelli, 1991; Castaing et al., 1996; Tryggvason et al., 2002). Fractures in the crust have the tendency to cluster in damage zones around a major fault. The frequency of fracturing generally decreases with distance from the fault core (Faulkner et al., 2006) and depends on its size (Beach et al., 1999). The nature of the fault displacement and the existence of multiple fault cores affect the spatial distribution and the geometry of the fractured damage zone (Mitchell and Faulkner, 2009). Fractures also distribute on and around fold zones (Price, 1966), where they are controlled by a series of parameters, including the nature of the rock, the strain, the bedding thickness, and the ductile contrast between layers (**?**).

Some of these fractures outcrop at the surface and are visible on bare rock formations (e.g., Foord et al., 2015; Watkins et al., 2015; Procter and Sanderson, 2017), generally occurring in

aligned sets (Figure 1.3a). Deformation mechanisms, such as folding or shearing, can lead to complex fracture networks, with more than one set of fractures, showing different orientations, lengths and intensities (Figure 1.3b). Multiple fracture sets with different orientations can result from different deformation events over time.

Fractures occur naturally at a variety of scales (Figure 1.4) ranging from the grain (Hooker et al., 2009; Iñigo et al., 2012) to regional (Le Garzic et al., 2011; Le Goc et al., 2017) and continental scale (Wise, 1974; Perrin et al., 2016).

Since the second half of the 19^{th} century, fractures have been artificially induced in order to enhance the connectivity properties of rock (Testa, 2017). Hydraulic fracturing (also called fracking) is used to improve reservoir recovery, as fractures represent a preferential pathway for fluid flow. Applications include tight gas and shale gas reservoirs (Kendall et al., 2012), as well as geothermal systems (Baisch et al., 2009). As the technique is increasingly used, it is intensively monitored, as it frequently raises public concerns (Whitmarsh et al., 2015).

1.2 Importance of fractures

Because of their ubiquity in the top kilometres of the Earth's crust, fractures and cracks represent a major feature when studying its properties and have several important implications. They decrease the strength of rock (Alehossein and Boland, 2004), impact rheological behaviour (Zhang et al., 2017) and represent natural pathways for fluids in crustal rocks (Franciss, 2010). These impacts on mechanical and fluid-flow properties are of major importance for natural hazard assessment (e.g., Walter and Joswig, 2008; Hamlyn et al., 2014 and geo-industrial applications (e.g., Awdal et al., 2016; Jupe et al., 2003; Verdon et al., 2013). Fractures also provide secondary porosity, such as in carbonate reservoirs (e.g., Huang et al., 2017). Stress history and past deformation mechanisms can also be investigated by observing and analysing fracture networks (e.g., Castaing et al., 1996).

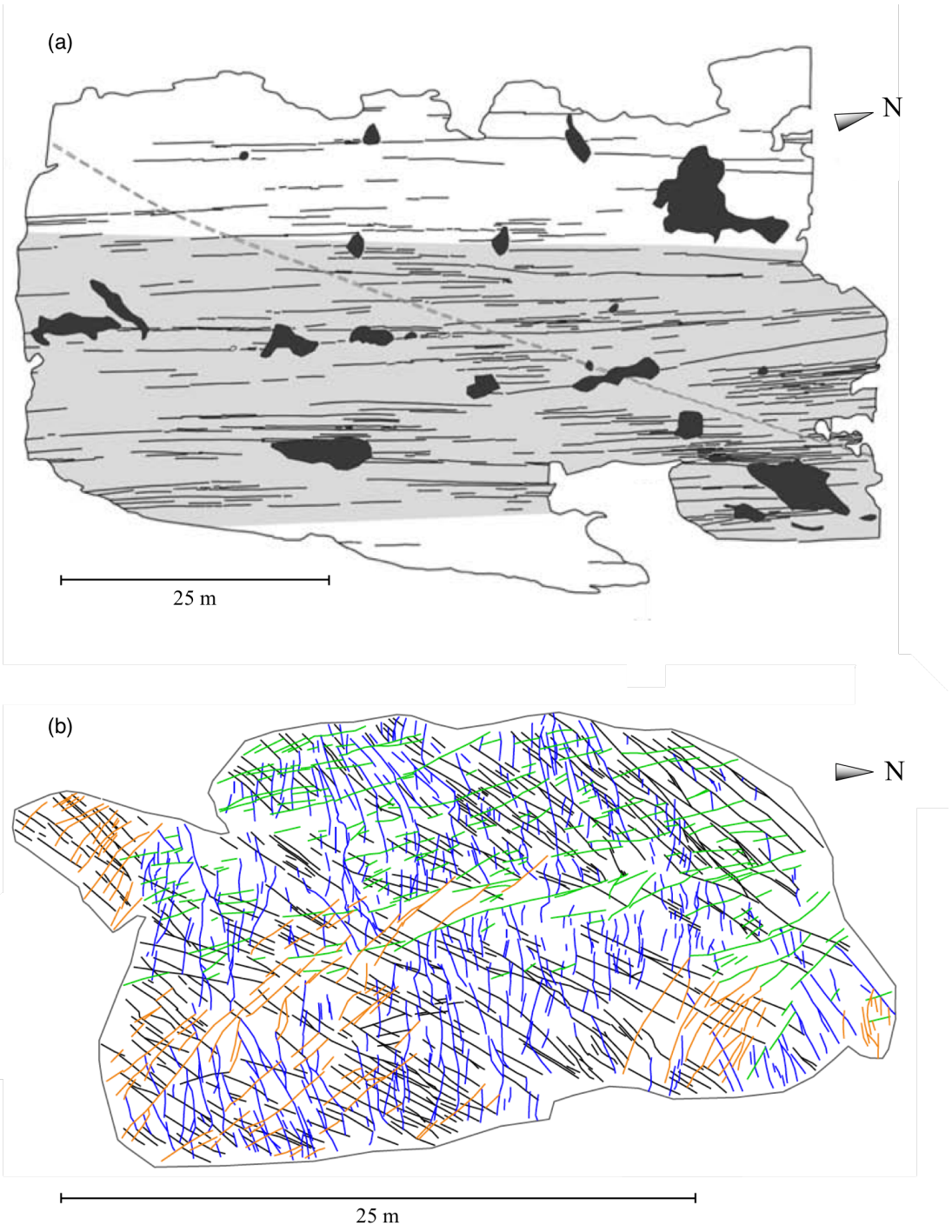

Figure 1.3 Fracture trace maps derived from outcrop mapping. (a) Ward Lake outcrop, California, United States. Light-grey region shows homogeneous subdomain, and black regions are unexposed and non mappable areas. Dashed line shows the location of a dike. Modified from Rohrbaugh et al. (2002). (b) Outcrop of the Torridon Group sandstone in the Achnashellach Culmination, Scotland. Each colour corresponds to a specific fracture set. Modified from Watkins et al. (2015)

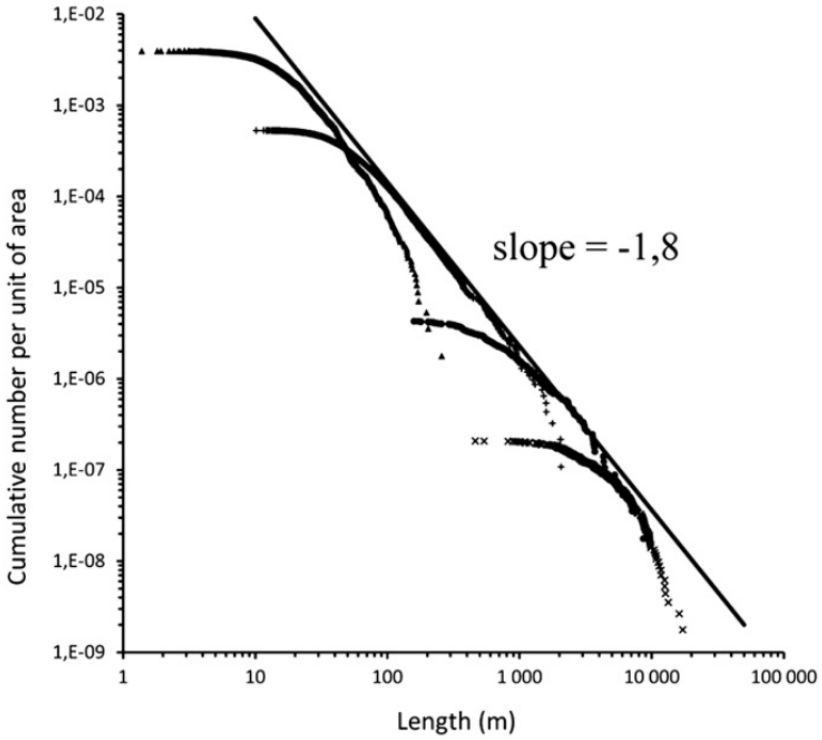

Figure 1.4 Normalised cumulative distributions of fracture lengths derived from structural maps. The four distinct datasets, marked as ▲ , +, • and × are based on mapping of fractures ranging over several order of magnitudes. Source: Le Garzic et al. (2011).

1.2.1 Permeability

One of the most important characteristics of the fractures is their ability to enhance the permeability of the medium they are embedded in. Laboratory experiments made on rock samples (Latief and Feranie, 2014; Lamur et al., 2017) and borehole measurements (Paillet and Kapucu, 1989) have shown the importance of fracture networks on the permeability of the medium. Faulkner and Armitage (2013) show permeability enhancement induced by the opening of micro-fractures at various loading paths in a granite sample. Anissofira and Latief (2015) estimate permeability in a geothermal reservoir, showing that fractures have a predominant role in transporting fluid compared to the granular type pores (Figure 1.5).

In reservoir settings, fluid storage is mainly due to pore spaces. Fractures act as secondary

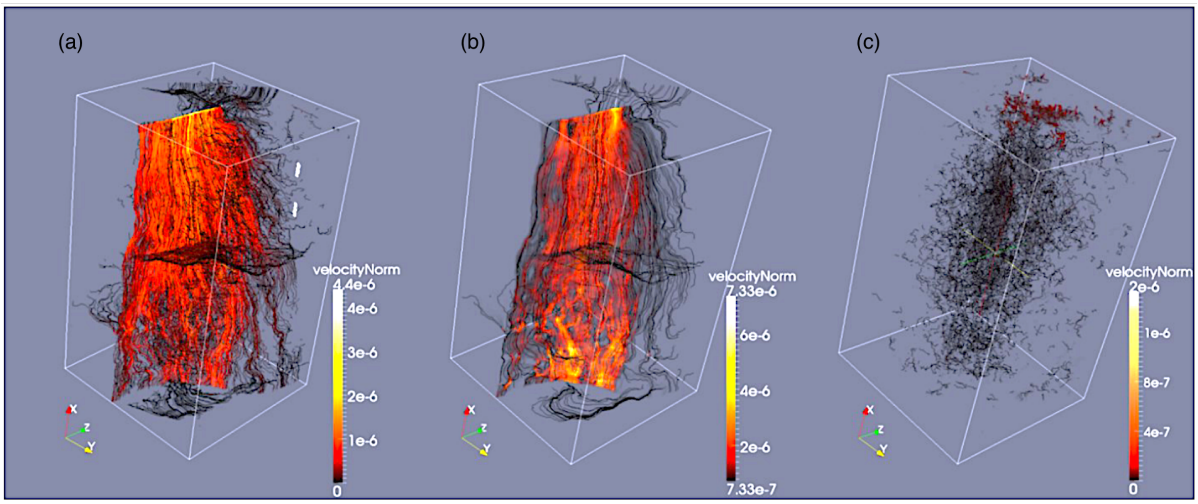

Figure 1.5 Modelled velocity profile produced by simulating fluid flow in a 3D scanned geothermal rock sample. (a) Contains fractures and granular pores. (b) Contains fractures only. (c) Contains granular pores only. Source: Anissofira and Latief (2015).

porosity features. Fractures generally represent a much more negligible volume and play a role of connection. They increase the permeability by linking together pore spaces (Gurevich et al., 2009), as they represent a natural pathway for fluids to flow in the rocks.

This is particularly important in production reservoirs, such as conventional (Al-Harrasi et al., 2011) and tight gas reservoirs (Wuestefeld et al., 2011a), as well as groundwater aquifers (Mansour et al., 2018; Nascimento Da Silva et al., 2004), and geothermal fields (Julian et al., 2010; Rial et al., 2005).

Reliable knowledge of fracture network geometry (strike, dip, density) in the reservoir is helpful before drilling production wells. To maximise the performance of the production reservoir, wells should intercept as much fracture as possible. This is the reason why modern recovery boreholes are drilled horizontally (or L-shaped), crosscutting vertically aligned fractures and improving the flow to the wells. Mapping fractures and assessing their preferred alignment is hence a necessary step in the reservoir exploration process.

The effect of fractures on permeability is also to be considered in storage reservoirs for sequestration of carbon dioxide (CO_2) or radioactive waste. Climate change challenges have

raised the question of mitigating anthropogenic CO_2 releases in the atmosphere. In recent years carbon capture and storage (CCS) technology has allowed CO_2 to be stored in sealed geological formations (Herzog, 2009; Singh, 2013). Managing nuclear waste also represents a challenging problem due to long decay times and high radioactivity. One of the solutions is disposal in impermeable formations (Hebel et al., 1978). In the case of CO_2 sequestration, as well as for radioactive waste storage, non-permeable sealing rocks are required to avoid leakage (Figure 1.6). Fracture detection is hence essential to assess the suitability of the potential storage structure and to monitor any change over time (White and Foxall, 2016; Harbert et al., 2016; Duxbury et al., 2012; Stork et al., 2015).

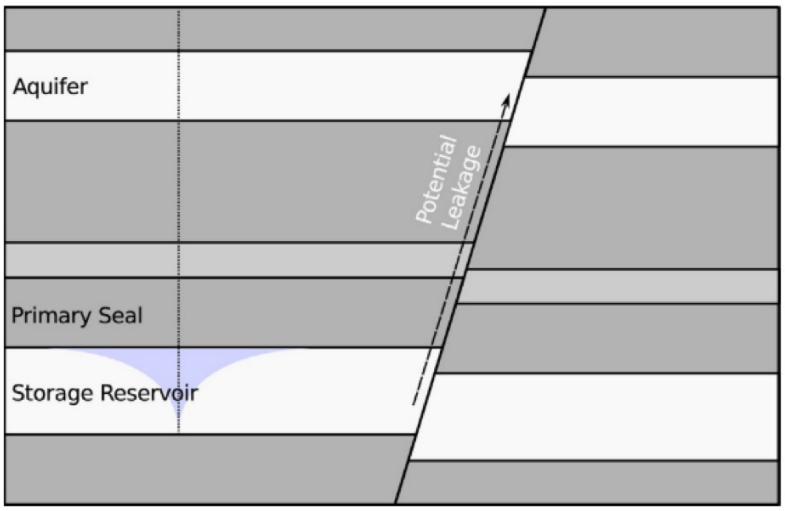

Figure 1.6 Cartoon of a storage reservoir isolated from an aquifer by a sealing formation. Leakage can potentially be triggered by faulting. Source: White and Foxall (2016).

Permeability and recovery rates can also be artificially enhanced by hydraulic fracture stimulation. This technique basically consists of pumping in a mixture of water, sand and chemicals, into the targeted reservoir to open new fractures and stimulate pre-existing ones. Hydraulic fracturing can be applied to tight shale reservoirs, when natural permeability is too low to provide enough fluid flow for production (Figure 1.7).

Hydraulic fracture stimulation is also used in the geothermal industry. The so-called

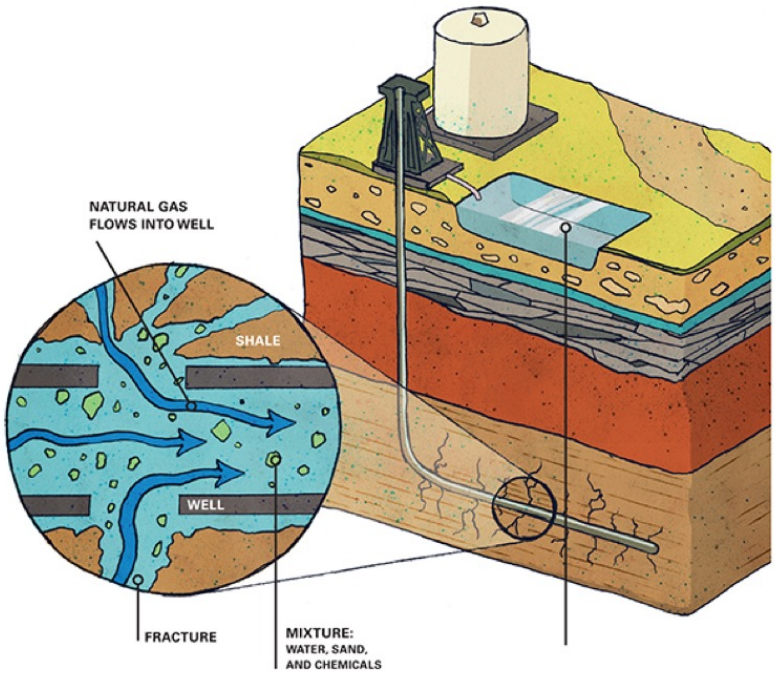

Figure 1.7 Cartoon of fracturing using horizontal injection well in a tight shale reservoir. Courtesy of Dow Water and Process Solutions.

Enhanced Geothermal System (EGS) involves human-made hydrothermal reservoirs. They are created where the rock is intrinsically hot but natural permeability or fluid saturation are too low to allow efficient fluid recovery (Adelinet et al., 2016). Applied to geothermal reservoirs, hydraulic fracturing does not only improve the permeability but also the contact area and heat transfer between the hot rock and the fluid (Gelet et al., 2013; Pruess and Doughty, 2010).

1.2.2 Elasticity and stability

As with permeability, the impact of fractures on elasticity is disproportionally large in comparison with the volume they occupy in the medium (Gurevich et al., 2009). This can affect the stability of the medium (Barton, 2007). For example, knowledge of fracture locations (Szalai et al., 2014) and how they trigger instability (Martel, 2004) is important while investigating landslide mechanisms. This provides insights into the stability of the slope and help to improve hazard prediction.

The observation of fractures, as well as the temporal variation of their characteristics, is not only of importance in landslide studies. Natural and engineering problems induced by stress build up and fracturing also include volcanic caldera collapse (Gudmundsson, 2006), borehole breakout (Zoback et al., 2003), crack propagation in concrete (Matsuyama et al., 2010; Ohno and Ohtsu, 2010) and decrease of rock stability during mining excavation (Lisjak et al., 2014; Wuestefeld et al., 2011a).

Since fractures affect the effective elasticity, they therefore have an impact on the propagation of seismic waves in the medium (Anderson et al., 1974; Hudson, 1980, 1981; Schoenberg and Douma, 1988; Guéguen and Schubnel, 2003). For example, fracture-induced anisotropy can be measured with seismic waves, such as variations in their velocity and amplitude as a function of propagation direction (Hall et al., 2002; Hobday and Worthington, 2012), or shear-wave splitting - SWS (Crampin, 1985). This link between seismic observations and elasticity can be used to identify and characterise fracture networks. However, models used to predict seismic wave propagation in fractured rock are often based on effective medium theory, as commonly used to model seismic anisotropy in fractured rock (e.g., Hall, 2000; Baird et al., 2013b; Adelinet et al., 2016). This theory mathematically approximates a heterogeneous medium with discrete fractures (Figure 1.8a) as a homogeneous medium with homogeneously distributed fractures (Figure 1.8b). Both the original heterogeneous medium and the effective media model have the same seismic response. Long wavelength seismic waves see both media equally. This implies that it is difficult to differentiate between long fractures and small cracks without more information.

1.3 Aims and motivations

The overall motivation of this thesis is to assess the use of seismic methods for characterising cracks and fractures in different settings. Factors such as fracture orientation, length scales, fluid content and strain rates are important influences on the seismic signals and often results in detectable and measurable seismic anisotropy. A principal focus is on recently developed methods to estimate fracture compliance ratios, which represents a powerful indicator of fluid fill

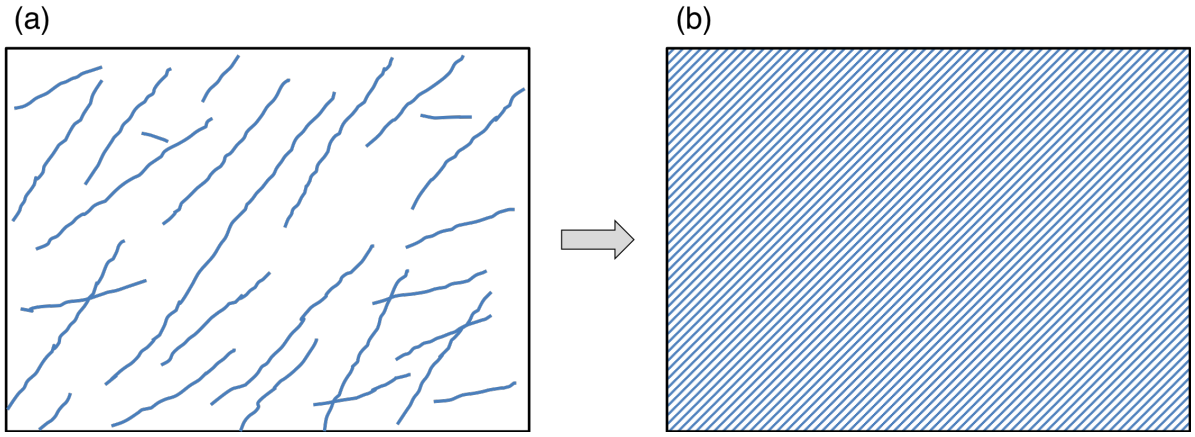

Figure 1.8 Homogenisation of a medium, using effective medium theory. Both (a) the fractured rock and (b) the equivalent medium have the same seismic response.

properties of fracture sets (See Chapter 2). Interest of this study is also on detecting temporal variations in seismic anisotropy and to explain these changes in terms of fracture properties, including fracture compliance.

Accordingly, this thesis is divided into two main sections. The first is the characterisation of a highly fractured outcrop at Lilstock, UK, through a mapping campaign (Chapter 3) and seismic experiments (Chapter 4). Second, a seismic dataset from an Eritrean volcano is analysed to image the fracture network in the shallow hydrothermal system (Chapter 5).

Chapter 3 presents a detailed mapping campaign of the wave-cut platform situated near the locality of Lilstock, South West England. Interest in this site is due to the fact that the fractures outcrop at the surface, and can be easily identified. Mapping of the platform using a drone (UAV) is used to quantify the fracture characteristics, such as the number of different sets present in the network, their preferred orientation, and their density.

In Chapter 4, a seismic experiment is conducted on the Lilstock wave-cut platform. The experiment first aims to recover fracture preferred orientation by measuring azimuthal variation in seismic velocities and seismic anisotropy. Furthermore, the use of rock physics-based inversions is used to estimate fracture compliances for the fracture sets visible in the outcrop. Observations

from the mapping campaign are used to calibrate the rock physics models and are used to create synthetic data. The best fitting model provides estimates on fracture compliance. Another interest of the Lilstock beach is that is affected by large tidal variations. Repeat seismic experiments are used to detect changes in fracture saturation as the tide retreats.

In Chapter 5, seismic data recorded at surface stations on Nabro volcano, Eritrea, are analysed, over a 4-month period following a major eruption on the 12 of June, 2011. Measurements of shear-wave splitting provide an indication of fracture-induced anisotropy in the hydrothermal reservoir. Interest resides in the fact that the seismicity is associated with the recent eruption, and anisotropy provides insights into the stress conditions and how they change over time. Another motivation in studying Nabro is the fact that it is considered to have significant geothermal potential. Fracture characterisation is thus important for future reservoir exploration and development. Finally, SWS is a potential tool for short-term forecasting of volcanic eruptions (e.g., Gerst and Savage, 2004). Temporal variation in SWS are investigated.

As part of the conclusions presented in Chapter 6, the results presented in this work are compared and contrasted with previous seismic experiments made under laboratory conditions and in the field, in order to better understand mechanisms linking seismic anisotropy and fracture compliance ratios. Suggestions for future experiment design are also presented.

CHAPTER 2

Seismic characterisation of fracture networks

Abstract

This chapter presents the theoretical background for fracture-induced anisotropy, providing a basis for the following chapters. First the basics of rock elasticity, including the effect of fractures on the medium, are briefly introduced. Second, the effects of fracture sets on the propagation of seismic waves are presented. The focus is on the variation of wave speeds as a function of azimuth, and shear-wave splitting. These methods are extensively employed in Chapter 4 and Chapter 5, respectively. Finally, the importance of fracture compliance is highlighted, including a complete review of existing measurements of fracture compliance ratios.

2.1 Rock elasticity

The elastic behaviour of a medium can be described by Hooke's law (Robert Hooke, 1635 - 1703), which relates the stress, σ_{ij}, applied to this medium and the resulting strain, ϵ_{kl}, by either the stiffness tensor $\mathbf{C}$, or the compliance tensor $\mathbf{S}$, such that,

$$\sigma_{ij} = C_{ijkl}\epsilon_{kl}, \tag{2.1}$$

and,

$$\epsilon_{kl} = S_{ijkl}\sigma_{ij}. \tag{2.2}$$

C and **S** are 3×3×3×3 tensors containing 81 components. Due to the symmetry of the stress and strain tensors, they can both be simplified into a 6 × 6 matrix (36 elastic components) using Voigt notation,

$$\begin{array}{ccccccccccc} ij & or & kl & & 11 & 22 & 33 & 23=32 & 13=31 & 12=21 & \\ & \downarrow & & & \downarrow & \downarrow & \downarrow & \downarrow & \downarrow & \downarrow & . \\ m & or & n & & 1 & 2 & 3 & 4 & 5 & 6 & \end{array} \tag{2.3}$$

Hence, Hooke's law (Equation 2.1) can be rewritten as,

$$\begin{pmatrix} \sigma_{11} \\ \sigma_{22} \\ \sigma_{33} \\ \sigma_{23} \\ \sigma_{13} \\ \sigma_{12} \end{pmatrix} = \begin{pmatrix} C_{11} & C_{12} & C_{13} & C_{14} & C_{15} & C_{16} \\ C_{12} & C_{22} & C_{23} & C_{24} & C_{25} & C_{26} \\ C_{13} & C_{23} & C_{33} & C_{34} & C_{35} & C_{36} \\ C_{14} & C_{24} & C_{34} & C_{44} & C_{45} & C_{46} \\ C_{15} & C_{25} & C_{35} & C_{45} & C_{55} & C_{56} \\ C_{16} & C_{26} & C_{36} & C_{46} & C_{56} & C_{66} \end{pmatrix} \begin{pmatrix} \epsilon_{11} \\ \epsilon_{22} \\ \epsilon_{33} \\ \epsilon_{23} \\ \epsilon_{13} \\ \epsilon_{12} \end{pmatrix}. \tag{2.4}$$

2.1.1 Isotropic medium

In the case of an isotropic medium, the simplest symmetry, the effective elasticity can be described by two independent constants, the Lamé parameters, λ and μ. The stiffness tensor can be simplified as,

$$\mathbf{C}_{iso} = \begin{pmatrix} (\lambda+2\mu) & \lambda & \lambda & 0 & 0 & 0 \\ \lambda & (\lambda+2\mu) & \lambda & 0 & 0 & 0 \\ \lambda & \lambda & (\lambda+2\mu) & 0 & 0 & 0 \\ 0 & 0 & 0 & \mu & 0 & 0 \\ 0 & 0 & 0 & 0 & \mu & 0 \\ 0 & 0 & 0 & 0 & 0 & \mu \end{pmatrix}. \tag{2.5}$$

The Lamé parameters are used to determine the seismic velocities of the compressional and shear waves, v_p and v_s, respectively,

$$v_p = \left(\frac{\lambda+2\mu}{\rho}\right)^{\frac{1}{2}}, \tag{2.6}$$

and

$$v_s = \left(\frac{\mu}{\rho}\right)^{\frac{1}{2}}, \tag{2.7}$$

where ρ is the density of the isotropic medium.

In an isotropic medium, the wave speeds at a point are the same in any direction.

2.1.2 Transverse isotropy

The simplest form of anisotropy is that of a transversely isotropic (TI) medium, which has a plane of isotropy and an axis of symmetry normal to it (Figure 2.1a,b). Depending of the orientation of the medium, it can be described as horizontal transversally isotropic (HTI), vertical transversally isotropic (VTI), or tilted transversally isotropic (TTI). TI medium shows a rotational invariance in elastic properties around an axis of symmetry. In other words, properties vary only as a function of angle to the symmetry axis.

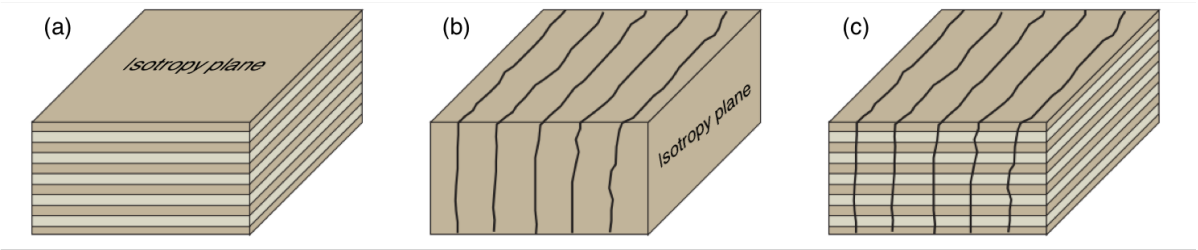

Figure 2.1 VTI, HTI and orthorhombic anisotropy due to (a) horizontal layering, (b) aligned vertical fractures and (c) a combination of fractures and layering, respectively (from Baird et al., 2013b).

2.1.2.1 HTI anisotropy

Fractures are generally sub-vertical in reservoir settings and normally occur in aligned sets. The effective elastic response of such configuration can therefore be described as a HTI medium (Figure 2.2).

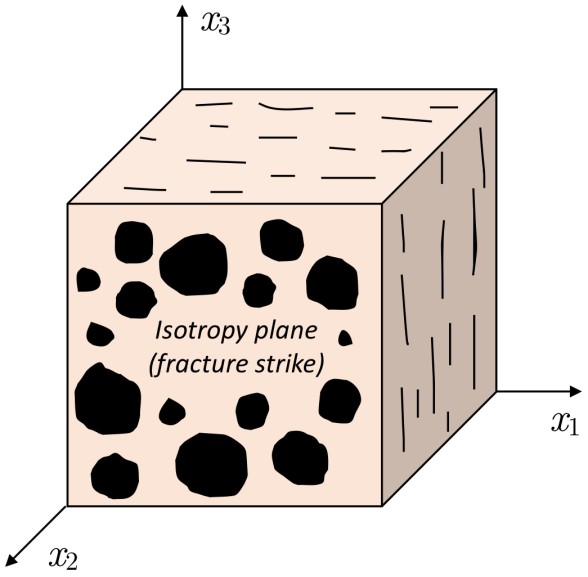

Figure 2.2 Medium with HTI anisotropy caused by aligned cracks (black discs) embedded in a isotropic background. Symmetry axis is aligned with x_2.

With a set of vertical fractures aligned in the x_1- x_3 plane, where the symmetry axis is aligned parallel to the x_2 axis, the stiffness tensor in Voigt notation can be written as,

$$\mathbf{C}_{HTI} = \begin{pmatrix} C_{11} & C_{12} & C_{12} & 0 & 0 & 0 \\ C_{12} & C_{22} & C_{23} & 0 & 0 & 0 \\ C_{12} & C_{23} & C_{11} & 0 & 0 & 0 \\ 0 & 0 & 0 & C_{44} & 0 & 0 \\ 0 & 0 & 0 & 0 & C_{44} & 0 \\ 0 & 0 & 0 & 0 & 0 & C_{66} \end{pmatrix}, \tag{2.8}$$

with,

$$C_{23} = C_{33} - 2C_{44}. \tag{2.9}$$

2.1.2.2 VTI anisotropy

VTI anisotropy results from layering or the preferred alignment of phyllosilicate minerals in shales (Kendall et al., 2007). Five elastic constants are required to describe this anisotropy and the symmetry axis is in the vertical direction, x_3, as,

$$\mathbf{C}_{VTI} = \begin{pmatrix} C_{11} & C_{11}-2C_{66} & C_{13} & 0 & 0 & 0 \\ C_{11}-2C_{66} & C_{11} & C_{13} & 0 & 0 & 0 \\ C_{13} & C_{13} & C_{33} & 0 & 0 & 0 \\ 0 & 0 & 0 & C_{44} & 0 & 0 \\ 0 & 0 & 0 & 0 & C_{44} & 0 \\ 0 & 0 & 0 & 0 & 0 & C_{66} \end{pmatrix}. \tag{2.10}$$

Thomsen (1986) expresses the five VTI parameters in terms that can be more readily expressed as a function of wave speeds.

Since an isotropic medium can be described by the two Lamé parameters (Equation 2.5), a VTI medium has three anisotropy parameters which can be defined by the Thomsen (1986) parameters and defined as,

$$\varepsilon = \frac{C_{11} - C_{33}}{2C_{33}} = \frac{v_{p_H}^2 - v_{p_V}^2}{2v_{p_V}^2}, \tag{2.11}$$

$$\gamma = \frac{C_{66} - C_{55}}{2C_{55}} = \frac{v_{s_H}^2 - v_{s_V}^2}{v_{s_V}^2} \tag{2.12}$$

and

$$\delta = \frac{(C_{13} - C_{55})^2 - (C_{33} - C_{55})^2}{2C_{33}(C_{33} - C_{55})}. \tag{2.13}$$

ϵ is "*the fractional difference between vertical and horizontal P-wave velocities* (Thomsen, 1986). γ relates horizontal and vertical shear-wave velocities. δ is a more difficult parameter to relate to seismic velocities, as it describes velocities in of axis directions of propagation, and is sometimes referred as the short-offset effect.

2.1.2.3 TI compliance tensor

By inversion of the stiffness tensor (Equation 2.8), the compliance tensor in HTI media with a symmetry axis aligned in the x_1 direction can be rewritten as,

$$\mathbf{S}_{HTI} = \begin{pmatrix} S_{11} & S_{12} & S_{12} & 0 & 0 & 0 \\ S_{12} & S_{33} & S_{23} & 0 & 0 & 0 \\ S_{12} & S_{23} & S_{33} & 0 & 0 & 0 \\ 0 & 0 & 0 & S_{44} & 0 & 0 \\ 0 & 0 & 0 & 0 & S_{44} & 0 \\ 0 & 0 & 0 & 0 & 0 & S_{66} \end{pmatrix}, \tag{2.14}$$

The elastic compliance tensor for an HTI medium may be expressed in terms of the Young's modulus, E_i, corresponding to axis x_i, the Poisson's ratio, ν_{ij}, that relates the strain along x_j to stress applied along x_i and the shear modulus, μ_{ij}, corresponding to the plane x_{ij} as,

$$\mathbf{S}_{HTI} = \begin{pmatrix} 1/E_1 & -\nu_{21}/E_1 & -\nu_{31}/E_1 & 0 & 0 & 0 \\ -\nu_{12}/E_1 & 1/E_1 & -\nu_{31}/E_1 & 0 & 0 & 0 \\ -\nu_{13}/E_1 & -\nu_{12}/E_1 & 1/E_3 & 0 & 0 & 0 \\ 0 & 0 & 0 & 1/\mu_{13} & 0 & 0 \\ 0 & 0 & 0 & 0 & 1/\mu_{13} & 0 \\ 0 & 0 & 0 & 0 & 0 & 1/\mu_{12} \end{pmatrix}, \tag{2.15}$$

The HTI tensor can be rotated to describe dipping fractures or vertical transverse isotropy (VTI) caused by horizontal alignments. The presence of more than one set of fractures, with different orientations, as well as other anisotropic features, such as sedimentary layering or aligned crystals, adds complexity to the anisotropy by producing lower degree of symmetry and increasing the number of required anisotropy parameters. In the case of one set of vertical fractures embedded in a medium with horizontal layering (Figure 2.1c), the symmetry is orthorhombic and 9 anisotropy parameters are necessary to describe the elasticity of the medium.

2.1.3 Additional compliance approach

Various mathematical formulations have been developed to describe fracture networks, such as these that assume ellipsoidal inclusions (Budiansky and O'Connell, 1976; Hoenig, 1978; Tandon and Weng, 1984), penny-shaped cracks (Hudson, 1980, 1981; Cheng, 1993; Thomsen, 1995), low aspect ratio parallel fractures (Frazer, 1990; Sayers and Kachanov, 1995; Schoenberg and Sayers, 1995), plane distributions of cracks and welds (Hudson and Liu, 1999), among others (Figure 2.3).

In this work, the additional compliance approach (Schoenberg and Sayers, 1995) is used. This theory considers fractures as poorly bonded interfaces representing displacement discontinuities. This approach is adapted as it is the most flexible description of a fracture. Few assumptions are made about the physical properties of the fractures. This is particularly important when

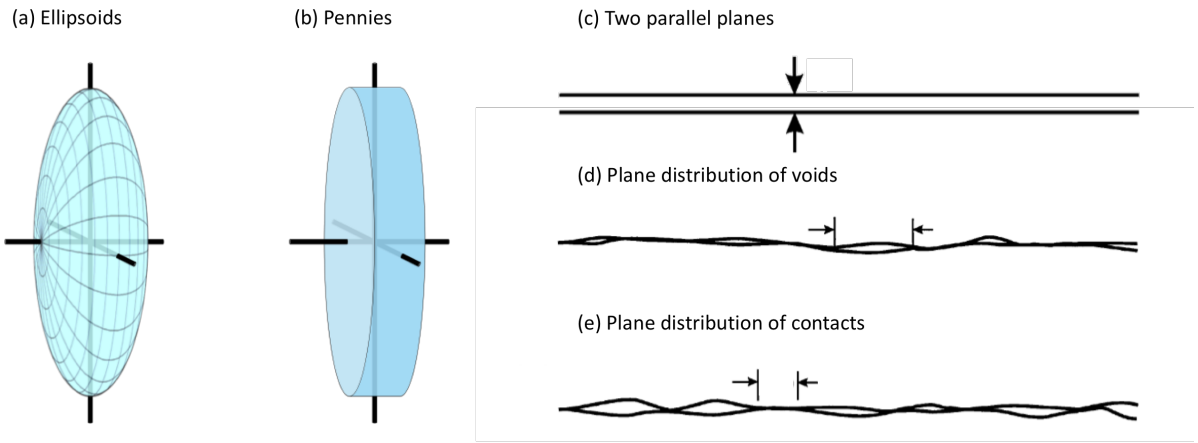

Figure 2.3 Different approaches to represent fractures. Inclusions are generally represented by (a) ellipsoid or (b) penny-shaped inclusions. Fractures can be thought of (c) two parallel surfaces, (d) a planar distribution of voids or (e) welds.

studying reservoir fractures, where no o little information is available about their internal architecture and filling conditions.

A stress applied to a medium containing a single fracture will result in a difference in the displacements of the two surfaces of the fracture and produce a displacement discontinuity $[u_i]$, which can be described as,

$$\int_A [u_i] dA \equiv \bar{\sigma}_{ij} n_{ij}, \tag{2.16}$$

where A is a fracture area, with normal n_j, and $\bar{\sigma}_{ij}$ is the average stress.

By summing all the displacement discontinuities in a medium of volume V, an additional strain is produced, such that Equation 2.2 can be rewritten as,

$$\epsilon_{ij} = S_{ijkl_b} \bar{\sigma}_{kl} + \frac{1}{2V} \sum_r \int_{A_r} ([u_i] n_j + [u_j] n_i) dA. \tag{2.17}$$

S_{ijkl_b} is the compliance of the non-fractured background medium, while the second part of the equation is the additional strain introduced by the presence of r fractures (represented as displacement discontinuities). This strain added by the fractures is related to the applied stress though a 3×3 fracture compliance tensor, Z_{ij},

$$\frac{1}{V}\sum_{r}\int A_r[u_i]dS = Z_{ij}\bar{\sigma}_{jk}n_k. \tag{2.18}$$

The extra compliance as a result of m sets of fractures is $S^{(m)}_{ijkl_f}$ (Schoenberg and Sayers, 1995), so combining 2.17 and 2.18 yields,

$$S^{(m)}_{ijkl_f} = \frac{1}{4}\sum_{m}(Z^{(m)}_{ik}n^{(m)}_l n^{(m)}_j + Z^{(m)}_{jk}n^{(m)}_l n^{(m)}_i + Z^{(m)}_{il}n^{(m)}_k n^{(m)}_j + Z^{(m)}_{jl}n^{(m)}_k n^{(m)}_i). \tag{2.19}$$

In the presence of m sets of fractures, each with its own orientation (e.g., normal n_j) and its own Z_{ij},

$$S_{ijkl} = S_{ijkl_b} + \sum_{m} S^{(m)}_{ijkl_f}. \tag{2.20}$$

If the fractures are considered to be rotationally invariant and with no preferred slip direction, Z_{ij} is simplified and reduced to a three non-zero elements tensor, defined by only two parameters, Z_N and Z_T, the normal and tangential fracture compliances (Figure 2.4),

$$Z_{ij} = Z_N n_i n_j + Z_T(\delta_{ij} - n_i n_j), \tag{2.21}$$

where δ_{ij}, is the Kronecker delta.

In the case of a single set of fractures oriented in the $x_2 - x_3$ plane, their compliance tensor in Voigt notation is therefore,

$$\mathbf{S}_{mn_f} = \begin{pmatrix} Z_N & 0 & 0 & 0 & 0 & 0 \\ 0 & 0 & 0 & 0 & 0 & 0 \\ 0 & 0 & 0 & 0 & 0 & 0 \\ 0 & 0 & 0 & 0 & 0 & 0 \\ 0 & 0 & 0 & 0 & Z_T & 0 \\ 0 & 0 & 0 & 0 & 0 & Z_T \end{pmatrix}. \tag{2.22}$$

Z_N and Z_T represent the least amount of information needed to characterise the fracture set. These two components represent all that can be obtained from seismic data without further information about the nature of the fractures (e.g., shape and wall spacing). The ratio of the normal to the tangential component, the fracture compliance ratio Z_N/Z_T provides insights into the physical properties of the fractures .

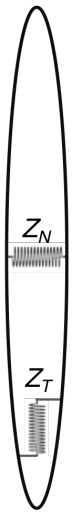

Figure 2.4 Normal and tangential components of fracture compliance.

To estimate Z_N/Z_T from seismic velocities, synthetic data are created using a series of rock physics models. These models consist in a rock matrix containing one or more sets of fractures. The best fitting model is the one which minimise the difference between the observed and the modelled seismic velocities.

2.2 Seismic anisotropy to image fractures

As discussed in Section 2.3, the compliance induced by aligned fractures controls the behaviour of seismic wave speeds. Fracture compliance, in turn, is controlled by fracture and infill properties. Observations of seismic anisotropy can be therefore used to characterise fractures.

Anisotropy refers to a medium in which the physical properties vary as a function of direction. In the frame of this thesis, focus is on the analysis of seismic anisotropy (i.e., variations of the seismic wave speed as a function of the direction of propagation).

Seismic anisotropy is here investigated in the upper part of the Earth's crust, where it is generally controlled by the presence of cracks and fractures (Crampin, 1994), which can be filled with material, generally fluids. In sedimentary basins, anisotropy is also controlled by horizontal layers (Sayers, 1999). In the lowermost part of the crust, fractures are closed due to the high confining pressures (Boness and Zoback, 2004) and anisotropy is mainly caused by layering (Backus, 1962) or crystal alignment (Lloyd and Kendall, 2008).

There are a number of approaches for using seismic methods to investigate anisotropy associated with fractures. They can be divided in two groups, depending whether the velocity (e.g., Savage, 1999) or the amplitude (e.g., Hall et al., 2002) of the seismic waves is investigated (see Delbecq et al., 2013 for a review).

In this thesis, anisotropy is described and measured using velocity-based approaches. First, in Chapter 4, the variation of seismic velocities with azimuth is investigated on fractured outcrop. Second, in Chapter 5, SWS is measured in the hydrothermal system of an active volcano in Eritrea.

2.2.1 Azimuthal variation of seismic waves

The presence of an aligned fracture set in rock leads to a variation of velocity with direction. Compressional (P) waves propagate faster in the direction parallel to the fracture preferred orientation, and slower in the direction perpendicular to the fractures (Figure 2.5).

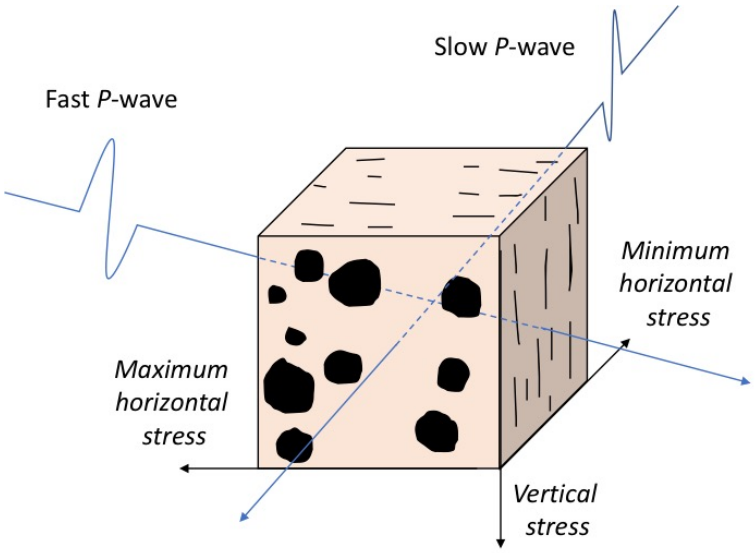

Figure 2.5 *P*-wave velocity as a function of the direction of propagation in an isotropic medium containing a set of aligned fractures (black discs). Maximum *P*-wave velocity is parallel to the plane of the fractures.

Such behaviour has been observed in seismic experiments on synthetic fractured media (Rathore and Fjaer, 1994), and in the field (Hess, 1964; Bamford and Nunn, 1979; Nunn et al., 1983; Hobday and Worthington, 2012; Foord et al., 2015; Inks et al., 2015). Figure 2.6 shows some results from laboratory and *in-situ* measurements performed to seismically identify the orientation of fracture sets. Although scattering is significant, a clear maximum in *P*-wave velocities appears in the direction parallel to the observed cracks and fractures. In some cases, results from the field were calibrated by comparing seismic data with outcrop or core data. Such experiments were also conducted to assess effective medium models or to evaluate fracture properties such as density and saturation (Crampin et al., 1980).

2.2.2 Shear-wave splitting (SWS)

Another observable effect of anisotropy on seismic wave propagation is the splitting of an *S*-wave into two orthogonally polarised *S*-waves, one being faster than the other. The fast shear-wave polarisation (ϕ) and the time delay between the fast and the slow *S*-waves (δt) are referred as the splitting parameters and characterise the style of anisotropy of the medium traversed by the

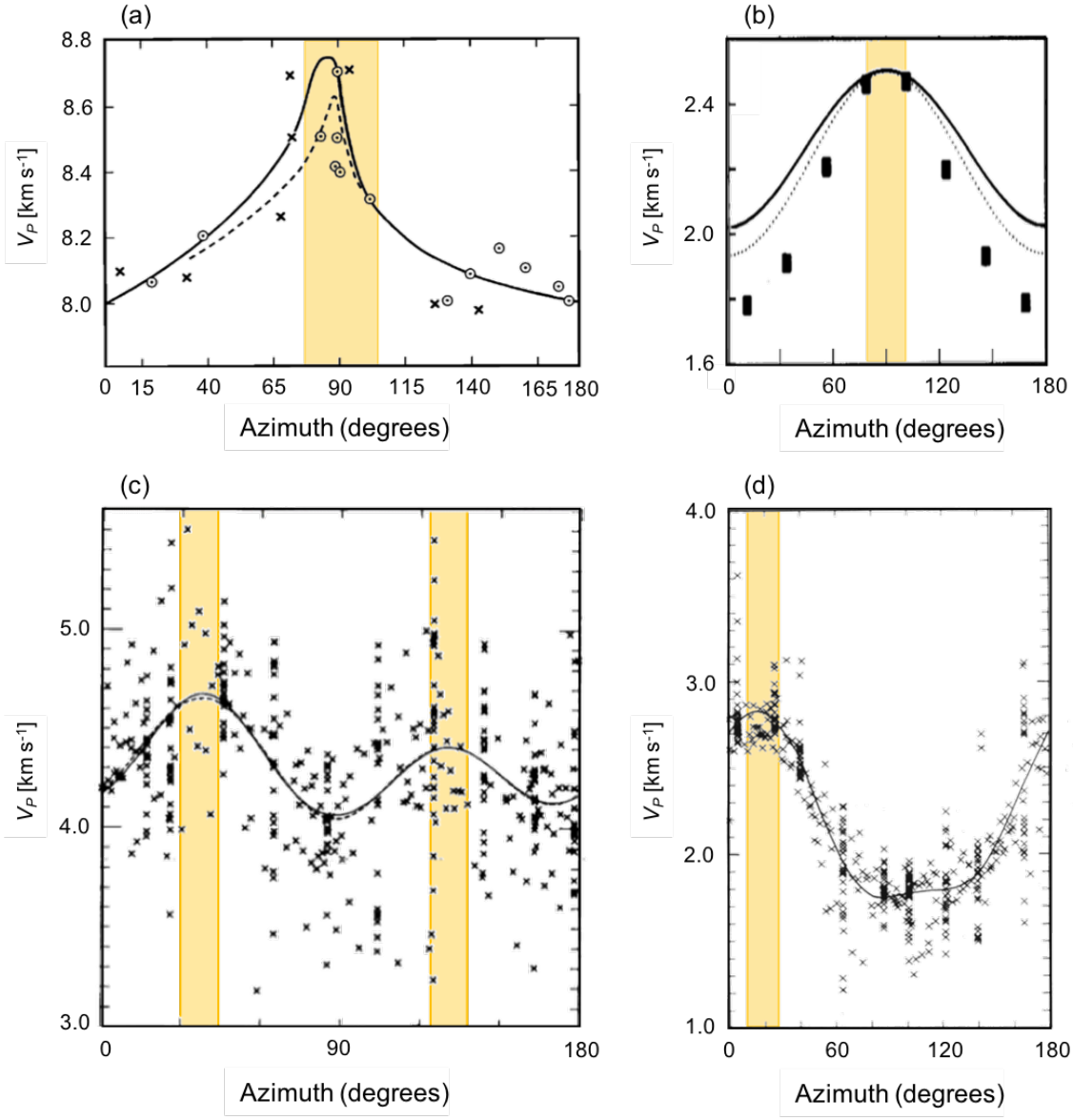

Figure 2.6 Examples of measurements of *P*-wave velocity as a function of the azimuth. Orientation of aligned sets of vertical fractures are delimited by orange shades. Symbols show individual velocity measurements. Solid and/or dashed lines show approximations of the velocity pattern using effective medium models (see the references for more details about specific methods). (a) Seismic refraction survey near the Mendocino and Maui fracture areas, California (Hess, 1964). Plot modified from Savage (1999). (b) Acoustic survey made on synthetic sandstone containing dry cracks (Rathore and Fjaer, 1994). Solid line shows model predictions from Thomsen (1995). Dashed lines show models predictions from Hudson (1980, 1981). (c) Seismic refraction on fractured limestone (Bamford and Nunn, 1979). Plot modified from Crampin et al. (1980). (d) Seismic velocities and best fitting line from a seismic survey performed on fractured chalk (Nunn et al., 1983).

seismic waves. The fast *S*-wave tends to polarise in the orientation of the symmetry plane of anisotropy, while the slow *S*-wave polarises orthogonally to the fast *S*-wave. In the case of the presence of a single set of aligned fractures, ϕ lies in the fracture plane (Figure 2.7). Although more complexity is added in the case of multiple fracture sets, observations of ϕ have been used to detect several fracture directions (e.g., Lou and Rial, 1997; Nowacki et al., 2018). On the other hand, δt provides information about the strength of anisotropy in the medium, and can be related to fracture density and the thickness of the anisotropic layer (Lou and Rial, 1997). Upon leaving the anisotropic region, the splitting parameters are frozen and preserved. This anisotropic signature can therefore be recorded by receivers, such as surface seismic stations or borehole seismic arrays.

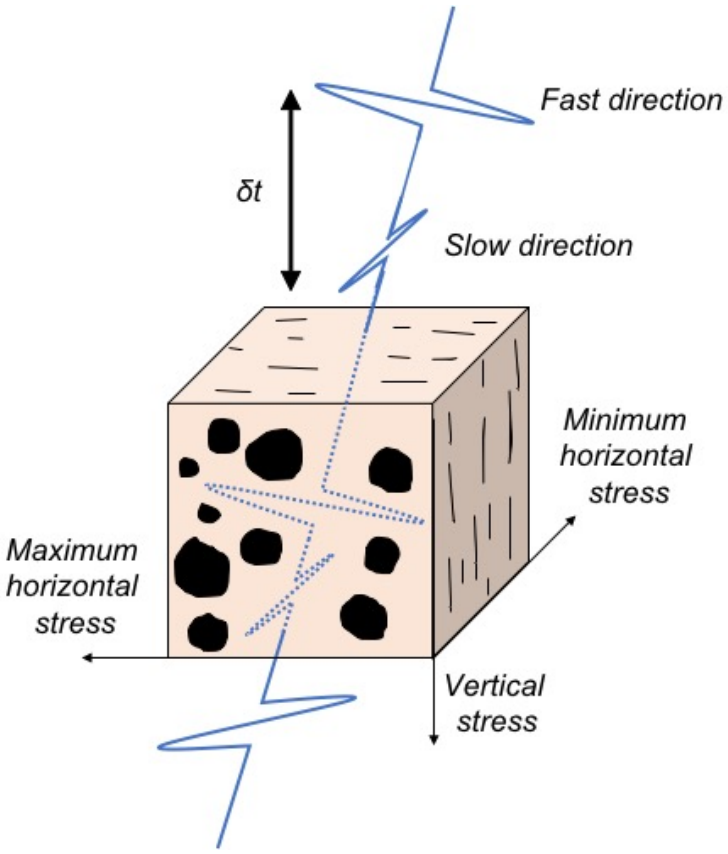

Figure 2.7 Shear-wave travelling though an anisotropic medium and splitting into two orthogonally polarised fast and slow shear-waves. Anisotropy is caused by a set of vertically aligned fractures (black discs).

In this thesis, the methodology of Silver and Chan (1991) is used to assess SWS. First, the data are converted from the geographic reference frame (E-W, N-S, Z) to the raypath reference frame. Then, for each event-receiver signal, the *S*-wave arrival is picked and a window containing the *S*-phase wavelet is defined for analysis purposes. Finally, a grid search is performed over the splitting parameters, where the *S*-waveforms are rotated by ϕ and shifted by δt to determine values that best linearise the *S*-wave particle motion. With SWS, the energy of the incident *S*-phase is split onto the orthogonally polarised fast and slow *S*-waves, and the particle motion becomes elliptical. The splitting values that best linearise the particle motion have the minimum eigenvalue of the covariance matrix, which describes the ellipticity of the particle motion after correction. The best parameters also minimise the energy on the corrected component transverse to the original *S*-wave polarisation.

This method for estimating SWS parameters can be dependent on the picking of the *S*-wave wavelet, as slight variations in its location may result in significantly different outputs. This has been highlighted by Teanby et al. (2004a), who proposed a method of multiple windows and cluster analysis to tackle this issue. This ensures a reliable SWS measurement, with a result not being dependent on picking the wavelet. The method of Silver and Chan (1991) and its extension by Teanby et al. (2004a) is applicable to sub-vertical incident waves recorded at surface seismic stations (e.g., Schlaphorst et al., 2017).

SWS is considered to be one of the most robust tools to characterise anisotropy (Baird et al., 2013a; Verdon and Wüstefeld, 2013; Kendall et al., 2012). The technique has been used to investigate anisotropy in multiple environments, including the mantle (Silver and Chan, 1991; Thomas and Kendall, 2002; Long and Silver, 2009; Savage, 1999), subduction zones (Schlaphorst et al., 2017; Walpole et al., 2017), geological reservoirs (Rial et al., 2005; Verdon and Kendall, 2011), fault zones (Liu et al., 2008), volcanic settings (Bianco et al., 2006; Keats et al., 2011; Baird et al., 2015; Nowacki et al., 2018; Johnson and Poland, 2013), and laboratory samples (Rathore and Fjaer, 1994). More recently, techniques have been developed to directly estimate fracture compliance from SWS measurements (Verdon and Wüstefeld, 2013).

In this thesis, SWS is measured on signals recorded at surface stations above the hydrothermal system of Nabro volcano, Eritrea, which is considered to have significant geothermal potential (see Chapter 5). Fast shear-wave polarisation and time delay have to potential to give insights into local anisotropy and fracture characteristics in geothermal fields (e.g., Lou and Rial, 1997; Tang et al., 2015; Vlahovic et al., 2002; Elkibbi and Rial, 2005; Rial et al., 2005).

2.3 Fracture compliance

Estimates of Z_N/Z_T on laboratory samples or in the field were initially aimed to calibrate discrete fracture network or effective medium models (e.g., Sayers and den Boer, 2012; Pyrak-Nolte et al., 1990; Verdon et al., 2008). Prior to that, most models assumed scalar fractures (i.e., $Z_N/Z_T = 1$).

Hudson (1981) shows that $Z_N/Z_T \approx 1$ for a unfilled penny-shaped fracture, while adding a stiff fluid decreases Z_N and does not affect Z_T, reducing Z_N/Z_T. Pointer et al. (2000) mathematically demonstrate than Z_N/Z_T is affected by the stiffness of the fluid and its capacity flow between fractures and pore spaces, and the stiffness of the fluid (Foord et al., 2015). In the case of a soft fluid or if the fluid can flow easily, $Z_N/Z_T \approx 1$. Otherwise, Z_N is smaller than Z_T and $Z_N/Z_T \rightarrow 0$. Z_N/Z_T is also affected by the internal architecture of the fractures. Sayers et al. (2009) numerically show that mineralised asperities in fractures influence Z_N/Z_T.

More recently, studies have focused on directly determining Z_N/Z_T, as it is considered a good proxy for permeability conditions in fractured medium. Most values were obtained through laboratory experiments, at a reduced scale, while measurements made at the field scale are still sparse. Laboratory experiments allow control over the parameters of the fractured samples. As they are obtained in a controlled environment, they are important in understanding controls on fracture compliance.

The published values of Z_N/Z_T in the literature can be classified into three main categories: (1) core samples, (2) synthetic samples, and (3) field measurements. An inventory of these

results is listed in Table 2.1. Focus is on measuring specific fracture compliances and fracture compliance ratios. Some of the laboratory experiments also performed measurements on samples in dry and saturated conditions, or containing inclusions, in order to further assess the effect of fracture properties on Z_N/Z_T.

2.3.1 Core samples

Several studies have measured elastic wave velocities on core samples that do not contain macro fractures, but rather attempt to image the effects of grain-scale discontinuities. Verdon et al. (2008) inverted P- and S-wave ultrasonic measurements made by Hall et al. (2008) on dry core samples from the Clair oilfield (UK Continental Shelf), finding $0.68 < Z_N/Z_T < 1.06$. Angus et al. (2009) inverted published data for fracture parameters on more than 150 measurements from the literature made on dry core samples of sedimentary rocks. They found $0.25 < Z_N/Z_T < 1.5$. Sayers and Han (2002) inverted similar ultrasonic measurements made by (Han et al., 1986) on sandstone samples in dry and water-saturated conditions, finding $0.25 < Z_N/Z_T < 3$ and $0.05 < Z_N/Z_T < 1.1$, respectively. Finally, Macbeth and Schuett (2007) analysed the impact of thermally damaging samples. They inverted ultrasonic measurements and find $0 < Z_N/Z_T < 0.6$ for intact core samples, and $0 < Z_N/Z_T < 1.2$ for thermally damaged samples. Higher Z_N/Z_T is attributed to the higher degree of micro fracturing and the thermal smoothening of the grain-grain contact areas.

Other studies used similar techniques to characterise samples containing discrete fractures, these being considered more representative to field scale fractures. Using ultrasonic data, Pyrak-Nolte et al. (1990) estimated the compliance of a single fracture embedded in a core sample of quartz monzonite. Based on their estimates, fracture compliance ratios can be determined as, $0.20 < Z_N/Z_T < 0.77$ for dry samples, and $0.04 < Z_N/Z_T < 0.48$ for water-saturated samples. Using a similar technique, Lubbe et al. (2008) artificially created a fracture by cutting and reassembling core samples of limestone (Figure 2.8). They found $0.20 < Z_N/Z_T < 0.55$ for dry samples and $0.02 < Z_N/Z_T < 0.05$ for honey-saturated samples. Sayers (1999) inverted ultrasonic measurements made by Hornby (1994) on water-saturated shale samples finding that

$0.26 < Z_N/Z_T < 0.41$.

	Reference	Method	Medium conditions	Z_N/Z_T
	Core sample			
1	Pyrak-Nolte at al. (1990)	Ultrasonic measurements on quartz sample containing a single fracture.	Dry sample.	0.2 - 0.7
			Water saturated.	0.04 - 0.05
2	Sayers (1999)	Ultrasonic measurements on shale samples.	Dry samples.	0.47 - 0.80
		Data from Johnston and Christensen (1993) and Vernik (1993).	Water saturated.	0.26 - 0.41
3	Sayers and Han (2002)	Ultrasonic measurements on grain-scale fabrics.	Dry samples.	0.25 - 3
		Data from Han et al. (1986).	Water saturated.	0.05 - 1.1
4	MacBeth and Schuett (2007)	Ultrasonic measurements on grain-scale fabrics.	Undamaged sample.	0 - 0.6
			Thermally damaged.	0 - 1.2
5	Lubbe et al. (2008)	Ultrasonic measurements on limestone samples containing a single fracture.	Dry samples.	0.2 - 0.55
			Honey saturated.	0.02 - 0.05
6	Verdon et al. (2008)	Ultrasonic measurements on grain-scale fabrics.	Dry samples.	0.68 - 1.06
		Data from Hall et al. (2007).		
7	Angus et al. (2009)	Ultrasonic measurements on grain-scale fabrics.	Dry samples.	0.25 - 1.50
		Data from literature sources.		
	Synthetic sample			
8	Hsu and Schoenberg (1993)	Ultrasonic measurements on medium of crompressed perspex plates.	Dry samples.	0.8 - 1.0
			Honey saturated.	0.1
9	Verdon and Wüstefeld (2013)	Synthetic sample containing a population of cracks.	Dry.	0.46
		Ultrasonic data from Rathore et al. (2014), reanalysed by Hudson et al. (2001).		
10	Choi et al. (2014)	Ultrasonic measurements on gypsum specimens containing synthetic fractures.	Mated.	0.38 - 1.48
			Nonmated.	0.1 - 1.17
11	Far et al. (2014)	Ultrasonic measurements on a stack of Plexiglass plates.	With rubber inclusions.	0.01 - 0.25
			Without rubber inclusions.	0.11 - 0.91
	Field data			
12	Hobday and Worthington (2012)	Hammer seismic imaging of fractured outcrop.	Water saturated.	< 0.1
13	Baird et al. (2013)	SWS during hydraulic fracture stimulation.	Undrained. Pre-fracturing.	0.30
			Drained. Post-fracturing.	0.60
14	Verdon and Wuestefeld (2013)	SWS during hydraulic fracture stimulation.	Full dataset.	0.70 - 0.78
			After proppant injection.	1.0 - 2.0
15	Foord et al. (2015)	Hammer seismic imaging of (i) a limestone outcrop and (ii) carboniferous limestones underlying a parkland.	(i) Water saturated fractures.	0.37 ± 0.06
			(ii) Patially drained fractures.	0.75 ± 0.10
16	Yu (2016)	Estimation of shale anisotropy using downhole microseismic dataset.	Dry or gas saturated fractures.	2.5

Table 2.1 Z_N/Z_T inventory based on published measurements made on laboratory samples and in the field. Updated from Verdon and Wüstefeld (2013).

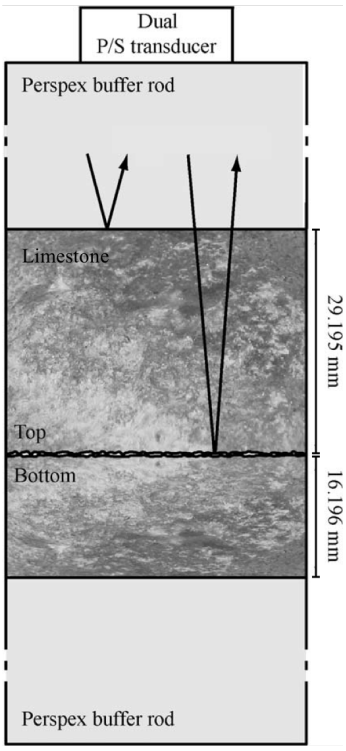

Figure 2.8 Schematic representation of a laboratory experiment made in a hydraulic pressure cell. The sample is a cut limestone sample, sandwiched between perspex buffer rods and imaged using a *P*- and *S*-wave transducer. Modified from Lubbe et al. (2008).

2.3.2 Synthetic media

In order to better constrain the parameters influencing rock physics mechanisms and their response to fractures, some studies have used synthetic fractured media in the laboratory. Using ultrasonic measurements, Hsu and Schoenberg (1993) investigated synthetic samples containing discontinuities that simulated a transversely isotropic medium. Initially, air-saturated fractures showed $0.8 < Z_N/Z_T < 1$. The effect of air substitution with honey tended to decrease the fracture compliance ratio, such that $Z_N/Z_T < 0.1$. The reduction of Z_N/Z_T is here mainly due to the drop of the normal fracture compliance with the introduction of an incompressible fluid.

Rathore and Fjaer (1994) constructed a synthetic rock sample, which consisted of sand cemented by epoxy resin, containing discrete disc-shaped voids, acting as isolated cracks. Verdon

and Wüstefeld (2013) derived a value for $Z_N/Z_T = 0.46$, using the best-fit parameters that Hudson et al. (2001) computed to fit the ultrasonic measurements of Rathore and Fjaer (1994).

More recently, Far et al. (2014) measured ultrasonic velocities on a stack of plexiglass plates, with and without rubber inclusions. Experiments with inclusions show lower values of fracture compliance ratio than experiments without rubber discs, $0.01 < Z_N/Z_T < 0.25$ and $0.11 < Z_N/Z_T < 0.91$, respectively. They showed that this increase of Z_N/Z_T when the fractures are air-saturated is controlled by a decrease of Z_T, but did not explain the mechanism.

Finally, Choi et al. (2014) investigated the effect of fracture faces roughness on the shear to normal stiffness ratio (noted κ_x/κ_z in Choi et al. (2014), which is equivalent to Z_N/Z_T). Ultrasonic measurements were performed on gypsum and lucite specimens containing sandpaper acting as a synthetic fracture. The experiment was repeated with different sandpapers of distinct grit sizes. They observed that for polished fracture faces, $0.3 < Z_N/Z_T < 1.2$, while for sandpapered surfaces, $0.08 < Z_N/Z_T < 0.4$. Their results showed the role of shear contact geometry on Z_N/Z_T.

2.3.3 Field experiments

Field estimates of Z_N/Z_T are still sparse in comparison with the wide range of data from laboratory measurements. They can be classified into two main groups. The first is active surveys made on fractured outcrop, and the second comes from passive monitoring of hydraulic fracture stimulation (i.e., fracking).

Refraction surveys have been conducted on bare rock platforms where discrete fractures outcrop at the surface. Hobday and Worthington (2012) carried out a hammer seismic survey on a sandstone wave-cut platform containing two orthogonal sets of sub-vertical fractures, finding $Z_N/Z_T < 0.1$. Similarly, Foord et al. (2015) used *P*-wave refraction to image two orthogonally oriented fracture sets, finding $Z_N/Z_T = 0.37 \pm 0.06$. Both Foord et al. (2015) and Hobday and Worthington (2012) assumed saturated (at least partially) fractures due to the proximity of the two survey sites with the shore. Foord et al. (2015) also conducted a *P*- and *S*-wave

refraction survey on fractured rock buried few meters below the surface, on the Clifton Downs near the Avon Gorge, South West England. They found $Z_N/Z_T = 0.75 \pm 0.10$. The location of the survey site, at the top of the gorge, and the dry conditions during the seismic experiment, suggested that the fractures were mostly drained.

In the last decade passive seismic techniques have been increasingly used to monitor hydraulic fracturing operations. Microseismic events are generated by fracture stimulation and can be detected through downhole or surface sensor arrays (e.g., Chambers et al., 2010; Maxwell, 2010; Wuestefeld et al., 2011b).

Verdon and Wüstefeld (2013) developed a method to invert shear-wave splitting (SWS) measurements, made during the hydraulic fracturing of a tight gas reservoir, for Z_N/Z_T. They initially found $Z_N/Z_T = 0.74$ for the entire stimulation period. By analysing the data as a function of time, they observed variations in Z_N/Z_T related to the timing of fracture stimulation, and especially $1 < Z_N/Z_T < 2$ corresponding to the timing of proppant injections. Similarly, Baird et al. (2013b) inverted SWS measurements made during a multi-stage hydraulic stimulation in a tight-gas sandstone field. They found $Z_N/Z_T = 0.3$ in the early stage of the fracture stimulation and $Z_N/Z_T = 0.6$ in the latter stages. Both Baird et al. (2013b) and Verdon and Wüstefeld (2013) attribute these increases of Z_N/Z_T to a change in their internal architecture as fracture stimulation progresses. The injected fluids reduced surface roughness of fractures by flushing out recrystallised materials and other impurities.

More recently, Yu (2016) estimated $Z_N/Z_T = 2.5$ on a fractured shale reservoir by inverting borehole and surface seismic data. This value is the largest of the existing data and was assumed to correspond to well-connected gas-saturated or dry fractures.

2.3.4 Generalisations from these results

Figure 2.9 presents an overview of the measurements of Z_N/Z_T existing in the literature and detailed above. Typical values range between 0 and 2, but values up to 3 have been reported (Yu, 2016; Sayers and Han, 2002). These studies demonstrate that the previously held assumption

of $Z_N = Z_T$ is generally not correct.

From this broad range of measurements of fracture compliance made at different scales, using distinct approaches, it is possible to make some generalisations in using Z_N/Z_T as a indicator of the fracture conditions. Table 2.2 summarises the effect of fracture and fluid properties on Z_N/Z_T.

Changing the fluid saturating the fractures changes Z_N/Z_T. The introduction of a stiff fluid into dry fractures tends to reduce Z_N/Z_T, by decreasing Z_N and leaving Z_T almost unchanged. This implies that the fluid is viscous and/or the fractures are not well connected, so that the fluid cannot leave the fractures when the stress is applied.

A change in Z_N/Z_T *can also results from a change in the fracture network connectivity.* By generating new fractures or opening pre-existing ones, for example by hydraulic fracturing or thermal damaging, Z_N/Z_T tends to increase significantly.

The internal architecture of the fractures also influence Z_N/Z_T. Rough fracture surfaces have smaller Z_N/Z_T than smooth or polished ones. The presence of inclusions may also reduce Z_N/Z_T, by increasing the compliance in the tangential direction (Z_T).

Reservoir-scale experiments are still very sparse, although estimates of Z_N/Z_T have the potential to provide precious information about the bulk modulus of the fluid infill and its ability to flow between fractures and pore spaces. This can add valuable information to microseismic surveys, which provide the location and orientation of fracture sets.

Table 2.2 Effects of fracture properties on Z_N/Z_T. + and − signs indicate high and low values of the corresponding fracture property, respectively. Modified from Kendall et al. (2014).

Low ←	Z_N/Z_T	→ High
+	Saturation	−
+	Fluid stiffness	−
+	Fluid viscosity	−
−	Connectivity	+
+	Mineral infill	−

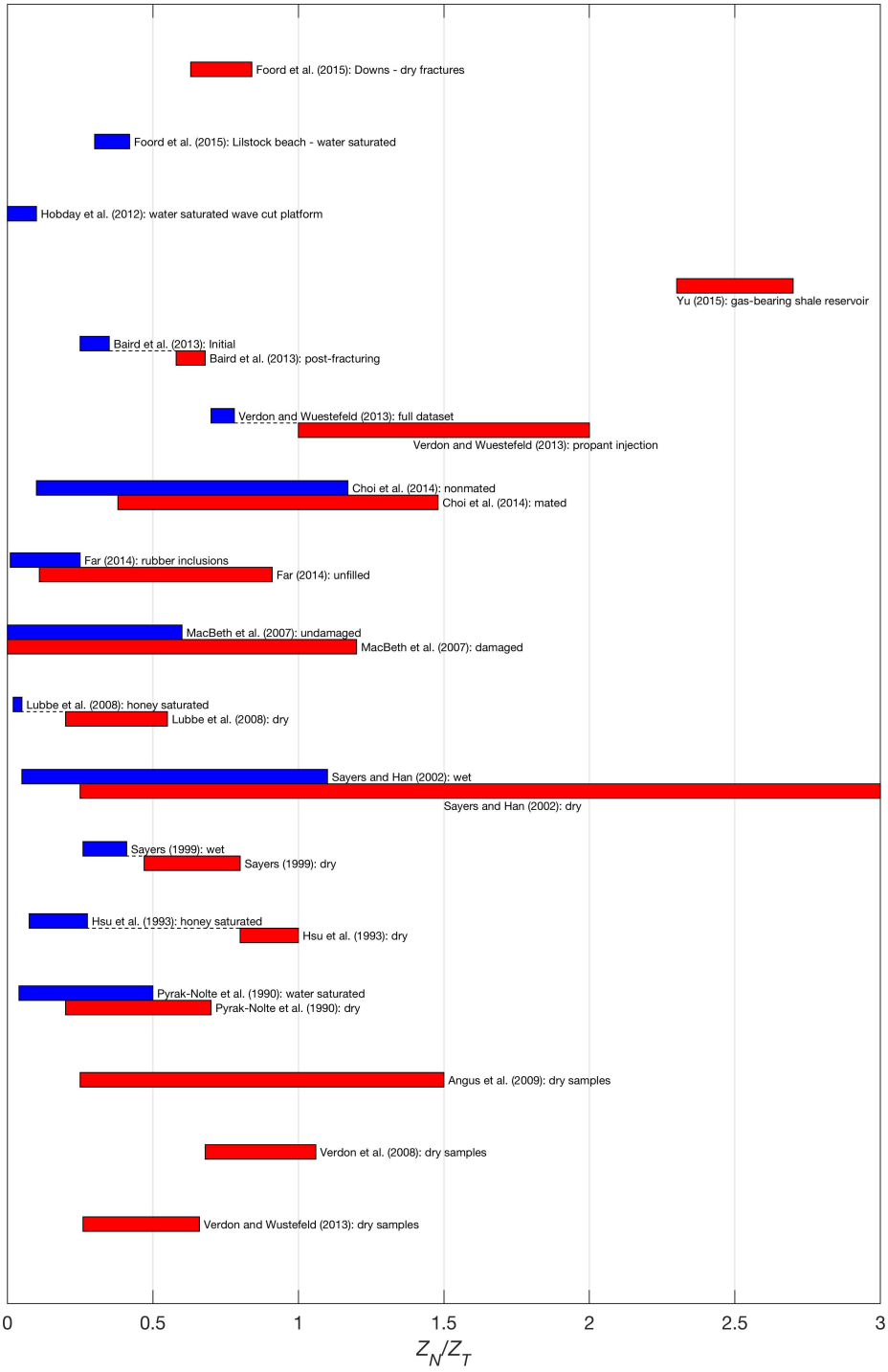

Figure 2.9 Z_N/Z_T inventory. Check Table 2.1 and text for references. Blue bars show wet fractures. Red bars show dry or well-connected fractures. Modified and updated from Foord et al. (2015); Verdon and Wüstefeld (2013) and Choi et al. (2014).

2.3.5 Compliance and fracture size

Some studies have obtained absolute values for both fracture compliance components, Z_N and Z_T. Worthington (2007) and Worthington and Lubbe (2007) shown that a scaling relation exists between the compliance of a single fracture, B_N or B_T (mPa^{-1}), and its length L.

Individual fracture compliance $B_{N,T}$ can be obtained from $Z_{N,T}$ by following the relationship presented by Hobday and Worthington (2012),

$$B_{N,T} = L\, Z_{N,T}, \tag{2.23}$$

where L is the average distance between the fractures of a same set.

Figure 2.10 shows a compilation of laboratory and field data, highlighting that absolute compliance increases with the length of the fractures. Although these data must be considered as order of magnitude estimates (Worthington, 2007), they give qualitative indications about the relation between compliance and length of the fractures. This scaling relation provides insight into fracture properties at reservoir depths, where constraints on fracture size are difficult to obtain. Direct measurements of fracture compliance and size, through log or vertical seismic profiling (VSP) in boreholes, are very specific and localised (e.g., Hardin et al., 1987; Lubbe and Worthington, 2006). However, scaling compliance and length could help estimate fracture properties away from wells. This has the potential to better constrain reservoir physics models, since fracture compliance controls the propagation of seismic waves and seismic anisotropy in fractured medium.

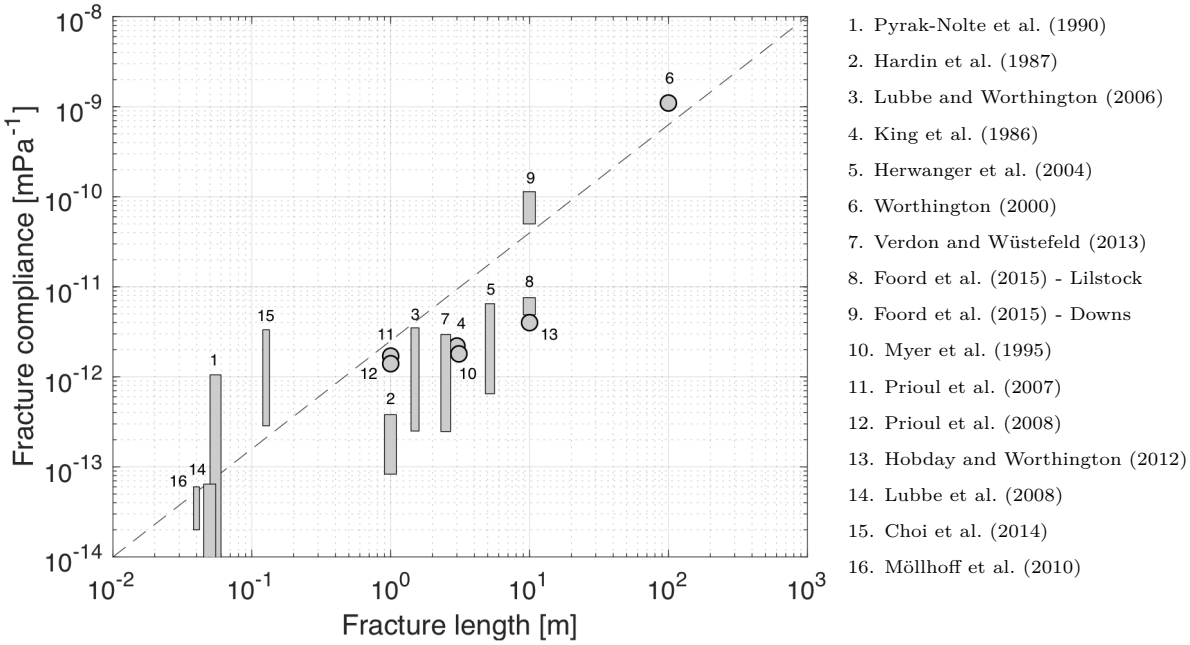

Figure 2.10 Individual fracture compliance as a function of fracture length. Modified and updated from Worthington and Lubbe (2007); Worthington (2007); Verdon and Wüstefeld (2013) and Foord et al. (2015).

CHAPTER 3

Lateral variability in fracture network

Abstract

This chapter describes the mapping and the characterisation of the joints outcropping at the surface of the Lilstock wave cut platform. The mapping was performed by taking a series of aerial photographs with a standard drone. The photographs were merged to create a georeferenced mosaic of the outcrop and the fractures were then digitised by hand. Two distinct sets of joints are present at the surface of the outcrop of interest, the first showing fractures longer than 5 meters striking East-West, and the second including cracks shorter than 1 meter with a more random orientation. Several fracture parameters were quantified, such as length, orientation and intensity. The results highlight significant lateral heterogeneity in the fracture network across the outcrop. In particular, fracture intensity shows variations of from 1 to 13 m^{-1} over a distance of a couple of meters, in relation with their position on the Lilstock anticline. Such results can help better understand the effect of a fracture network on seismic wave propagation and identify source of scattering that can appear in the data.

3.1 Introduction

Fractures are present in most rocks in the upper crust and have a significant influence on their properties such as permeability, porosity, elasticity and strength. Understanding their control on these properties is crucial for the hydrocarbon and geothermal industries (Odling et al., 1999; Vlahovic et al., 2003), as well as for aquifer exploitation (Nascimento Da Silva et al., 2004; Weiss, 2008), hazardous waste storage (Verdon, 2010; Duxbury et al., 2012), and monitoring of fracking operations (Baird et al., 2013b; Kendall et al., 2012).

Studies of fractured outcrop provide valuable insights into reservoir properties and help predict reservoir quality from surface observations (Matthäi and Belayneh, 2004; Odling et al., 1999; Watkins et al., 2018; Awdal et al., 2016). They also represent good sites for seismic experiments, the analysis of wave propagation being a unique tool to characterise fracture properties, such as preferred orientation, density or connectivity (Hobday and Worthington, 2012; Foord et al., 2015; Bamford and Nunn, 1979; Crampin et al., 1980; Inks et al., 2015). Such experiments made on observable fracture sets can help to better understand their impact on seismic anisotropy, as well as calibrate seismic interpretation.

Mapping fractures is then a prerequisite to these applications. Various techniques exist to characterise *in-situ* two-dimensional fracture patterns on outcrops. They can be classified into two main categories: direct measurements and topological sampling.

Direct measurements, also called geometric analysis, involve the quantification and the description of fracture properties such as the number of fracture sets (Belayneh, 2004), as well as fracture orientation (Welch et al., 2015; Watkins et al., 2015; Bowyer and Kelly, 1995), length (Priest and Hudson, 1981; Odling, 1997), aperture (Hooker et al., 2009) or spacing (Renshaw, 1997). Although these techniques can be very time consuming, depending on the extent and the resolution of the mapping, they provide accurate quantitative results. Direct measurements of fracture attributes can be achieved along a linear scanline (Priest and Hudson, 1981; Barbier et al., 2012; Iñigo et al., 2012) or in a rectangular or two-dimensional shaped window (Belayneh

and Cosgrove, 2004). Measurements can be based on photographs taken on the field (Belayneh and Cosgrove, 2004; Engelder and Peacock, 2001), aerial photographs from unmanned aerial vehicles - UAVs (Healy et al., 2016; Peacock and Sanderson, 2018) or satellite imagery (Castaing et al., 1996; Ahmadirouhani et al., 2017), in the case of larger outcrop.

Topological sampling is based on the counting of fracture intersections and terminations (Sanderson and Nixon, 2015; Peacock et al., 2016). Fractures are here described as traces compounded by branches and nodes (Figure 3.1). Nodes can be classified into 3 groups (Manzocchi, 2002) - isolated tips (I), abutments (Y), and cross fractures (X). These individual structures are quantified and served as inputs in a series of equations that estimates fracture set relationship, by computing attributes such as fracture density, intensity and mean length. The topological approach highlights the relationships and interactions between fractures. This can be achieved directly in the field along a circular scanline (Procter and Sanderson, 2017; Mauldon et al., 2001), or by mapping the fracture structures based on photographs (Peacock and Sanderson, 2018).

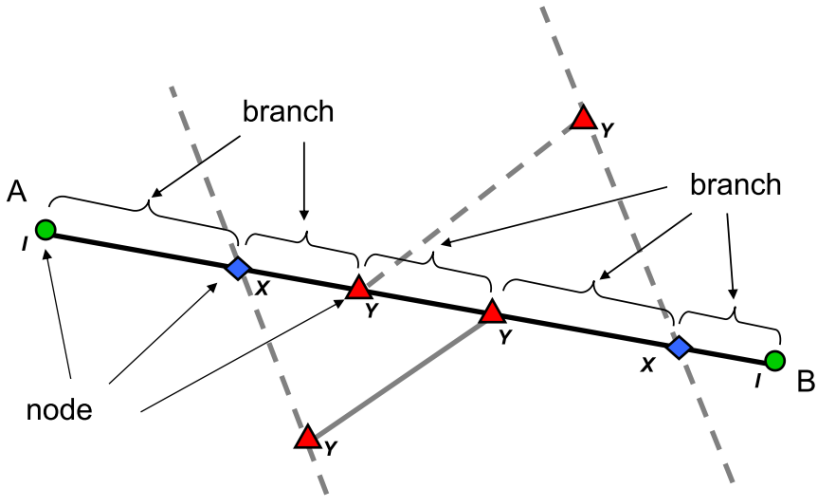

Figure 3.1 Fracture trace (A-B solid line), abutting and cross-cutting fractures (dashed lines), and resulting branches and nodes. Green circles are I-nodes; blue diamonds are X-nodes; red triangles are Y-nodes. From Sanderson and Nixon (2015).

Some surveys use a combination of geometric and topological techniques to map and quantify fracture attributes. Watkins et al. (2015) combined linear and circular scanline methods to measure and count fracture properties at the edge and inside the circle, respectively. Zhang et al. (2016) computed mean trace length by using scanlines into rectangular windows and used the output values to construct a mathematical model.

In this chapter, a characterisation of a fractured outcrop located on the coast of Somerset, United Kingdom, is presented. The analysis is based on a mapping survey using a drone. This area has been intensively studied, including fracture observations on different stratigraphic units (Rawnsley et al., 1998; Belayneh and Cosgrove, 2004; Procter and Sanderson, 2017), as well as on separated outcrops of the same bed along the beach (Belayneh and Cosgrove, 2004). Based on both direct measurements and topological analysis, focus is here on the variability of several parameters of the fracture network inside a window across a single outcrop composed of a single stratigraphic unit. The main objective is to highlight the lateral heterogeneity of a fracture network across the area. In later chapters, these results are compared to estimates of fracture properties derived from seismic measurements.

3.2 Methodology

3.2.1 Lilstock beach

The area of interest is a beach situated on the southern margin of the Bristol Channel Basin (BCB), near the locality of Lilstock (Figure 3.2). It is part of a ~20 km long shore exposure of Mesozoic Blue Lias formation, consisting of alternate layers of limestone and shale (Engelder and Peacock, 2001).

The BCB experiences one of the largest tidal range in the world (Uncles and Cox, 1981; Xia et al., 2010), which provides an excellent coastal exposure of rocks, consisting of a up to 500 m wide wave-cut platform and 20 m high cliff sections. Due to the quality of the outcrops, BCB has been widely studied, including stratigraphy (Simms et al., 2004; Hesselbo and Jenkyns, 1998), palaeontology (Lomax et al., 2018), structural geology (Glen et al., 2005; Brooks et al.,

1988), and seismic anisotropy (Foord et al., 2015).

The formation of the BCB can be summarised in three main stages, the first being basin extension (rifting) during the Jurassic-Lower Cretaceous, with burial and diagenesis (Nemčok et al., 1995). Secondly, a basin inversion took place during the Tertiary, initiated by the Alpine Orogenic collision, including amplification of the folding initially formed during the extension

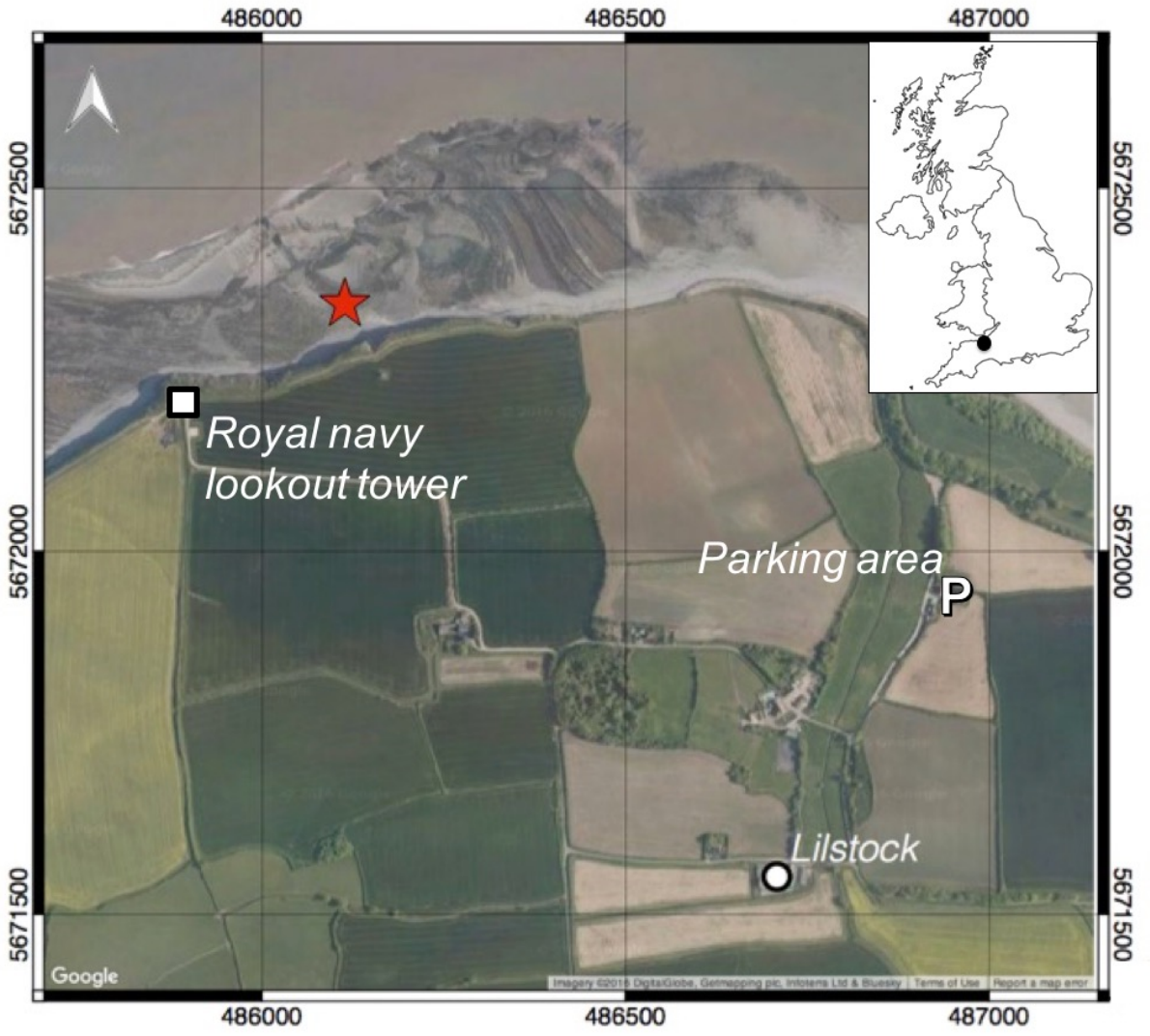

Figure 3.2 Location of the area of interest on the Somerset coast of the Bristol Chanel Basin. The red star shows the location of the mapped outcrop. Coordinates grid: UTM zone 30N. Coordinates units are in meters.

(Dart et al., 1995). The BCB was finally uplifted and exhumed in a multistage process until the Late Paleogene - Neogene (Holford and Turner, 2005), resulting in the present-day configuration (Kamerling, 1979; Van Hoorn, 1987). One of the primary observable features of this geological sequence is the Lilstock buttress anticline. This anticline is asymmetric, as typically observed for rollover anticlines, with a gently dipping south limb and a more inclined northern limb (Belayneh, 2003).

Various fracture patterns have been observed along the beach in different beds, due to their relative position to the anticline (Engelder and Peacock, 2001) or the thickness of limestone horizons (Belayneh and Cosgrove, 2004). Although micro-veins appeared during the extension stage (Belayneh and Cosgrove, 2010; Peacock, 2004), major tectonic features formed during the basin inversion, with long joint sets striking mostly East-West, sub-normal to the compression axis (Engelder and Peacock, 2001). Other sets of smaller joints also formed during the inversion, and mostly consist of non-cross-cutting cracks, roughly perpendicular to the main fractures (Belayneh and Cosgrove, 2004; Engelder and Peacock, 2001). Such fracture sets are common in asymmetric anticlines (Figure 3.3). The joint sets generally terminate at the limestone-shale boundaries, due to the distinct mechanical properties of the two lithologies (Belayneh and Cosgrove, 2004).

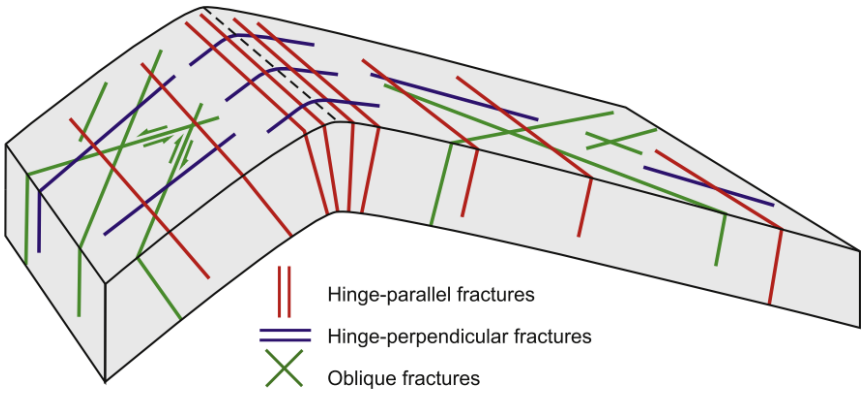

Figure 3.3 Price (1966) classification for fracture patterns observed on asymmetric anticlines. From Awdal et al. (2016), modified from Price and Cosgrove (1990).

Rawnsley et al. (1998) observed an anticlockwise rotation of the joint strike during BCB formation, suggesting a similar rotation of the stress field during the inversion. However, Belayneh and Cosgrove (2004) suggested a simpler mechanism of formation, consisting in one single and constant N-S basin inversion. As the formation history is not clear and still debated (Belayneh and Cosgrove, 2010), further work must focus on characterising the complex joint network around Lilstock.

The outcrop described in this chapter (51°12′7.44″N, 3°11′55.27″W) is located 1.21 km West from the parking area, and 0.27 km East from the military tower (Figure 3.2). It consists of a 20 × 25 m^2 rectangle situated at the eastern edge of the hinge of the Lilstock buttress anticline described by Engelder and Peacock (2001), on the upper part of the wave-cut platform (Figure 3.4), in front of the boulders present at the foot of the cliff (Figure 3.5).

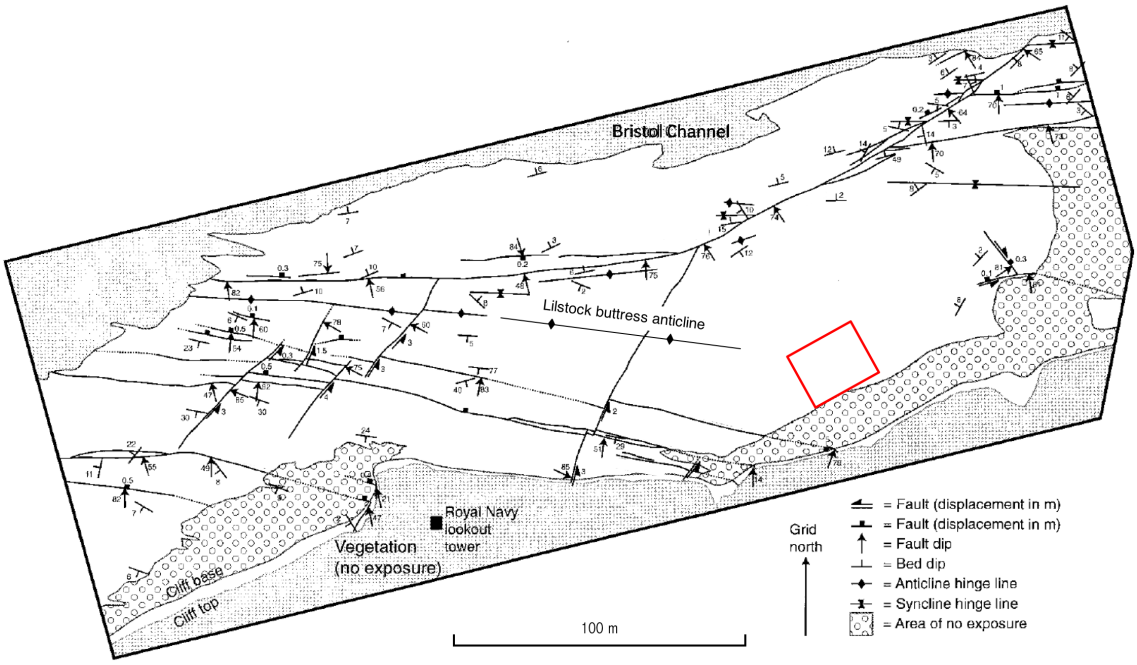

Figure 3.4 Structural geology map of Lilstock modified from Engelder and Peacock (2001). The red square shows the location of the outcrop of interest.

The study outcrop is composed of two 15 cm thick horizontal beds of limestone containing vertical fractures, overlaying a layer of shale. It contains one main set of sub-vertical joints,

Figure 3.5 Picture of the site location taken from the top of the cliff. Red square delimits the outcrop of interest, yellow line shows the hinge of the Lilstock buttress anticline. Boulders can be seen in the foreground.

broadly striking East-West (Figure 3.6a). These joints are consistent with the Alpine joints described by (Belayneh and Cosgrove, 2004), which are located in the hinge region of the Lilstock anticline and are subparallel to the fold axis. A secondary set of smaller joints outcrops, with at first sight no defined preferred orientation (Figure 3.6b). They generally do not cross cut the main fractures and are partially or totally cemented.

This particular outcrop was selected due to its good exposure. The horizontal bedding also minimises the bias caused by optical deformation due to dipping while taking photographs from the drone. Furthermore, the large flat area allows the deployment of a network of geophones for

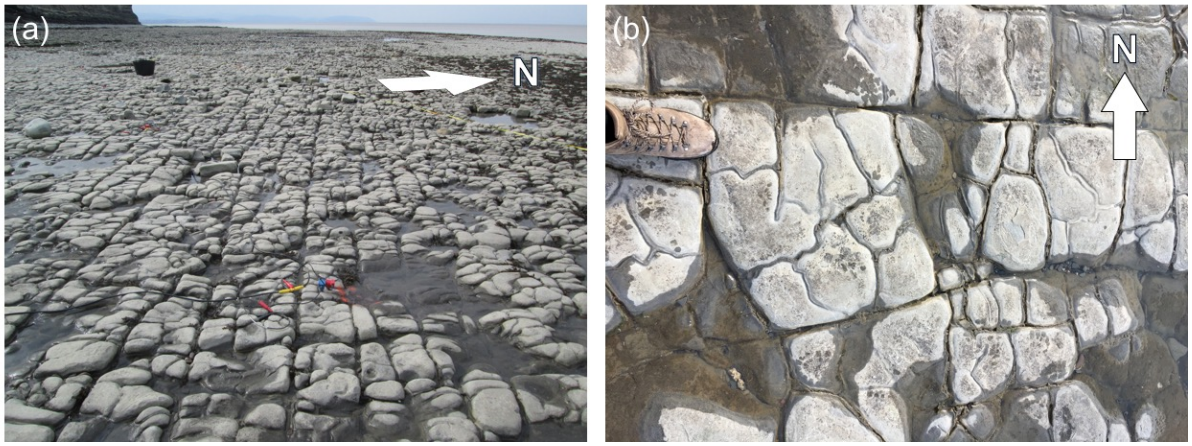

Figure 3.6 Fracture and crack sets on the outcrop of interest. Observed (a) long fractures striking roughly E-W and, (b) non-crossing cracks showing no obvious preferred orientation.

the seismic experiment (See Chapter 4).

For the purpose of this chapter, the generic terms 'fracture' and 'crack' will be used to refer to the E-W sets of long joints, and to the intermediate set of short joints, respectively.

3.2.2 Data acquisition

On 6 November 2017, the outcrop of interest was mapped using a drone in order to quantify fracture attributes, such as preferred orientation, length, intensity, and connectivity.

Aerial photographs were acquired using a DJI™ Phantom 3 Standard drone, equipped with a 12 megapixels built-in camera installed on a stabilisation gimbal (Figure 3.7). Removable propellers, lightweight design and small dimensions of the aircraft make it easily transportable to the field in a small backpack.

The drone was remotely controlled using the DroneDeploy application (available online: www.dronedeploy.com), which allows automated flight, including take off, photographs acquisition and landing. DroneDeploy uses Google Maps and Global Positioning System (GPS) to establish a flight plan. Parameters such as flight path and flight altitude, as well as forward and lateral overlap between photographs were pre-defined (see Table 5.1 for flight parameters).

Figure 3.7 DJI Phantom 3 Standard drone and built-in camera used for the mapping survey.

Table 3.1 Input flight parameters.

Path length [m]	350
Altitude [m]	20
Lateral overlap [%]	66
Forward overlap [%]	80

As a result, the drone took a total of 56 photographs covering an area of ~5000 m^2, including the outcrop of interest, in less than 5 minutes. The photographs were then merged using the online DroneDeploy platform to create a georeferenced photomosaic of the outcrop, with a resolution of 1 cm per pixel (Figure 3.8).

3.2.3 Fractures and cracks characterisation

The cracks and fractures of the area of interest were manually digitised into the QGIS[1] environment by creating a line shape file on top of the aerial photograph (Figure 3.9). Although it is a time-consuming method, it avoids misinterpretations, mainly caused by the presence of boulders and water at the surface. These artefacts are responsible for the large blank areas visible on the vector plot. The line width of the vectors in Figure 3.9 is not true to scale and

[1]QGIS is an open source Geographical Information System application (http://www.qgis.org/)

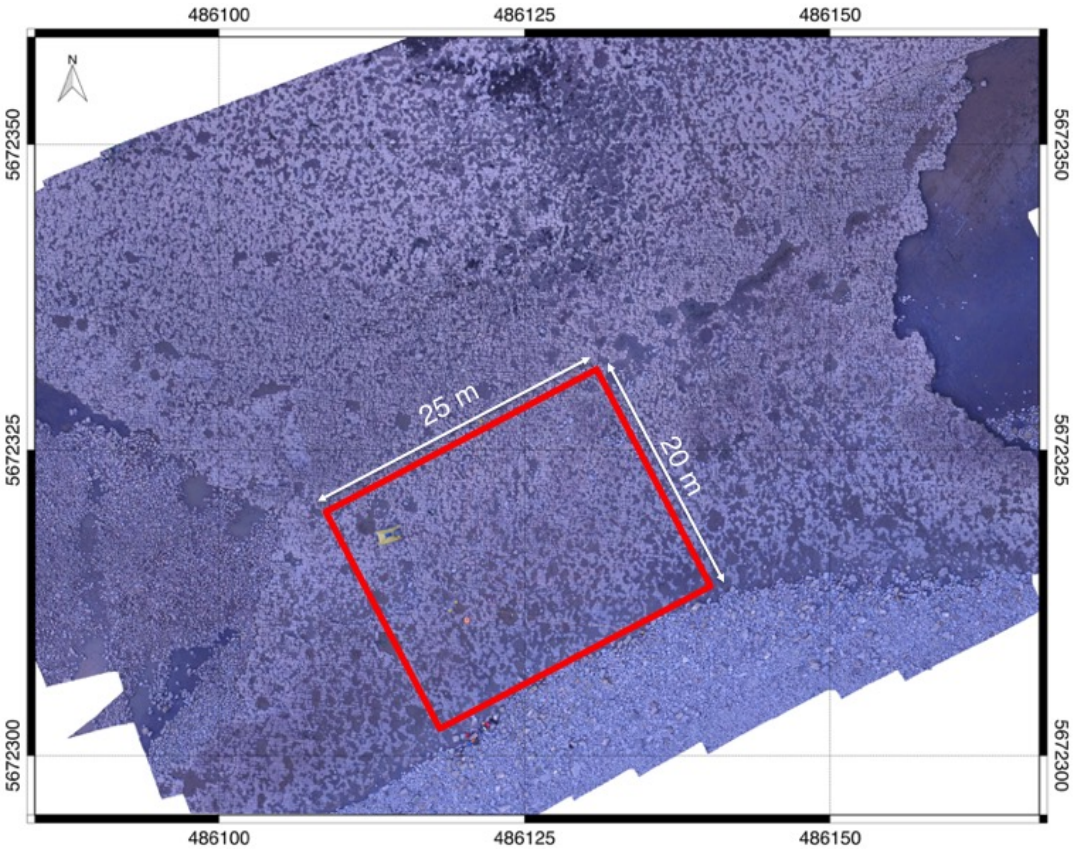

Figure 3.8 Photomosaic of the wave cut platform at Lilstock. The red square delineates the outcrop of interest. Coordinates grid: UTM zone 30N. Units are in meters.

different joint apertures were observed on site. The aperture varies between 3 to 4 mm for the cracks, and is about 5 mm for the long fractures striking East-West. Fractures extending outside the delineated rectangle were cropped.

The analysis of the vectorised fractures and cracks was performed using two different softwares packages. I used the QGIS Line Direction Histogram plugin (Tveite, 2015) to quantify fracture and crack orientation and the FracPaQ MATLAB^{TM} toolbox (Healy et al., 2016) to estimate other attributes such as length, intensity and connectivity.

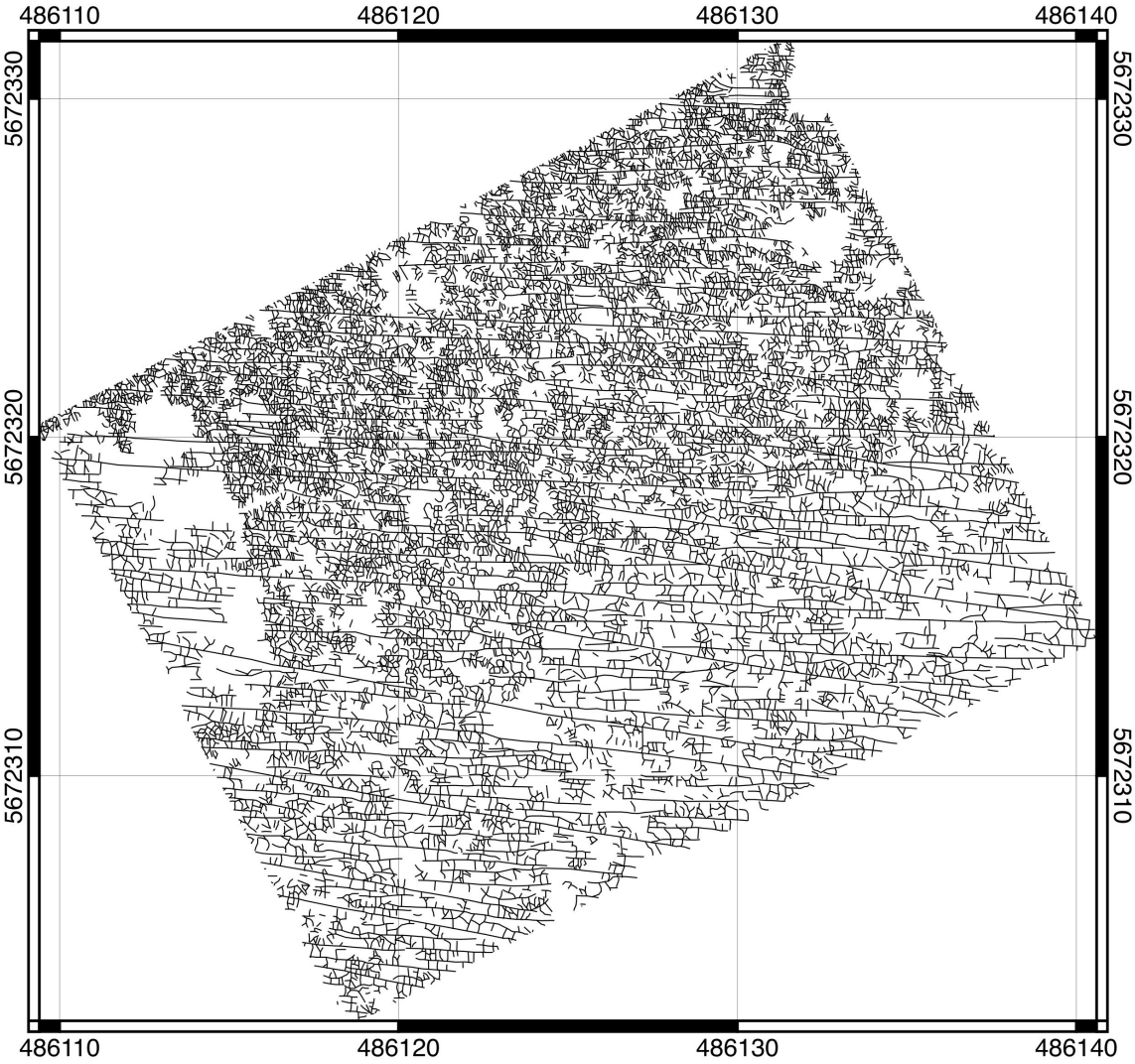

Figure 3.9 Fracture traces on the Lilstock outcrop (see red square on Figures 3.2 and 3.4 for location). Note that the thickness of the lines is not true to scale and overestimate the width of the fractures and cracks. Coordinates grid: UTM zone 30N. Units are in meters.

3.2.3.1 Fracture orientation

In the scope of this project, I am particularly interested in determining fracture and crack orientation to better understand the seismic anisotropy observed on the Lilstock outcrop (See Chapter 4). With the shape file of the vectorised fractures as an input, the QGIS Line Direction Histogram plugin creates a rose diagram that displays the distribution of the directions of

the fracture and crack branches. The direction bins are weighted on branch lengths, which means that the accumulated lengths of the line branches for each bin determines the shape of the histogram. The rose diagram is normalised, so that the maximum value of the direction bins corresponds to the sector with the maximum length, and the lengths of the sectors of the remaining bins are scaled proportionally.

3.2.3.2 Fracture length

Length is the commonly used parameter to define the joint size in surveys from surface observations (Dershowitz and Einstein, 1988; Rohrbaugh et al., 2002). Outcrops generally exhibit a wide range of lengths, especially when several fracture sets are present (Healy et al., 2016; Odling, 1997). Different sets have distinct mean length, according to their mechanical formation process. For example, at Lilstock, N-S joints formed during the post-Alpine uplift are short in comparison with long E-W joints formed during the basin inversion (Belayneh, 2003). Quantifying joint length is also relevant as it can be an important parameter for elastic properties, such as fracture compliance, which was shown to exhibit scaling relationships (Worthington and Lubbe, 2007).

3.2.3.3 Fracture intensity

Fracture intensity is noted P_{21} (Sanderson and Nixon, 2015; Zeeb et al., 2013). The P_{xy} notation refers the the x^{th} dimension of the sampling region, and the y^{th} dimension of the feature. P_{21} gives an estimate of fracture abundance in a determined area. Fracture intensity can be mathematically described as the total length of trace segments per unit area (Dershowitz and Einstein, 1988; Rohrbaugh et al., 2002) and is here calculated for each cell (pixel) of the map, following the equation,

$$P_{21} = \frac{\sum_n L_n}{A}, \tag{3.1}$$

where L_n is the length of the n^{th} fracture or crack trace present inside a circle of area A (Figure 3.10). Here a search circle with a radius equal to 1.0 m is used.

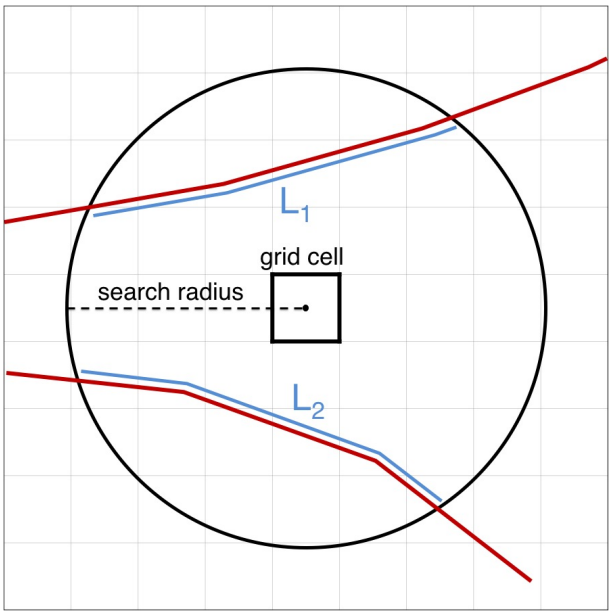

Figure 3.10 Search circle used to determine joint intensity by computing the total length of joint segments around a grid cell. Red lines show the joints intersecting/intercepting the search circle. Blue lines show the n joint segments of length L_n inside the search circle (Equation 5.1).

3.2.3.4 Fracture connectivity

By analysing the relative amount of Y-, X-, and I-nodes present on the fracture network, it is possible to infer the degree of connectivity of the outcrop. A well connected fracture network will have a Y:X:I ratio dominated by the X-nodes, whereas a network of isolated, non cross cutting fractures will be dominated by I-nodes. The proportion of the three types of nodes can help describe the fracture and crack network. Results are generally plotted on a triangular or ternary diagram (Procter and Sanderson, 2017; Healy et al., 2016; Sanderson and Nixon, 2015; Manzocchi, 2002).

3.3 Results

Figure 3.11 shows the orientation of the fracture and crack branches, vectorised based on the aerial photographs. The rose diagram highlights the dominance of the long fractures striking in the West-East direction, as first observed in the field. Although shorter cracks are present at

every angle, as also reported by Rawnsley et al. (1998) at Lilstock beach, they here tend to slightly dominate in the North-South direction.

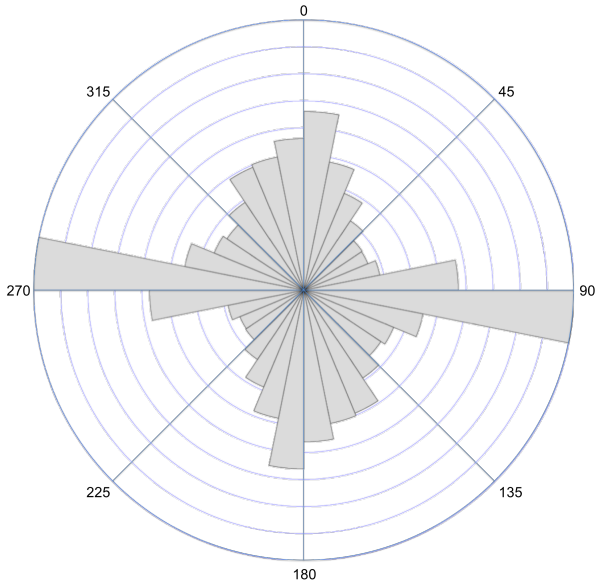

Figure 3.11 Rose diagram showing the orientation of the fracture and crack branches in degrees from North, normalised and weighted on length.

Figure 3.12 shows a histogram and the cumulative frequency of joint lengths for the mapped area. Due to the presence of two sets (fractures and cracks), trace lengths range over two orders of magnitude. Furthermore, it must be noted the dominance of smaller cracks versus long fractures, as highlighted by the low percentages of fractures longer than 1 meter in Figure 3.12a. Fractures longer than 5 meters represent less than 0.1 % of the total number of joints present on the outcrop. More than 90% of the traces are cracks smaller than 1 meter, and the mean trace length is about 0.31 m. The longest fracture is almost 22 m long and is part of a longer feature cropped by the sampling window, as it is the case with many of the E-W fractures. The slope of the log-log cumulative frequency of trace length (Figure 3.12b) presents a power-law distribution, which is common in most rock systems composed of several sets of cracks and fractures (Sanderson and Nixon, 2015; Healy et al., 2016; Odling et al., 1999).

Figure 3.13 shows the fracture intensity across the mapped outcrop. Heterogeneity is well marked, with the area north of the anticline hinge showing an intensity 1 order of magnitude

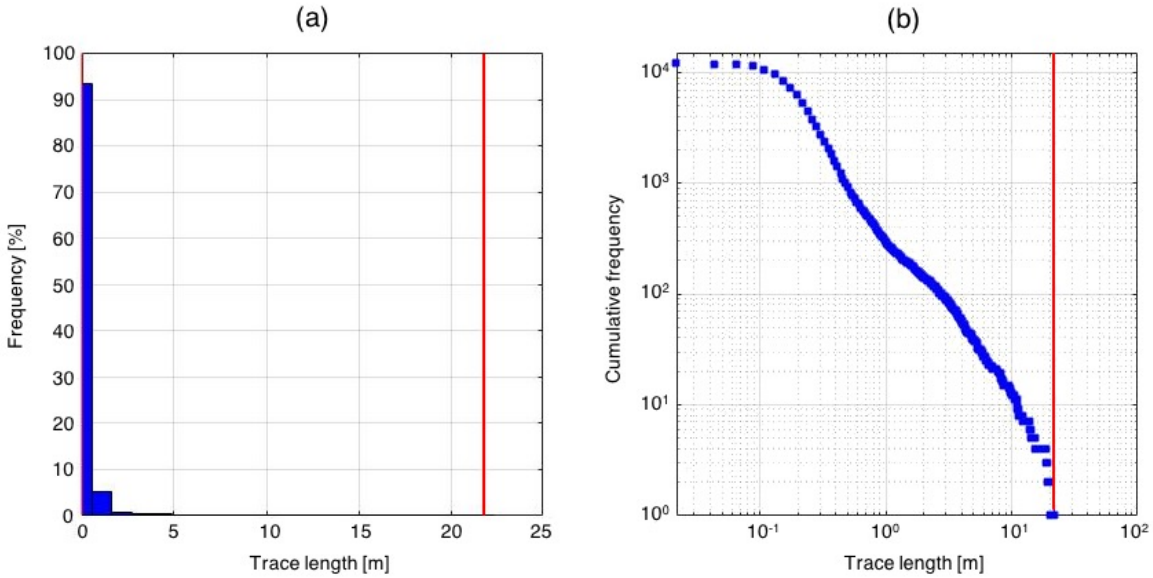

Figure 3.12 Fracture length on the Lilstock outcrop. (a) Histogram and (b) log-log plot of fracture lengths. Red lines highlight the longest trace inside the mapped rectangle.

larger than the bottom half of the sampled rectangle. Note the presence of very low intensity spots, particularly to the North-East of the outcrop, due to the presence of boulders and water that make the mapping of the fractures and cracks impossible based on the aerial photograph. Also, the low values encountered at the edge of the intensity map are biased due to the cropping of the features outside of the sampling rectangle.

The topological analysis based on the counting of the three types of nodes present on the fracture network highlights a connectivity dominated by Y-nodes (Figure 3.14). The ratio of Y:X:I nodes was determined as 0.65:0.08:0.27, which is representative of a poorly connected network. This lack of connectivity is due to the fact that most of the cracks abut against fractures and do not cross cut them. Such a ratio is generally approximated by ladder or brick-like fracture patterns (Sanderson and Nixon, 2018).

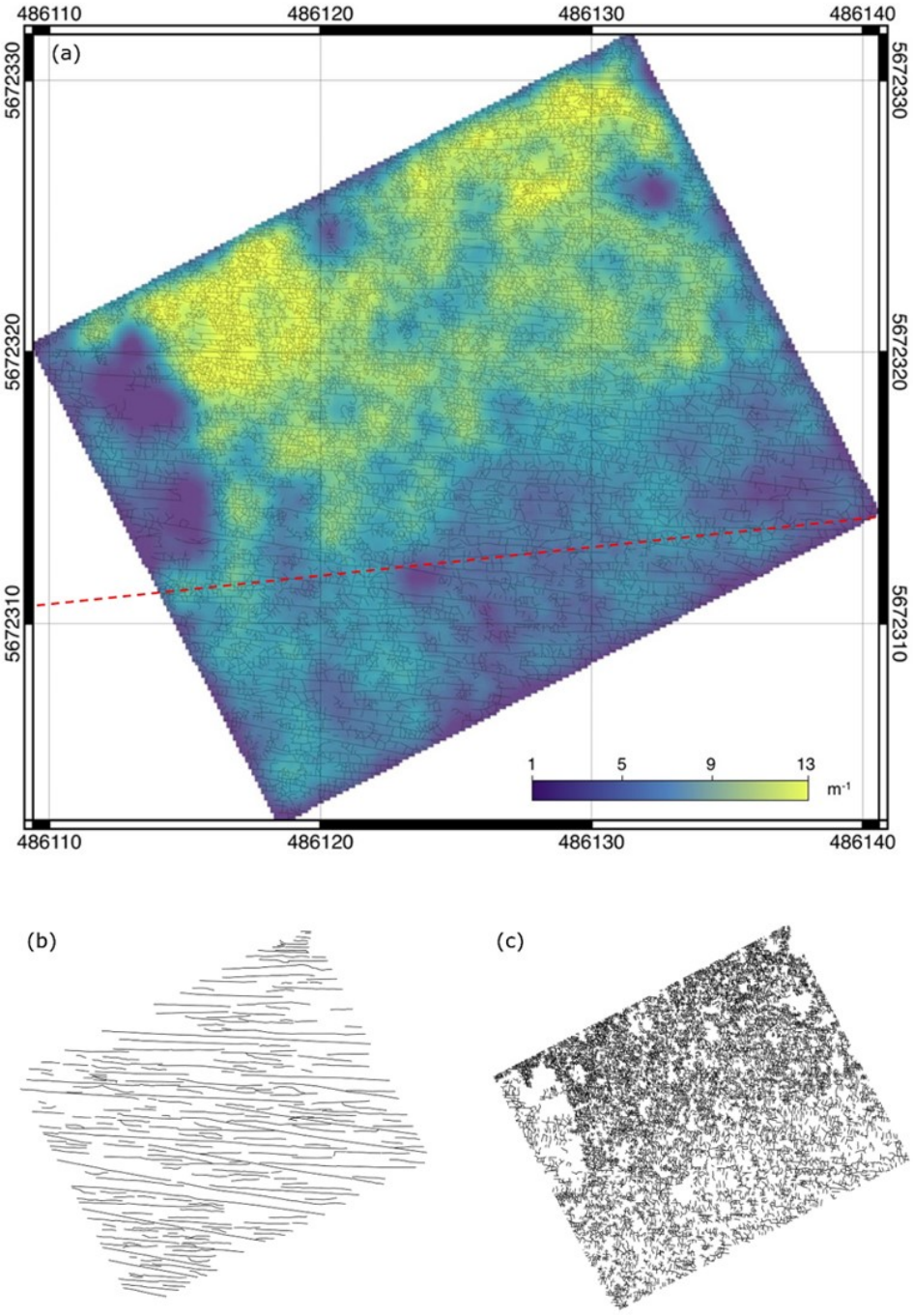

Figure 3.13 (a) Fracture intensity on the Lilstock outcrop. Dashed red line marks the position of the anticline. (b) Long E-W fractures and (c) short cracks on the Lilstock outcrop. Coordinates grid: UTM zone 30N. Units are in meters.

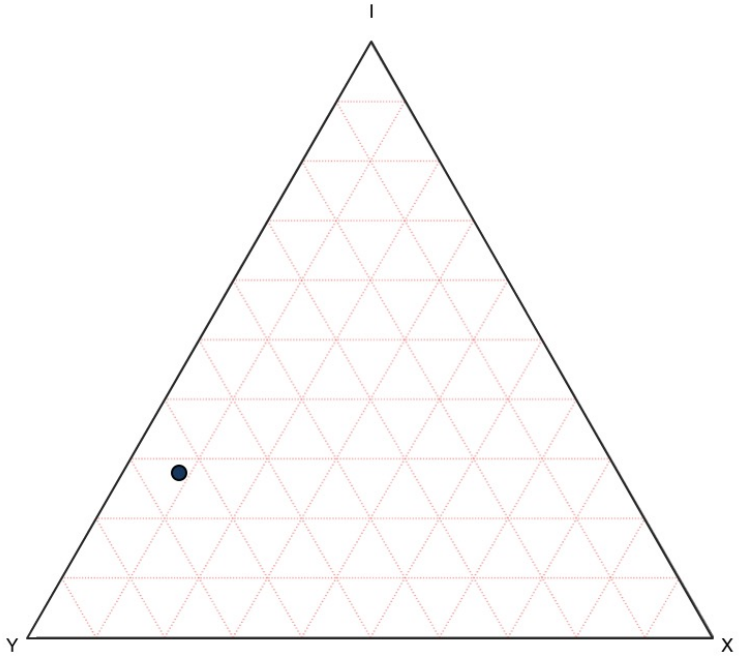

Figure 3.14 Triangular plot of node types proportion on the Lilstock outcrop. Nodes are classified as isolated tips (I), abutments (Y), and cross fractures (X). Note very few of the joints cross each others.

3.4 Discussion

The trace intensity map highlights a significant level of heterogeneity in the fracture and crack network shows (Figure 3.13a). Heterogeneity in intensity of the overall fracture network is controlled by the small cracks (Figure 3.13c), while long E-W fractures show a steady spacing throughout the outcrop (Figure 3.13b). Such heterogeneity in the trace orientation over short distances has been previously observed, even on small outcrops (Watkins et al., 2018, 2015). This heterogeneity is also reflected by others fracture attributes, such as their orientation. Figure 3.15 shows traces orientations for 9 equal subdivisions of the mapped fracture network. Although the dominance of the long fractures striking East-West is consistent over the overall area, note a variation in the distribution of crack orientation at intermediate angles. The 3 rectangles on the bottom part of the map show a strong bi-modality, with a preferred orientation for the cracks along the North-South axis, normal to the fractures. This configuration can

be approximate as a ladder pattern, widely observed around the hinge zone (Engelder and Peacock, 2001; Belayneh, 2004). Moving northward across the outcrop, more of the cracks tends to exhibit a higher degree of isotropy (random orientation). This is particularly true for the 3 sub-rectangles in the top part of the outcrop (Figure 3.15). The variation of the observed orientations, from a bi-axial fracture-crack configuration, to a more isotropic spreading of the cracks, can be related to their relative position on the Lilstock buttress anticline (Figure 3.3). Similar ladder patterns have been observed on the hinge zone of the anticline (Belayneh and Cosgrove, 2004), as well as irregular ladder patterns (Belayneh, 2003), involving a condition of low stress (Rives et al., 1994). Also, different joint patterns and intensities can be explained by variations in bed thickness (Peacock and Mann, 2005), although a systematic relationship is difficult to establish (Belayneh, 2003).

3.5 Conclusions

A complete characterisation of the joints outcropping on a wave cut platform located on the southern margin of the BCB was performed based on a UAV mapping campaign. The selected outcrop contains a visible joint network, consisting of a single set of long fractures and a more complicated set of small cracks, striking E-W and N-S, respectively. The N-S oriented crack set is more diffuse in alignment. The main objective was to quantify joint attributes such as length, orientation, intensity, and connectivity. Although the mapping was constrained to a small area, the results show strong heterogeneity in the joint network, mainly highlighted by the lateral variation of the fracture intensity. These observations will help interpretating seismic anisotropy measured at the outcrop (Chapter 4) and identify the sources of scatter that the data can exhibit in such experiments. Surface seismic experiments made on fractured outcrop generally present the seismic velocity data as a function of azimuth (Foord et al., 2015; Hobday and Worthington, 2012; Inks et al., 2015; Bamford and Nunn, 1979; Nunn et al., 1983; Crampin et al., 1980). Heterogeneity in the pattern of cracks and fractures across a region can lead to scatter in patterns of seismic anisotropy (Foord et al., 2015).

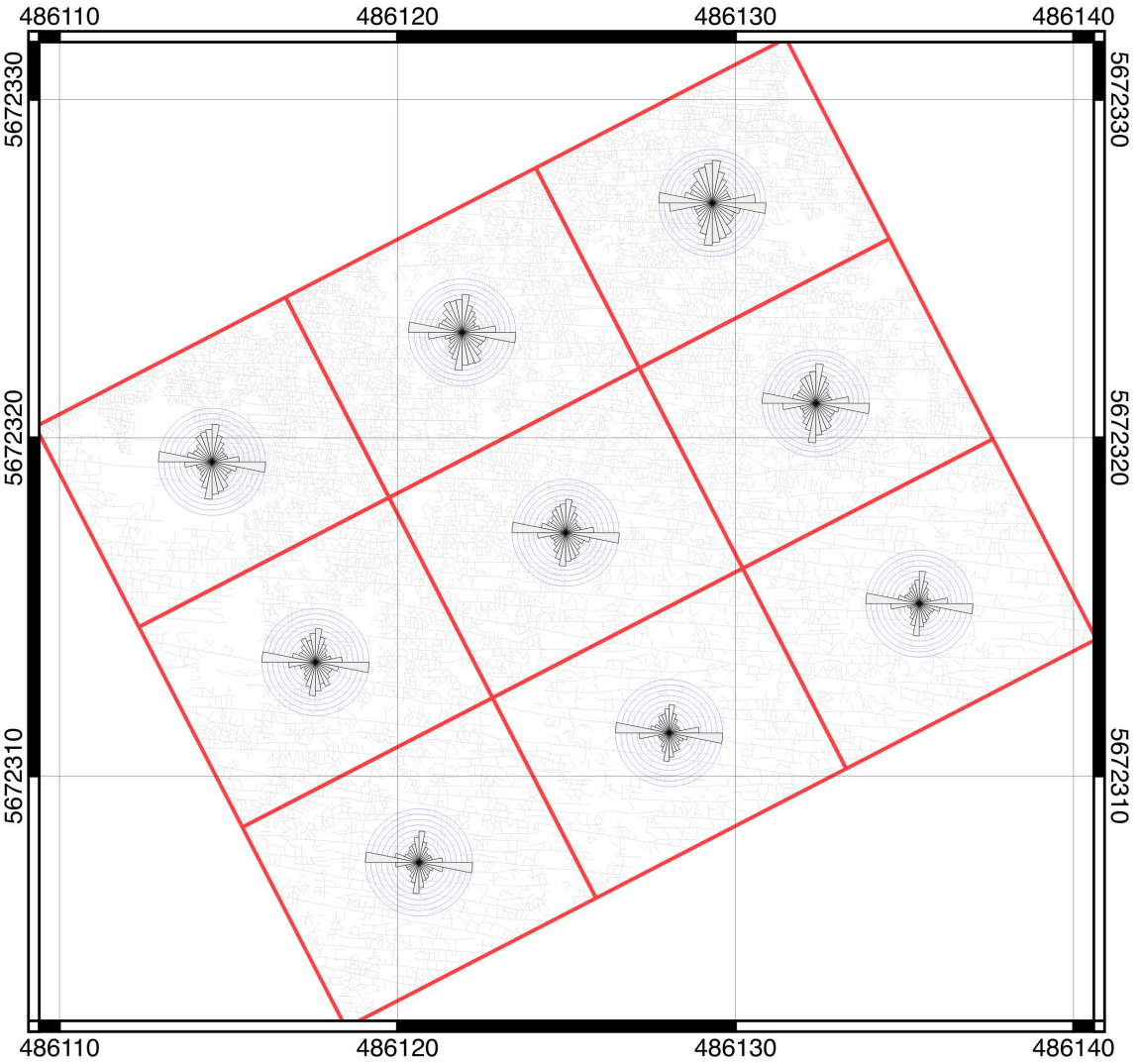

Figure 3.15 Fracture orientation data for 9 rectangular subdivisions of equal area of the Lilstock outcrop. Coordinates grid: UTM zone 30N. Units are in meters.

CHAPTER 4

Field measurements of fracture compliance on a wave cut platform

Abstract

Seismic surveys using hammer sources are used to estimate fracture compliance ratio on a wave-cut platform in Southwest England. The ratio of normal to tangential fracture compliance ratio (Z_N/Z_T) is a good indicator of permeability and can be used to study fluid flow in geological reservoirs. Aligned fracture sets lead to seismic anisotropy which is sensitive to Z_N/Z_T. P- and S-wave velocities are measured at different azimuths to investigate the impact of fractures on the seismic anisotropy. Three pairs (P and S) of surveys were performed after the high tide in order to investigate the effect of water draining on the fracture compliance. Seismic velocities increase as the water drains, an effect attributed to a reduction in the effective density of the medium. Systematic variations in Z_N/Z_T are also observed over the three surveys: $Z_N/Z_T{}^{(1)} = 0.18$, $Z_N/Z_T{}^{(2)} = 0.40$, $Z_N/Z_T{}^{(3)} = 0.48$. The increase is mainly due to a dramatic drop of the tangential component in the fracture compliance (Z_T). These variations are attributed to a decrease in the water content of the main fracture

set as the tide retreats, as well as a loss in lubrication, as the fractures are filled with clay.

4.1 Introduction

Fractures can control and enhance the permeability and the porosity of a material. This particularly includes the migration of fluids in geological reservoirs, such as magma in volcanic settings, water in geothermal fields, or hydrocarbon in sedimentary rocks (Vlahovic et al., 2003; Tang et al., 2005; Harris et al., 2005; Jupe et al., 2003; Khelifa et al., 2014). Fracture-related fluid flow is of crucial concern due to the recent development of underground waste storage (Duxbury et al., 2012; Verdon and Wüstefeld, 2013; Stork et al., 2015) and hydraulic fracking (Wuestefeld et al., 2011b; Baird et al., 2013b). Therefore, imaging fractures is of significant importance. Reflection seismology is commonly used to image fractures (Lynn and Thomsen, 1990; Hall et al., 2002). More recently microseismicity has been used to study fracturing (Teanby et al., 2004a; De Meersman et al., 2009; Maxwell and Urbancic, 2001; Duncan and Eisner, 2010).

Aligned fractures lead to seismic anisotropy, when the velocity of the seismic waves depends of the direction of propagation. This effect of fracture networks on seismic wavespeeds is controlled by the fracture compliance, which can be resolved into their normal and tangential (or shear) components, Z_N and Z_T, respectively (Schoenberg and Sayers, 1995). The fracture compliance ratio, Z_N/Z_T [1] has been demonstrated to be an effective indicator of fluid content and permeability in fractured media (Verdon and Wüstefeld, 2013; Baird et al., 2013b). However, interpreting fracture compliance is not an easy task, as it can be influenced by various fracture properties, such as internal architecture, connectivity and fluid viscosity. A review of existing Z_N/Z_T measurements has been published by Verdon and Wüstefeld (2013) and updated by Foord et al. (2015) and Choi et al. (2014). Most of these published data are derived from laboratory experiments made on core samples (Angus et al., 2009; Macbeth and Schuett, 2007) or synthetic media (Rathore and Fjaer, 1994; Far et al., 2014). As raised by Worthington and Lubbe (2007), field measurements are important in addressing upscaling concerns.

[1] also noted Ω (e.g., Foord et al., 2015)

In this chapter, azimuthal seismic anisotropy on a fractured beach rock is investigated using a hammer source to acquire shallow refraction profiles. The rock exposes at the surface and fracture attributes, such as strike, length, intensity, and spacing, can be mapped and quantified. These observations are used to constrain the rock physics model and better interpret the source of anisotropy. Furthermore, the effect of the tide on the fracture saturation and fracture compliance is also investigated.

4.2 Methods

4.2.1 Inversion of measured seismic velocities for fracture compliance

Measurements of anisotropy cannot be directly used to characterise fracture sets, as other mechanisms can induce anisotropy, such as grain alignment (Johansen et al., 2004), crystal preferred orientation (Kendall et al., 2007; Valcke et al., 2006), and sedimentary layering (Backus, 1962; Bakulin, 2003). The observed anisotropy must be related to the cause using rock physics models. Inversion approaches are then used to recover fracture compliance parameters from seismic measurements made on the fractured medium (Al-Harrasi et al., 2011; Verdon et al., 2009; Bakulin et al., 2000; Wuestefeld et al., 2011a; Verdon and Kendall, 2011; Kendall et al., 2012).

To predict the behaviour of seismic waves in a fractured medium, a rock physics model is built, with background embedded with fractures. Fracture parameters include orientation, density, and the compliance ratio. To find the best fitting model, an inversion is performed by doing a grid search over crack density ξ and Z_N/Z_T to find the values that minimise the root mean square (RMS) misfit between measured and modelled velocities. The model construction is based on the widely used additional compliance approach introduced by Schoenberg and Sayers (1995), which considers fractures as poorly bonded interfaces representing displacement discontinuities. The overall compliance of a fractured medium ($\mathbf{S}$) can be represented as the sum of the compliance of the intact background ($\mathbf{S}_b$), and the fracture compliance ($\mathbf{S}_f$),

$$\mathbf{S} = \mathbf{S}_b + \mathbf{S}_f, \tag{4.1}$$

where $\mathbf{S}$, $\mathbf{S}_b$, and $\mathbf{S}_f$ are 4^{th} order, $3 \times 3 \times 3 \times 3$ tensors.

In the case of the presence of m sets of aligned fractures, the equation can be rewritten, as,

$$S_{ijkl} = S_{ijkl_b} + S^{(m)}_{ijkl_f}, \tag{4.2}$$

where,

$$S^{(m)}_{ijkl_f} = \frac{1}{4}\sum_m (Z^{(m)}_{ik} n^{(m)}_l n^{(m)}_j + Z^{(m)}_{jk} n^{(m)}_l n^{(m)}_i + Z^{(m)}_{il} n^{(m)}_k n^{(m)}_j + Z^{(m)}_{jl} n^{(m)}_k n^{(m)}_i). \tag{4.3}$$

and n_j is the normal to the fracture surface.

If the fractures are considered to be rotationally invariant and with no preferred slip direction, Z_{ij} is simplified and reduced to a three non-zero elements tensor,

$$Z_{ij} = Z_N n_i n_j + Z_T(\delta_{ij} - n_i n_j), \tag{4.4}$$

where Z_N and Z_T are the normal and tangential fracture compliance, respectively, and δ_{ij} is the Kronecker delta.

The additional compliance due to a single set of vertical aligned fractures striking in the x_1-x_3 plane, is therefore,

$$\mathbf{S}_f = \begin{pmatrix} Z_N & 0 & 0 & 0 & 0 & 0 \\ 0 & 0 & 0 & 0 & 0 & 0 \\ 0 & 0 & 0 & 0 & 0 & 0 \\ 0 & 0 & 0 & 0 & 0 & 0 \\ 0 & 0 & 0 & 0 & Z_T & 0 \\ 0 & 0 & 0 & 0 & 0 & Z_T \end{pmatrix}. \tag{4.5}$$

The crack density, ξ, is related to Z_T by (Hall et al., 2008, based on Guéguen and Schubnel, 2003),

$$Z_T = \frac{\xi}{h}, \tag{4.6}$$

where h is an anisotropic normalizing factor,

$$h = \frac{3E_0(2-\nu_0)}{32(1-{\nu_0}^2)}. \tag{4.7}$$

E_0 and ν_0 are the Young's modulus and the Poisson's ratio of the isotropic background, respectively.

Once the compliance tensor has been computed, it is inverted to get the stiffness tensor, $\mathbf{C}$, as,

$$\mathbf{C} = \mathbf{S}^{-1}, \tag{4.8}$$

which is used in the Christoffel equation to compute P- and S-wave velocities as a function of azimuth. This is done using the MSAT toolbox developed by Walker and Wookey (2012). For

each angle, an inversion is performed, searching for the values that minimise the RMS misfit between measured and modelled seismic velocities.

4.2.2 Lilstock beach

The study area is a beach situated on the southern shore of the Bristol Channel Basin (BCB), near the locality of Lilstock, South West England. It is part of a ~20 km long exposed shore of Mesozoic Blue Lias formation, consisting of alternate layers of limestone and shale (Engelder and Peacock, 2001). The BCB experiences one of the largest tidal range in the world (Xia et al., 2010; Uncles and Cox, 1981), which provides an excellent coastal exposure, consisting of up to 500 m wide wave-cut platform and ~20 m high cliff sections. Due to the quality of the outcrops, BCB has been widely studied, including stratigraphy (Hesselbo and Jenkyns, 1998; Simms et al., 2004), palaeontology (Lomax et al., 2018), structural geology (Brooks et al., 1988; Glen et al., 2005), and seismic anisotropy (Foord et al., 2015).

The formation of the BCB can be summarised in 3 main stages, the first being basin extension, with burial and diagenesis (Nemčok et al., 1995). Secondly, a basin inversion took place, initiated by the Alpine Orogenic collision, including amplification of the folding initially formed during extension (Dart et al., 1995). The BCB was finally uplifted and exhumed, resulting in the present-day configuration (Van Hoorn, 1987; Kamerling, 1979).

Although micro-veins appeared during the extension stage (Belayneh and Cosgrove, 2004; Peacock, 2004), major tectonic features formed during the basin inversion, with long joints striking sub-normal to the compression axis (Engelder and Peacock, 2001). Posterior sets of smaller joints formed after the inversion, and mostly consist of non-cross-cutting cracks, abutting against the older joints. These most recently formed joint sets show various patterns along the beach on different beds, due to their relative position to the anticline or the thickness of the underlying shale horizons (Engelder and Peacock, 2001; Belayneh and Cosgrove, 2004). All joints generally terminate at the limestone-shale boundaries, due to differences in mechanical properties of the two lithologies (Belayneh and Cosgrove, 2004).

The outcrop described in this chapter (51°12′7.44″N, 3°11′55.27″W) is located 1.21 km West of the parking area, and 0.27 km East of the military tower (Figure 4.1). It consists in a 20 × 25 m^2 rectangle located at the eastern edge of the hinge of the Lilstock buttress anticline described by Engelder and Peacock (2001), on the upper part of the wave-cut platform, seaward of the boulders at the foot of the cliff.

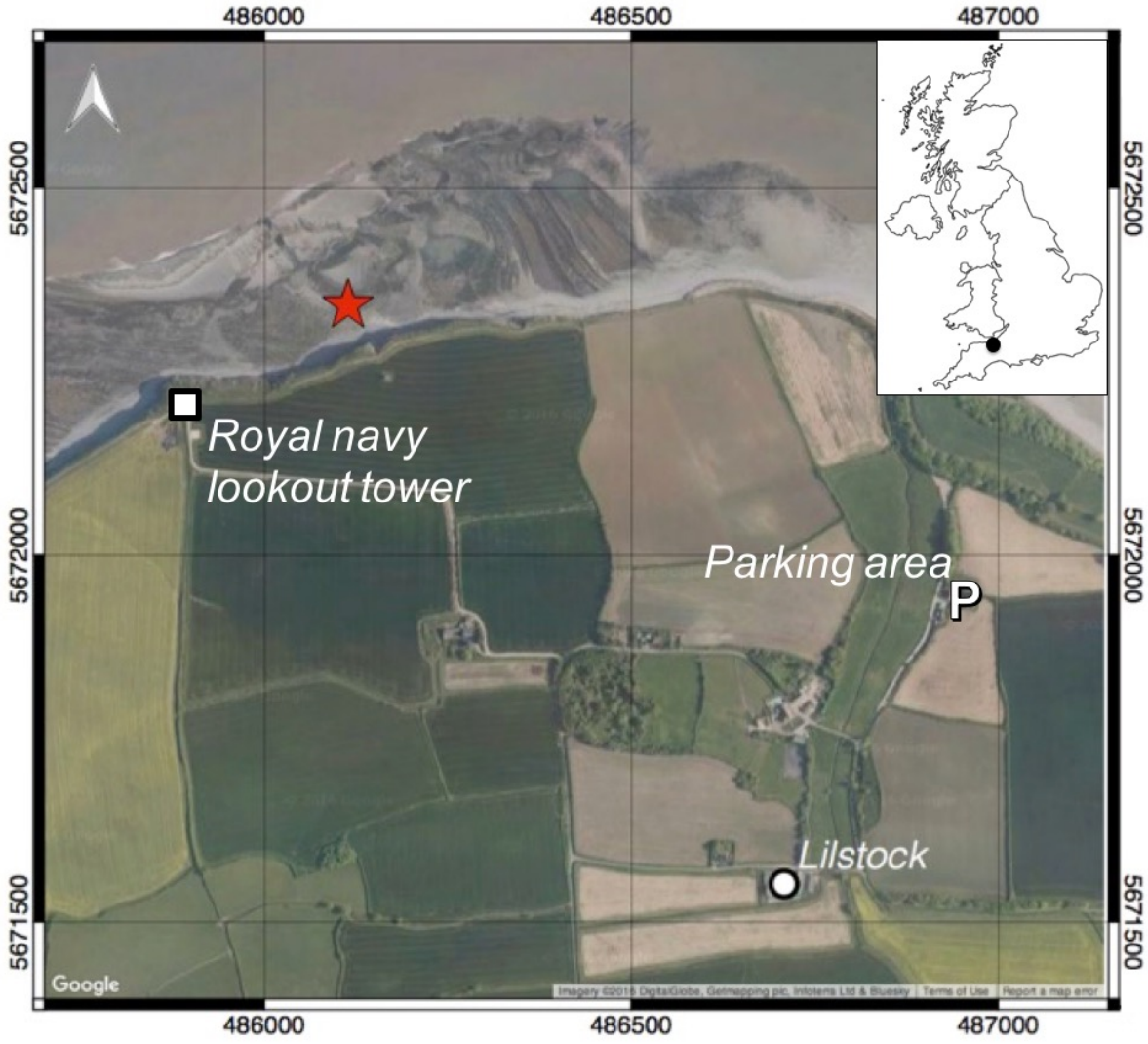

Figure 4.1 Location of the site of the seismic survey (red star) on the coast of Somerset, South West England.

The outcrop is constituted by two 15 cm thick horizontal beds of limestone containing vertical fractures, overlaying a layer of shale. It contains one main set of sub-vertical joints,

broadly striking East-West (Figure 4.2). These joints are consistent with the Alpine joints described by (Belayneh and Cosgrove, 2004), which are located in the hinge region of the Lilstock anticline and are subparallel to the fold axis (See Figure 3 from Engelder and Peacock, 2001). A secondary set of smaller joints, with no defined preferred orientation is also visible (Figure 4.2). They generally do not cross cut the main fractures, and are partially or totally cemented.

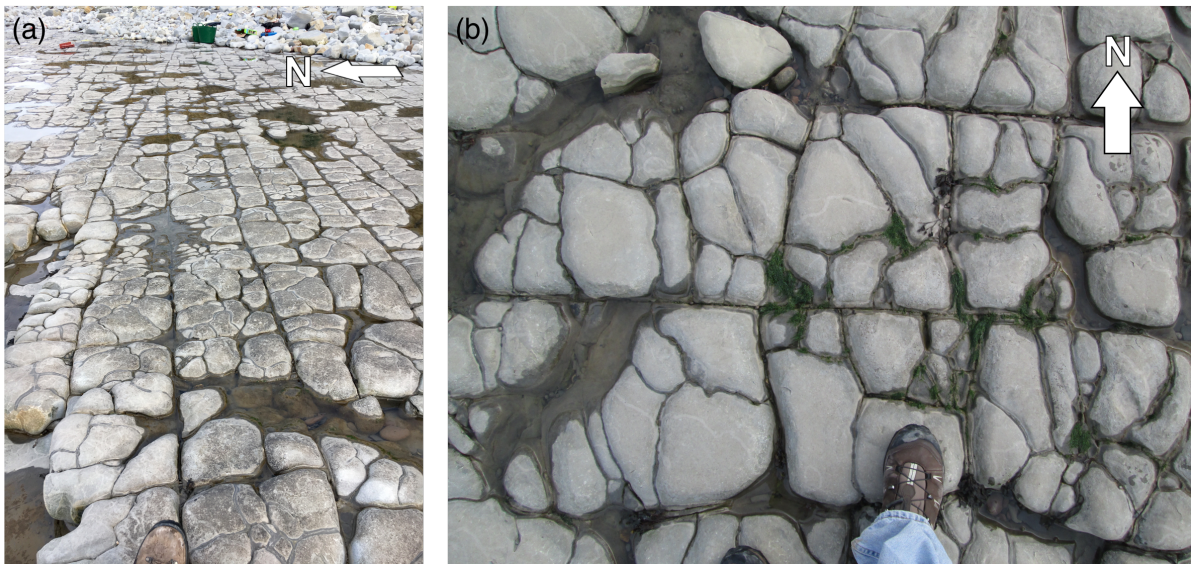

Figure 4.2 Fracture sets outcropping at the Lilstock wave-cut platform. (a) Long fractures striking East-West. (b) Short cracks with no well-defined preferred orientation.

The beach at Lilstock experiences large tides (Figure 4.3). This results in the beach being submerged at high tide, including the outcrop of interest (Figure 4.4). The seismic survey was conducted on 21 September 2016. According to the tide table for the Watchet Harbour marina, located 10 km West of Lilstock, on this day high and low tides occurred at 10:21 and 16:19, respectively.

For the purpose of this chapter, the generic terms 'fractures' and 'cracks' are used to refer to the E-W sets of long joints, and to the intermediate set of short joints, respectively.

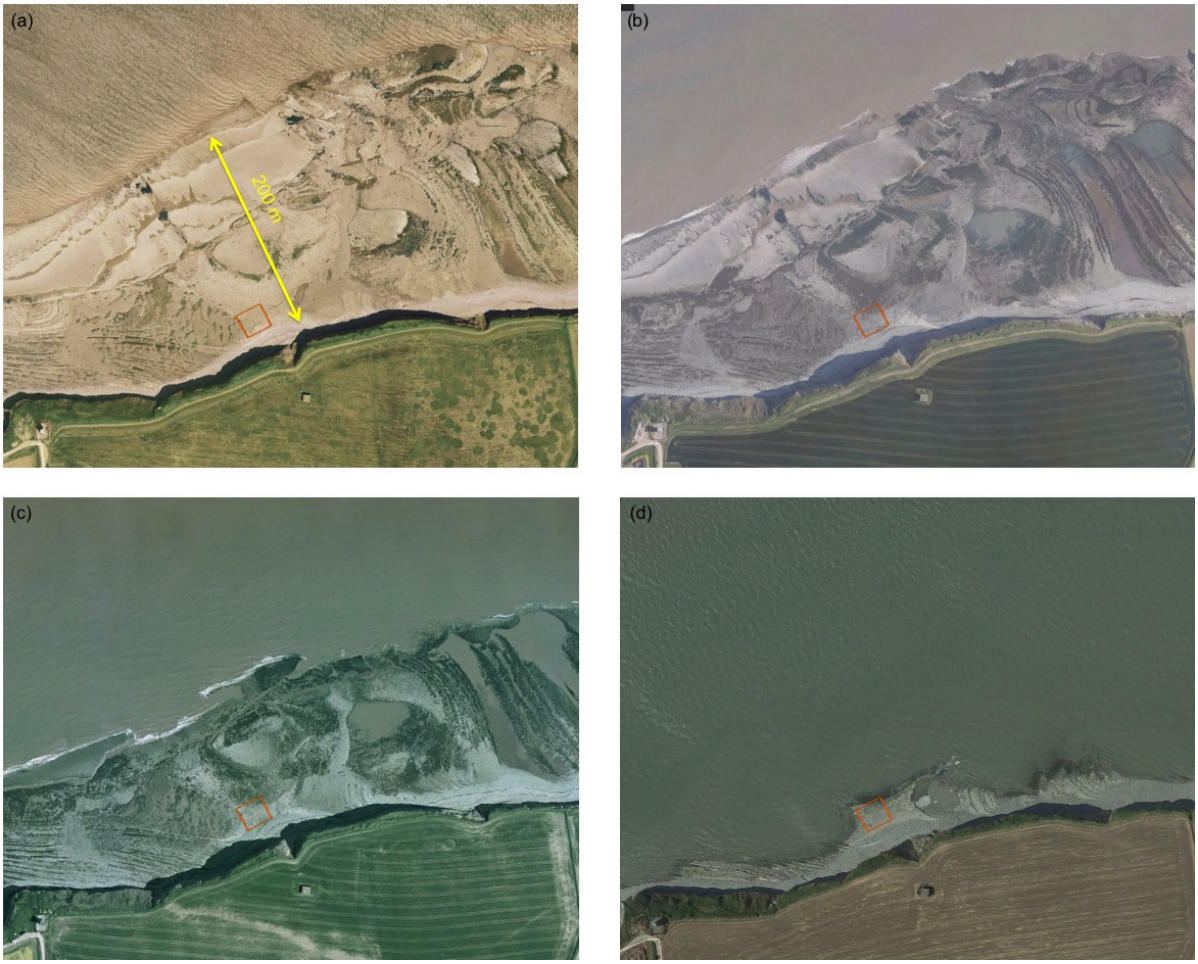

Figure 4.3 Satellite scenes showing the advance of the sea at Lilstock, from (a) low to (d) high tide. Note the boulder area between the location of the seismic experiment (red square) and the cliff, showing the uppermost limit of the tide. Google Earth V7.1.8.3036, (a) 30/06/2006, (b) 31/12/2010, (c) 31/12/2001, (d) 15/08/2016.

4.2.3 Data acquisition

Seismic surveys using compressional (P) and horizontal shear wave (S_H) were carried out on the Lilstock outcrop. The surveys followed the method described by Hobday and Worthington (2012) and adapted by Foord et al. (2015) on the Lilstock beach, but both only used P-waves. A grid of 16 pairs of geophones (4 × 4) was set up on a 15 × 15 m^2 square with a 5 m spacing (Figure 4.5). Each pair is composed of a vertical and an horizontal geophone, recording P- and S-waves, respectively. In order to firmly couple the geophones to the bare rock and maximise

Figure 4.4 Photograph taken at 10:45 on 21 September 2016, showing the high tide at Lilstock beach. Note the presence of boulders at the foot of the cliffs, indicating the uppermost limit of the tide. Photograph courtesy: J.-M. Kendall.

the energy transfer, the usual spikes were removed and replaced with flat bases, which allow to stick them to the ground using Crystalbond^{TM} glue. Horizontal geophones were oriented in the North-South direction, normal to the main fractures. Seismic shots were distributed across 16 locations around the geophone grid, in order to cover the whole range of azimuths (Figure 4.5). While hammer shots were performed directly on the bare rock to generate *P*-waves, *S*-waves were generated using a "Kirk" source (See Figure 4.6 and Appendix A). At every shot location, the source was oriented in the North-South direction, parallel to the horizontal geophones. The seismic traces were recorded using a Geometrics 24-channel Geode seismic recorder, within a sampling rate of 0.10 ms. Vertical and horizontal geophones had a 10 Hz and 4.5 Hz dominant frequency, respectively. The raw travel times were transformed into seismic velocities using manual picking of first arrivals and distances calculated based on the source-geophone grid geometry.

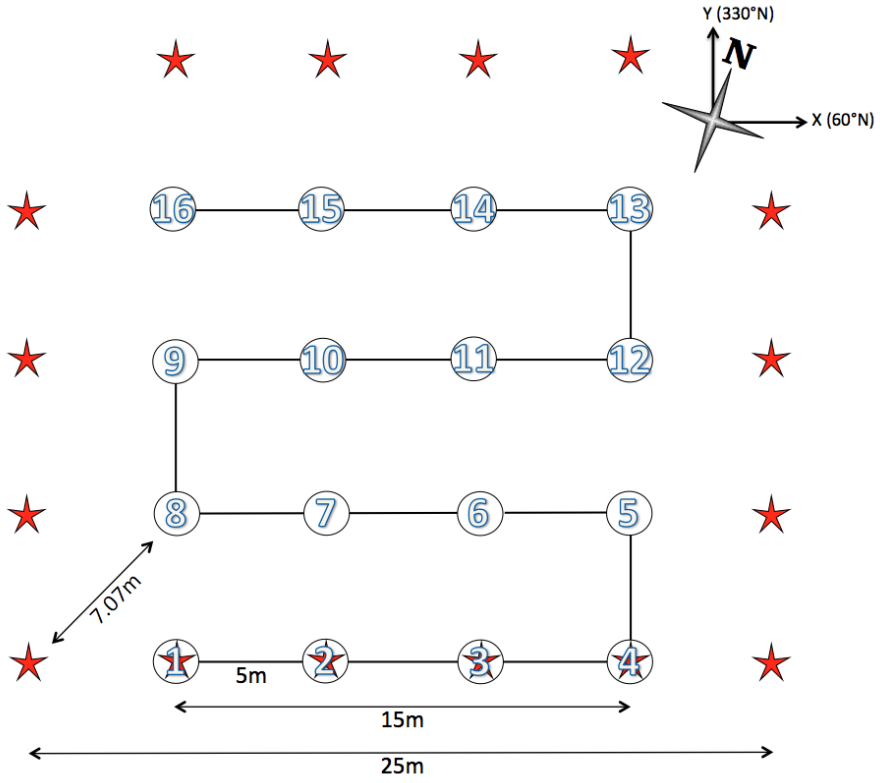

Figure 4.5 Configuration of the seismic surveys at Lilstock. Pairs of vertical and horizontal geophones are represented by numbered circles and hammer source locations by red stars.

The surveys were repeated over time using the same geophone and source locations, in order to investigate the potential effect of the tide on fracture saturation and fracture compliance. Three pairs of P- and S_H-wave surveys were performed after the high tide, at 13:45, 15:10 and 17:25, respectively (Figure 4.7).

Figure 4.8 shows raw traces from the P-wave surveys at Lilstock. These seismograms correspond to the shot at the bottom-left source point on the grid (Figure 4.5) for each of the three surveys. The data show little noise and accurate picking of the first arrivals was greater than 95% of the 256 recorded traces. The unpicked signals mostly correspond to bad connections between the geophone and the digitiser, as seen on the 13^{th} channel in Figure 4.8b. The special case of sources belonging to the same location as geophones #1, #2 , #3 and #4, have been ignored, because of their non-relevancy and dramatic picking up inaccuracy

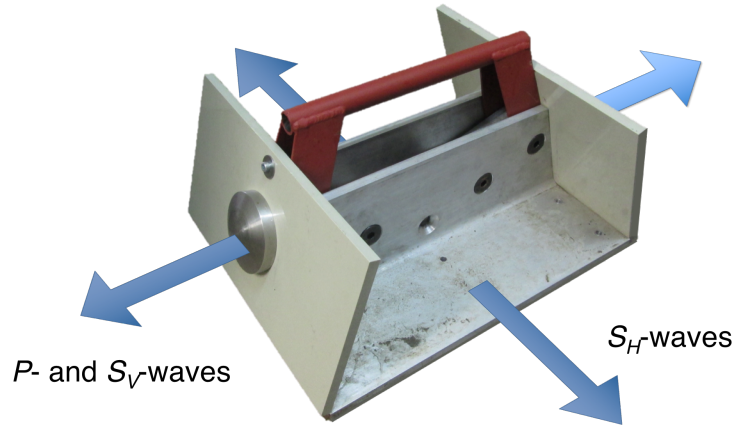

Figure 4.6 Shear-wave source and generated seismic waves by hammering the metal disc.

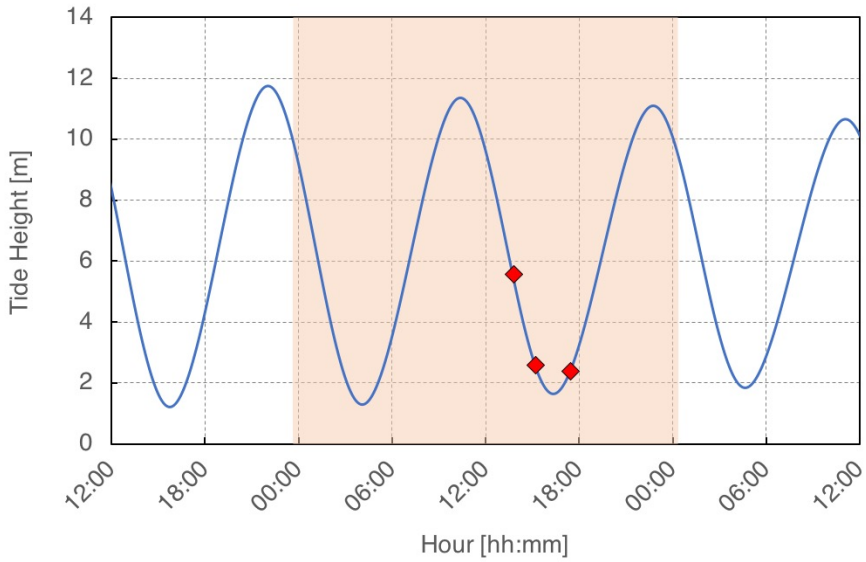

Figure 4.7 Tide predicted for Watchet Marina harbour, located 10 km West from Lilstock, on 21 September 2016 (orange shaded area). The three pairs of surveys are indicated by red diamond markers.

associated to the very short distance of propagation.

Due to the geometry of the grid, not all horizontal geophones recorded pure S_H-waves. To avoid P-S_V conversion, S-waves were only picked when the ray azimuth is between 45 and 135 degrees from North (See Figure 4.6 and Appendix A). Furthermore, the S-wave data were much

noisier. As a consequence, only ~33 % of the S_H-wave first arrivals were picked.

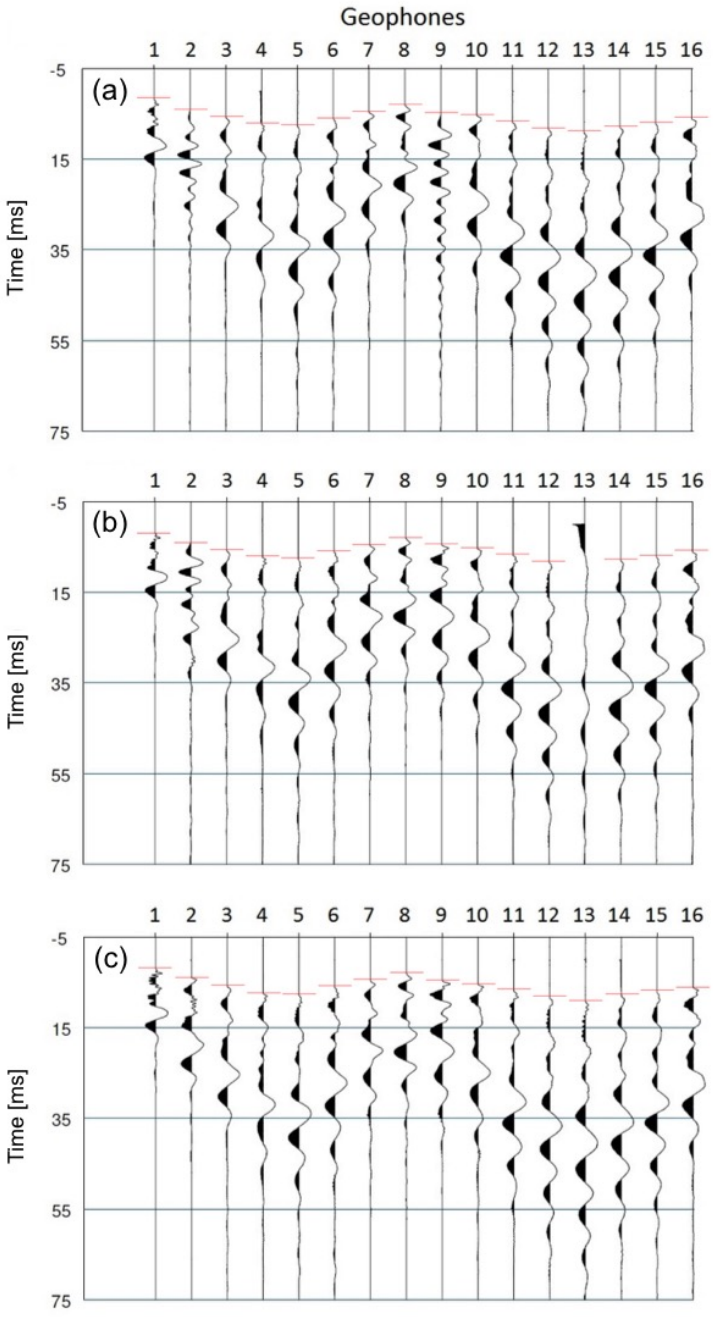

Figure 4.8 Raw traces recorded by the vertical geophones corresponding to the first shot (red star at the bottom left location on Figure 4.5) from surveys at (a) 13:45, (b) 15:10, and (c) 17:25. First arrivals are marked by red scores. Geophones numbers refer to Figure 4.5.

4.3 Results

With the P-wave surveys, raw travel time data were converted into seismic velocities for 24 directions of propagation between 0 and 180 degrees from North. In the case of the S_H-wave surveys, the azimuth coverage drops to a maximum of 12 angles (Figure 4.9a).

Figure 4.9 shows the mean measured seismic velocities as a function of azimuth for each pair of surveys. Error bars were determined by calculating one standard deviation of the measured velocities for each angle of propagation. The P-wave velocities show a maximum around 90 degrees from North. The pattern of the S_H-wave velocities is less clear, mainly due to fewer data and the narrower maximum-minimum range expected for horizontal shear waves (Hall, 2000). Nevertheless, a minimum around 90 degrees from North and maximum near 45 and 135 degrees from North are visible.

To identify the best-fitting model, an inversion is performed for the values of Z_N and Z_T that minimise the RMS misfit between observed and synthetic velocities. The pattern of the measured azimuthal velocities can only be reproduced with a rock physics model composed of a set of aligned fractures oriented East-West, embedded in an isotropic background. The compressional velocity of the rock matrix has been assumed to be equal to the highest measured mean velocity, 2750 m s^{-1}. The background density was calculated using the Gardner's relation (Gardner et al., 1974), giving a value of 2250 kg m^{-3}. The values of fracture compliance related to these models are listed in the table 4.1.

Table 4.1 Best fitting fracture compliance parameters for the three pairs of seismic surveys at Lilstock. Errors estimated by F-test with 90% confidence.

	Survey #1 13:45	Survey #2 15:10	Survey #3 17:25
Z_N/Z_T	0.20 ± 0.08	0.42 ± 0.10	0.46 ± 0.11
Z_N [× 10^{-11} Pa^{-1}]	1.28 ± 0.43	1.44 ± 0.25	1.26 ± 0.23
Z_T [× 10^{-11} Pa^{-1}]	6.38 ± 1.09	3.43 ± 0.56	2.73 ± 0.43

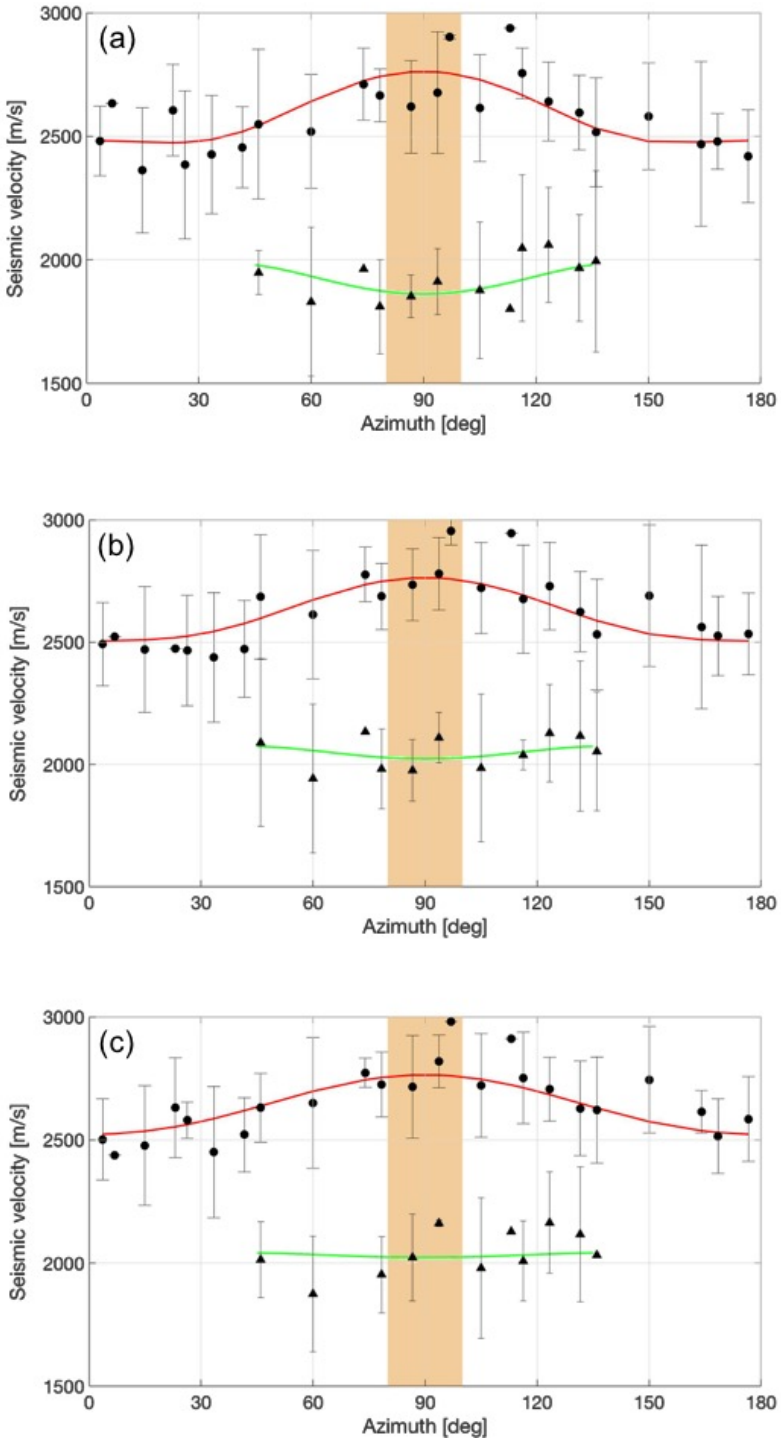

Figure 4.9 Measured P- (black dots) and S_H-wave velocities (black triangles) on the Lilstock outcrop. Surveys realised at (a) 13:45, (b) 15:10, (c) 17:25. Error bars represent one standard deviation of the measured velocities. Red and green curves show the best fitting modelled velocities for P- and S_H-waves, respectively. Orange shaded area represents the range of strikes of the main fracture set.

4.4 Discussion

4.4.1 Seismic velocities versus azimuth

The velocity pattern observed on the field can only be recovered using a rock physics model containing a single set of aligned fractures striking E-W. P-wave velocities show a maximum in the plane parallel to the fracture face and minimum in the normal direction (Hall, 2000; Bamford and Nunn, 1979; Nunn et al., 1983; Crampin et al., 1980; Foord et al., 2015; Hobday and Worthington, 2012; Inks et al., 2015). This model also explains the pattern of the S_H-wave velocities (Hall, 2000). The main fracture set observed in the field is assumed to be the dominant factor influencing the anisotropy. The secondary cracks are randomly oriented and serve to reduce the seismic velocities. In comparison, Foord et al. (2015) recorded P-wave velocities up to 3500 m s^{-1} in a limestone bed located 150 meters northward from the study area. Their results show two fracture sets, orthogonally aligned. A few P-wave propagation angles do not satisfy the best-fit models (6.9°, 96.9° 113.1° North) but these directions contain few data in comparisons with the other azimuths and are considered to be less representative of the overall anisotropy. The model assumes homogeneity in fracture compliance and matrix velocities, while some lateral variation is likely to be expected across the survey area (see Chapter 3). Nevertheless, a model with a single E-W fracture set explains the bulk of the observable velocities.

Such heterogeneity is also responsible for the significant scattering present in the data. Hobday and Worthington (2012) attributed these errors to three major causes, the first one being error in picking the first arrivals. Due to the particularly clear signal, this is assumed to be relatively low. The second cause is due to the likely variation of fracture compliance over the surveyed area. Some variation in crack density and aperture were observed on the grid. The third cause of scatter is lateral variations in the rock matrix velocity. After carrying out the survey at Lilstock, a fourth possible cause of scatter being of geometrical nature was identified. There is a slight variation between the *in-situ* position of the geophones and source points, and the idealised grid (Figure 4.5) used to perform the travel-time to velocity transform. For example, it is very likely that the first hammer shot of each one of the three surveys was

not performed exactly on the same point on the bare rock. Nevertheless, it is assumed that the heterogeneity of the effective medium, such as variation in fracture characteristics (spacing, aperture) and matrix properties (seismic velocities, density), is the dominant source of error.

4.4.2 Velocity changes

Figure 4.10 shows the variation of *P*-wave velocities for each angle of propagation between the first and the third surveys. An increase in velocities of up to 8% is visible between the first and the third surveys (Figure 4.10a). Two of the three angles that show a reduction in velocities correspond to azimuths with few data, while the third one shows a steadier trend, with a velocity change around zero. Most of the variation occurs between the first two surveys (Figure 4.10c).

The velocity increase highlights a change in the properties of the fractured outcrop. This change is attributed to the tide going out during the seismic experiment and the drainage of the fractures. An increase of the seismic velocities as the tide recedes, which is attributed to the lower density air replacing relatively incompressible liquids in the fractures. The fluid substitution at Lilstock impacts more the density than the incompressibility of the rock. The general form of *P*-wave velocity is $v_p = \sqrt{\frac{\kappa+4/3\mu}{\rho}}$, where κ is the bulk modulus and μ is the shear modulus. Replacing liquid (sea water) with gas (air) will not affect nor the incompressibility factor κ and μ, but will reduce ρ, yielding higher velocities.

The increase in velocities is also explained by the fluid substitution theory of Gassmann (1951). Figure 4.11 shows the P-wave velocity as a function of the fluid saturation. P-wave velocities first decrease gradually with increasing fluid saturation, because of the effective density increase. However close to the full saturation Vp increases drastically because the pore fluid compressibility effect outweighs the density effect. The increasing velocities detected at Lilstock is thus assumed to be related to a decrease in fluid saturation of the fracture network.

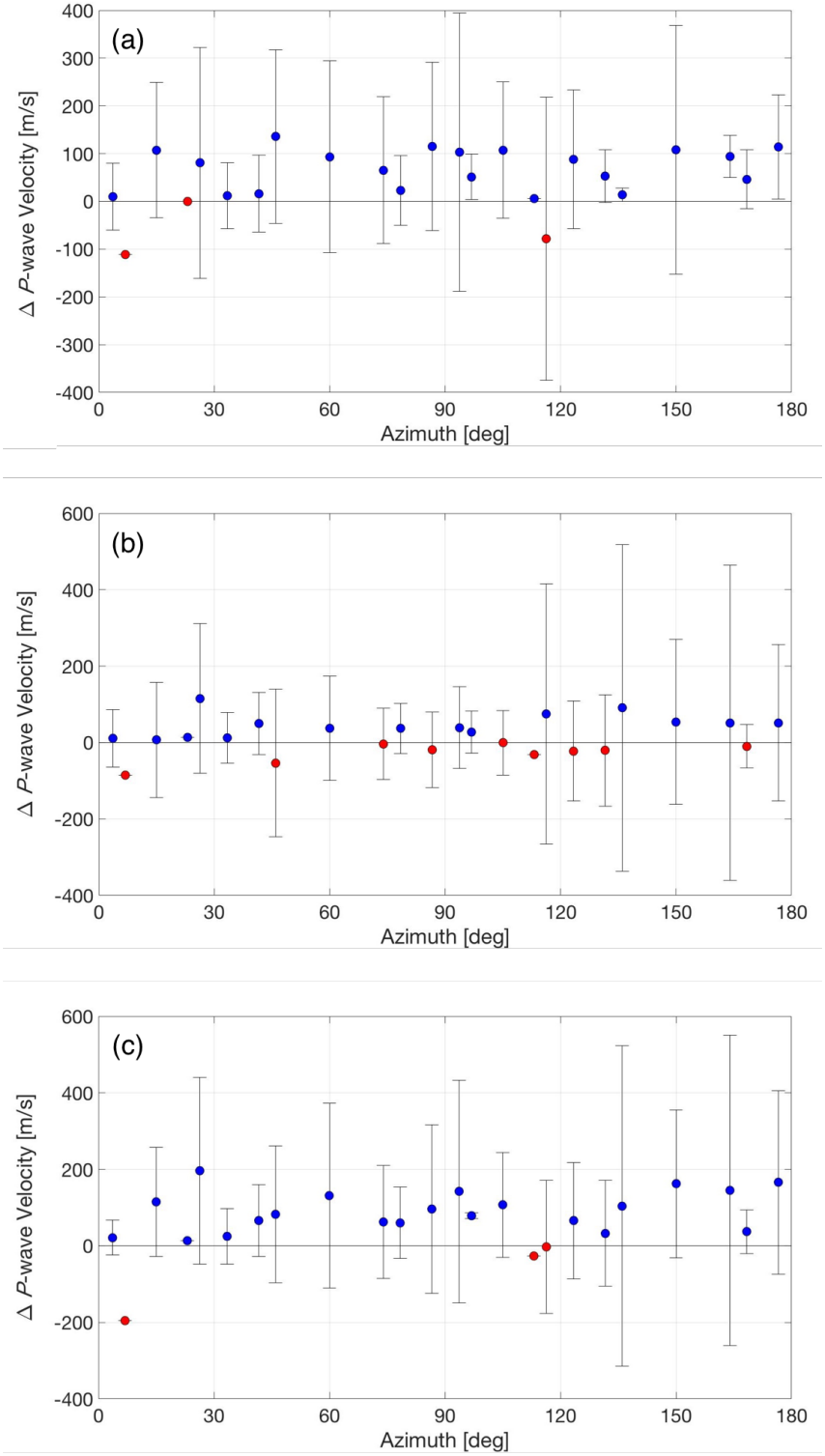

Figure 4.10 *P*-wave velocity variation for each measured angle of propagation between (a) survey #1 (13:45) and survey #2 (15:10), (b) survey #2 (15:10) and survey #3 (17:25), and (c) survey #1 (13:45) and survey #3 (17:25). Blue and red dots show positive and negative values, respectively.

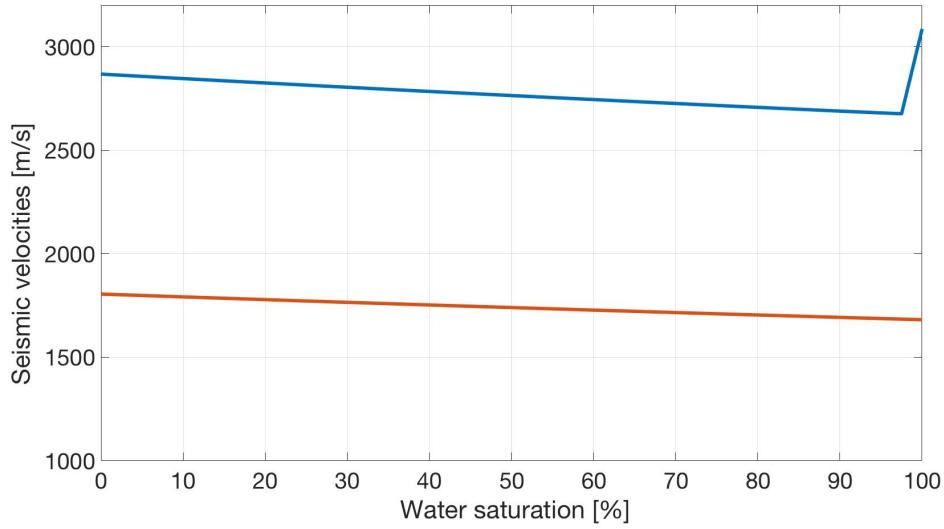

Figure 4.11 *P*-wave velocity as a function of fluid saturation following the fluid substitution theory developed by Gassmann (1951).

4.4.3 Fracture compliance

The values of Z_N/Z_T obtained at Lilstock fit into the typical range of published data (Verdon and Wüstefeld, 2013; Choi et al., 2014; Foord et al., 2015). Fracture compliance results presented in this study evolve from partially saturated to mostly drained conditions, as the tide goes out. This dramatic increase in fracture compliance ratio over time is mostly due to a drop of the shear compliance of 46% between the first and the third survey. Over the same time, the normal component experiences a decrease of around 8%.

This change is explained by the retreat of the tide and the partial draining of the fractures. This can lead to a loss of lubrication due to the water flowing out the fractures, which can contain some natural lubricants, such as algae slime. Most of the rock physics models assumed smooth fracture faces, but in reality, they are likely to present significant roughness and asperities. They often exhibit mineralization, such as bridges between fracture faces (Sayers et al., 2009). Because of the very shallow depth investigated here, changes in hydrostatic pressure is assumed to be not significant, - the fracture aperture is unchanged, and leads to negligible variation in Z_N.

Based on a P-wave survey on the Lilstock beach, Foord et al. (2015) found that $Z_N/Z_T = 0.37 \pm 0.06$ on an outcrop located about a further 150 m North on the wave cut platform, and containing two orthogonal fracture sets. Hobday and Worthington (2012) performed a seismic survey on a fractured wave-cut platform of laminated sandstones on the North coast of Scotland, and found that $Z_N/Z_T < 0.1$. Both studies were performed on locations closer to the sea shore than the present study area and both concluded that water-saturated fractures induced low values of fracture compliance ratio.

Laboratory experiments made on core and synthetic samples have shown that Z_N/Z_T tends to increase with the drainage of fractures with a stiff fluid (Lubbe et al., 2008; Hsu and Schoenberg, 1993; Sayers, 1999; Pyrak-Nolte et al., 1990). But unlike for the results of the present study, this is controlled by an increase of the normal compliance with the removing of the fluid. Also, these experiments were made in closed systems, preventing the fluid to escape the fractures and resulting in high values of normal compliance.

Far et al. (2014) presents similar results to the ones presented here, measuring seismic anisotropy in synthetic fractured medium, with and without rubber inclusions. Smaller Z_N/Z_T results with rubber inclusions induced by a decrease of both Z_N and Z_T, but the tangential component appears to be the most affected.

4.5 Conclusions

Three near-surface seismic surveys were carried out on a fractured wave cut platform located on the coast of Somerset, UK. The surveys were performed over a period when the tide was going out and the fractures were draining. The site exhibits a strong seismic anisotropy caused by the presence of a single dominant set of aligned fractures. An increase of the seismic velocities as the tide recedes, which is attributed to the lower density air replacing relatively incompressible liquids in the fractures. Furthermore, an increase in the fracture compliance ratio (Z_N/Z_T) is observed, mainly due to a dramatic drop of the tangential component (Z_T). These behaviours indicate a change in the elastic properties of the outcrop, attributed to a

decrease in fractures saturation as the tide is going out. The dropping Z_T is attributed to the removal of lubricants. The fractures at Lilstock are filled with clay (Janos Urai, Aachen University, Personal communication), which acts as a lubricant when combined with water (Odom, 1984; Schleicher et al., 2006; Tembe et al., 2010).

Azimuthal seismic surveys using P-waves are useful to determine fracture orientation, as well as changes in fracture saturation. They provide insights into fracture properties at the field scale. Fractured outcrops near the shoreline and influenced by tide cycles provide good sites to develop techniques for fracture imaging. Unlike the laboratory experiments, field surveys are not fully constrained and some assumption have to be made in order to interpret the present results. A good example is the assumption of rock and fracture homogeneity across the field site. Further experiments are needed to tackle these uncertainties. It would be worth expanding the study area to further investigate issues of upscaling. Such relations between fracture length and fracture compliance are of significant importance while upscaling to reservoir settings, where fluid migration is a crucial topic in a range of fields.

CHAPTER 5

Fracture characterisation using shear-wave splitting at Nabro volcano following the 2011 eruption

Abstract

Nabro Volcano, situated in the Afar depression, erupted on 12 June 2011. This first ever recorded eruption was one of the most unexpected large volcanic events of the last decade. About 10 weeks after the start of the eruption, a temporary network of eight three-component seismometers was deployed around the volcano by a team of Eritrean and British researchers. This study is based on a 4-month dataset containing events manually located below the caldera. High b-values were calculated, suggesting the presence of a dense fracture network with fluid content. Shear-wave splitting (SWS) measurements highlight an overall trend of the fast polarisation, ϕ, in the NW-SE direction, parallel to the regional maximum stress component. A shift of ϕ from an E-W to the NW-SE is observed over time. These results are attributed to the presence of two sets of fractures, one being activated by the eruption. Delay time between the fast of the slow shear waves, δt, shows that the anisotropy is localised in the first three kilometres below the surface. By inverting seismic anisotropy, variations of fracture

compliance ratio are also observed. In particular, Z_N/Z_T of the eruption-related fracture set decreases as a function of time. This is attributed to the fracture set closing and getting less connected as the fluid pressure is reduced in the hydrothermal system. Nabro Volcano is a promising geothermal reservoir in Eritrea, and fracture characterisation provides a means to help investigate such potential.

5.1 Introduction

Nabro volcano ($13°22'25.93''$N, $41°42'4.97''$W) is situated in the Northern part of the Afar triangle, in Eritrea (Figure 5.1). The volcano experienced its first recorded eruption on 12 June 2011, being one of the biggest unexpected volcanic events in recent years. Nabro is a stratovolcano part of the Bidu Volcanic Complex, which consists in two calderas, Nabro itself and Mallahle, on both sides of the international border between Eritrea and Ethiopia, respectively. This volcanic complex is itself the main element of the Nabro Volcanic Range (NVR), which lines up NNE-SSW, cross-cutting the Danakil micro-plate (Wiart and Oppenheimer, 2005). Nabro volcano is the main feature of the NVR, reaching 2280 m a.s.l. and exhibiting an 8 km diameter caldera. Nabro is located on the western margin of the Danakil block, which is in advanced stages of continental rifting. Danakil is located in the north of the Afar triple junction and is surrounded by the Arabia, Nubia and Somalia plates and lies between the Gulf of Aden, the main Ethiopian rift, and the Red Sea (Figure 5.1).

The eruption of Nabro emitted the largest amount of aerosol into the stratosphere since Mount Pinatubo in 1991 (Fromm et al., 2014). The SO_2 initial volume was estimated to be above 4 Tg during the 15 days following the eruption (Theys et al., 2013), based on observations of sulphate aerosol forming volcanic clouds (Pinto et al., 1989; Zhao et al., 1995). Such large volcanic aerosol clouds have the potential to impact climate at a global scale, including surface temperature and atmospheric circulation, by disturbing the Earth's radiation balance (Robock, 2000). Aerosol emissions from Nabro eruption reached the upper troposphere and the lowermost stratosphere (Clarisse et al., 2014; Friberg et al., 2015; Noh et al., 2017; Liu et al., 2019), spread

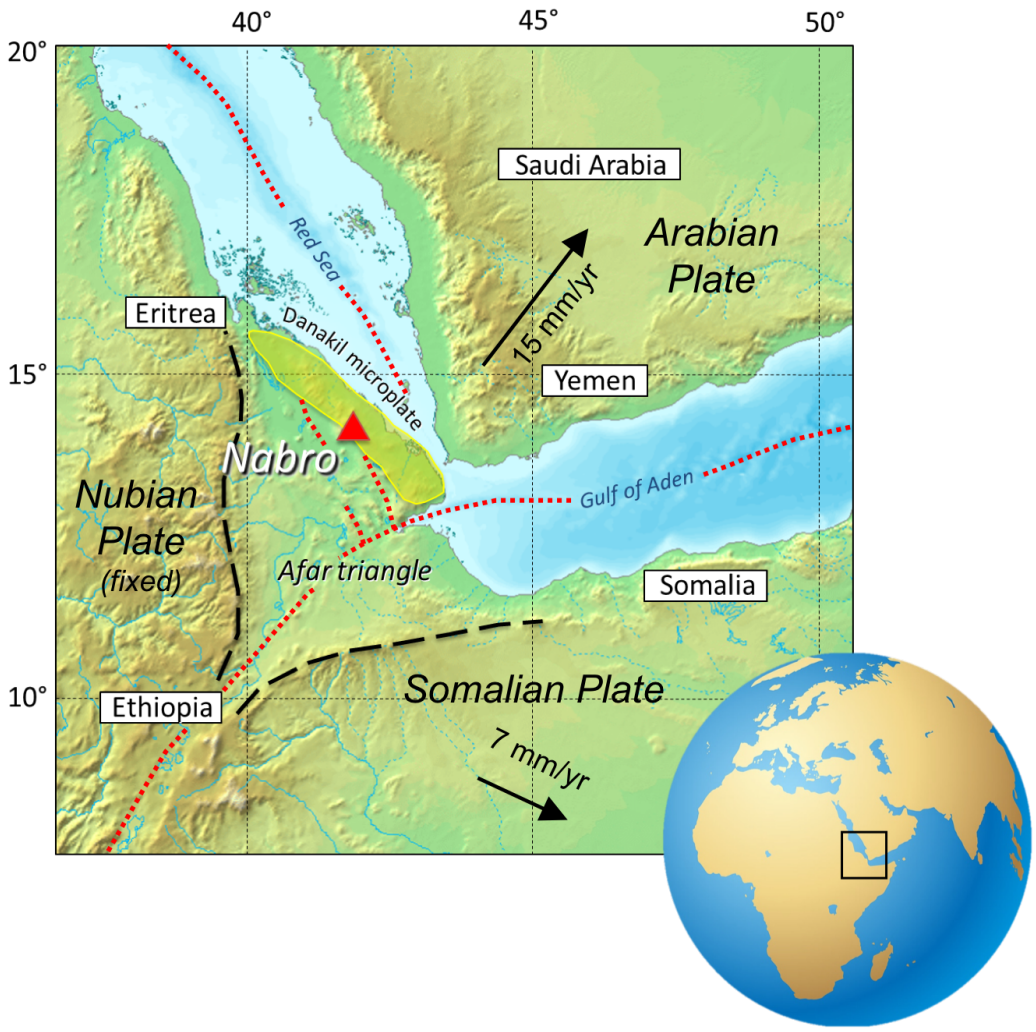

Figure 5.1 The Afar triangle (delimited by the black dashed lines), in the North of the East African Rift (insert). Nabro volcano (red triangle) is located on the western edge of the Danakil block (yellow shaded polygon). Black arrows show the rate and direction of rifting of the tectonic plates around the triple junction. Dotted red lines show the plate boundaries.

to Eastern Europe (Mateshvili et al., 2013) and Asia (Uchino et al., 2012; Shin et al., 2015; Noh et al., 2017), circled the globe northern hemisphere (Liu et al., 2019; Sawamura et al., 2012), and caused small but non-negligible climate variability (Bourassa et al., 2012; Santer et al., 2015).

Nabro eruption produced a powerful infrasound impulse detected in Djibouti and Kenya (Fee et al., 2013), consistent with volcanic emissions of the next days (Goitom et al., 2015).

Nabro eruption, among others, highlighted the potential of induced infrasound observations for monitoring volcanic hazards (Matoza and Fee, 2018).

The eruption caused 7 fatalities, many injuries, and forced thousands of people to move away from the affected zone (Goitom et al., 2015). Material damages, mainly caused by the induced earthquakes and the ash deposits, were also reported in the area.

The eruption lasted for few weeks, as highlighted by the observations of the lava flow heading West and an ash plume up to 5.5 km high, respectively observed by the NASA Earth Observatory on 29 June 2011, and by the Volcanic Ash Advisory Centres (VAAC) of Toulouse on 16 July 2011 (Global Volcanism Program, 2011). High resolution infrared images and radiance measurements also show active vents at least until mid-July (Goitom et al., 2015). Prior to the eruption, a 4.8 M_L earthquake was detected on 31 March 2011, being the first event ever reported by the United States Geological Survey (USGS) for the area. Initially located 25 km southeast of Nabro volcano by the USGS, the epicentre was relocated within the Nabro caldera using field observations, eyewitnesses (Ogubazghi and Goitom, 2014) and regional seismic stations in Ethiopia and Djibouti (Goitom et al., 2015).

Seismic anisotropy is here investigated below the Nabro volcano using shear-wave splitting (SWS) data from a period of 4 months following the June 2011 eruption. During the last decades, SWS has been used to study a range of geological reservoirs, including volcanic settings (Nowacki et al., 2018; Johnson and Poland, 2013; Gerst and Savage, 2004; Baird et al., 2015). Like other geothermal reservoirs associated with volcanic systems (e.g., Tang et al., 2015; Rial et al., 2005; Wilks et al., 2017), Nabro volcano is thought to be one the most promising geothermal sites in the region. This is mainly based on surface manifestations of high temperatures (Figure 5.2 ; Yohannes, 2009, 2012, 2013, 2015). Nabro is also listed by the United Nations (UN) Environment Africa Geothermal Inventory Database (see http://agid.theargeo.org/newagid/site/index.html) as a potential site of geothermal resource in Eritrea.

SWS is arguably the most robust tool to measure and describe anisotropy, which in turn,

gives insight into the nature of the reservoir. SWS can be used to characterise fracture networks (Erten et al., 2001; Baird et al., 2015; Nowacki et al., 2018; among others), as they represent a major pathway for fluid flow in hydrothermal settings (Crampin, 1985). Continuous or repeated seismic monitoring also provides a way to detect temporal changes in the anisotropy and reservoir characteristics and better understand the reservoir properties and elastic behaviour (Gerst and Savage, 2004; Miller, 2002; Verdon and Wüstefeld, 2013; Baird et al., 2015; Teanby et al., 2004a).

Figure 5.2 Photograph of fumarole activity taken few days after the June 2011 eruption (source: Yohannes, 2012). Note the basaltic lava in the background.

5.2 Methodology

5.2.1 Shear-wave splitting

Aligned sets of fractures are a common cause of seismic anisotropy, which can be investigate though measurements of shear-wave splitting. An anisotropic medium causes a shear wave to split into two independent quasi shear waves. The two resulting shear waves are orthogonally polarised and have distinct velocities. The fast shear wave polarisation, ϕ, provides information about the symmetry of the anisotropy. In the case of the presence of one set of aligned fractures, ϕ approximates the strike orientation of these fractures. More complexity is introduced with two or more sets of fractures influencing the local anisotropy (Nowacki et al., 2018; Teanby et al., 2004a). Bias can also be introduced if others sources of anisotropy are present, such as horizontal sedimentary layering. To minimise the effect induced by non-vertical fracture anisotropy, a shear window containing only incident angles between 0 and 45 degrees from vertical up is used. This also avoids the effects of free surface coupling (Booth and Crampin, 1985). These sub-vertical arrivals are easiest to analyse in terms of vertically aligned fracture sets (Verdon et al., 2011). The delay time between the fast and the slow *S*-waves, δt, is a measure of the strength of the anisotropy and can be related to the fracture density.

In this work SWS measurements are performed using the splitting correction method introduced by Silver and Chan (1991). The method rotates and shifts the horizontal components to remove the effects of the anisotropy. An analysis window is selected around the shear phase and a grid search is used to find ϕ and δt that best remove the effects of the splitting in this window. In the presence of anisotropy, the particle motion within this selected window is elliptical. This is linearised after correction for anisotropy. The best splitting parameters (ϕ and δt) are those that minimise the second eigenvalue of the particle-motion covariance matrix. Finally, errors can be assessed using an F-test is used to compute the 95% confidence interval for the best values for the parameters ϕ and δt.

This technique can give results that are highly dependent of the selection of the start and end of the time window, introducing significant uncertainties on the results. Manually testing

different windows for each SWS measurement is time consuming and not suitable for large earthquake catalogues. The analysis is hence extended by using the automated multiple windows approach developed by Teanby et al. (2004b). This technique uses a range of windows with distinct start and end times (Figure 5.3). A series of N windows are defined around the shear phase arrival. The beginning of these windows varies between T_{beg_0} and T_{beg_1}, with N_{beg} steps of ΔT_{beg}. Similarly, the end of the sampling windows varies between T_{end_0} and T_{end_1}, with N_{end} steps of ΔT_{end}. The total number of analysis windows is therefore given as

$$N = N_{beg} * N_{end}. \tag{5.1}$$

Here 5 time interval steps are used for both N_{beg} and N_{end} when applying the multiple windows approach. SWS is estimated for a total of $N = 25$ windows per ray.

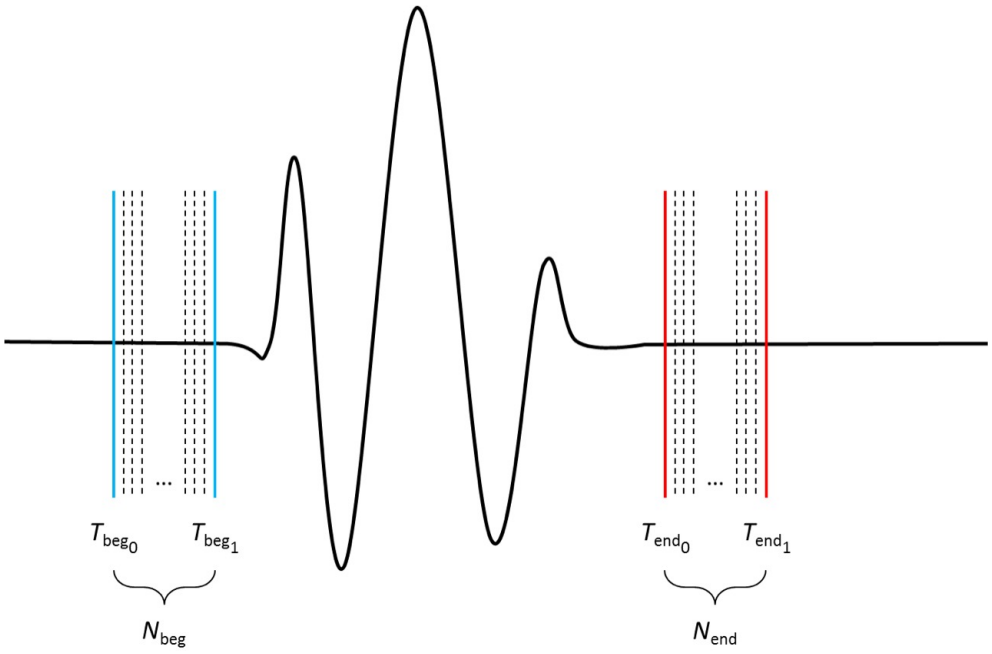

Figure 5.3 SWS using multiple evaluation windows. Start (blue) and end times (red) define a series of windows around the shear phase (black wavelet).

SWS parameters are calculated for each window. A cluster analysis is then used to identify the measurements that are stable (steady ϕ and δt parameters) over many windows, highlighting the robustness of these measurements. Reliable clusters must contain a minimum number of stable measurements and show small error bars. The best solution corresponds to the window which gives the SWS estimates with the smallest uncertainties within a stable cluster.

In order to assess the automated SWS, each measurement is displayed on a diagnostic plot (Figure 5.4). Several criterions of confidence are to be taken in account to validate the reliability of the SWS measurements (Teanby et al., 2004a; Schlaphorst et al., 2017): (1) clear *S*-phase in the recorded data, (2) energy minimisation of the corrected transverse component, (3) linearisation of the particle motion in the analysis window after correction, (4) stable cluster over a large range of time windows, (5) similar fast and slow wavelets, (6) clear unique minimum in the error contour plot.

Based on the observation of these criteria, 200 source-receiver records were considered as reliable SWS measurements and used in the analysis of the Nabro volcano anisotropy.

5.2.2 Magnitude-frequency distribution and *b*-values

The frequency of earthquakes as a function of the magnitude can help infer the state of stress of a region at a given time period. The most broadly used approach to quantify the magnitude-frequency distribution of an earthquake population is the Gutenberg-Richter relationship (Gutenberg and Richter, 1942), which is expressed as,

$$N(M) = 10^{(a-bM)}, \tag{5.2}$$

or

$$log_{10}N = a - bM, \tag{5.3}$$

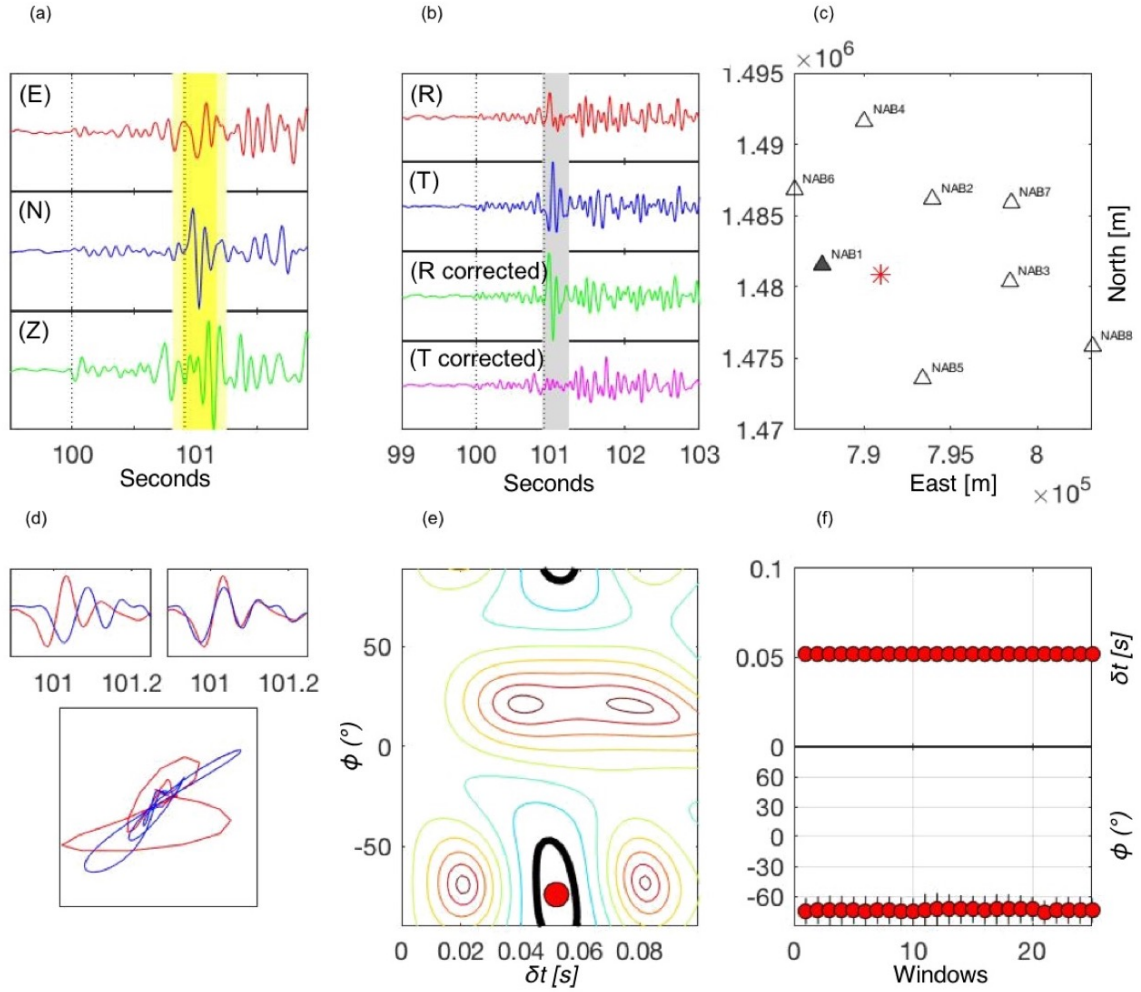

Figure 5.4 Example of splitting measured at station NAB1 on a magnitude 1.1 M_L event recorded on 27-08-2011. This event was originated at 3.68 km below the surface. The incidence angle of the arrival is 45 degrees from vertical up. (a) Filtered (bandpass 1 to 15 Hz) east-west (E), north-south (N), and vertical (Z) components. Dotted bars show the manually picked *P*- and *S*-phases (Goitom, 2017). Yellow shade delimits the range on which the time windows were chosen. (b) Uncorrected and corrected radial (R), and transverse (T) components. Radial refers to the original polarisation of the *S*-wave in the isotropic medium and transverse is the component tangential to this. Note the effective minimisation of the energy on the transverse component after the splitting correction. Grey shade delimits the best result window. (c) Map of the seismic array (triangles) and the location of the event (asterisk). The station which recorded the signal is highlighted by the black shaded triangle. (d) Top 2 panels: Fast (red) and slow (blue) shear waves before (left) and after (right) the splitting correction. Bottom panel: Particle motion before (red) and after (blue) the splitting correction. Note the good linearisation of the initially elliptical-shaped particle motion. (e) Surface error plot of the grid search over fast orientation (ϕ) and delay time (δt). The solid black line shows the 95% confidence interval around the best splitting parameters. (f) Cluster of the best fitting solution for 25 analysis windows. A reliable result is stable and shows a plateau over several time windows, both in ϕ and δt.

where N is the number of events with a magnitude equal to or higher than M, and a and b are constants representing the intercept and the slope of a straight line, respectively.

First, a Goodness-of-Fit Test (Wiemer and Wyss, 2000) is used with a 95% probability to compute the required magnitude of completeness, M_C, which is defined as the magnitude above which all events of the earthquake catalogue are recorded (Rydelek and Sacks, 1989; Mignan and Woessner, 2012). On a logarithmic plot (Figure 5.5), below M_C, the cumulative number of events starts to bend and shows a plateau. This is because the smaller events are more difficult to detect.

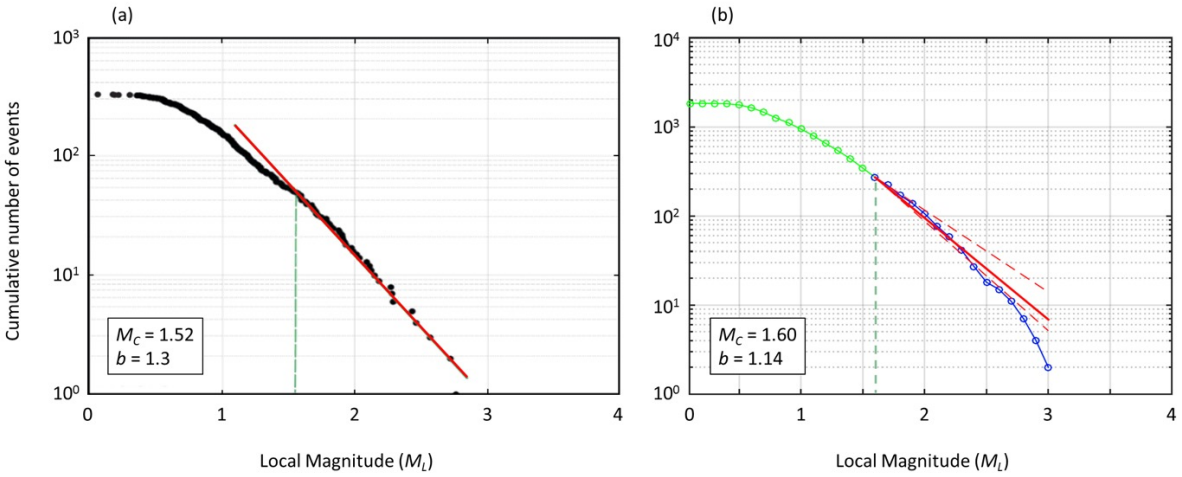

Figure 5.5 Frequency-magnitude relationships at Nabro for (a) the period 31 August to 7 October 2011 (modified from Hamlyn et al., 2014) and (b) the period 31 August to 31 December 2011 (modified from Goitom, 2017). Smooth red lines are the best fits and green dashed lines are the magnitudes of completeness.

The parameter b (commonly called b-value) describes the gradient of the straight line fitting the data above M_C on a logarithmic scale plot (Figure 5.5). The maximum likelihood method (Mignan and Woessner, 2012; Aki, 1965) is used to determine the b-value. The b-value is a measure of the relative proportion of low to high magnitude earthquakes and provides insights into the rock properties and the state of stress of the region (Scholz, 2015). b-values

are commonly close to 1 in tectonic settings (Frohlich, 1993). In contrast, *b*-values higher than 1 describe regions with low rate of high magnitude events, generally indicating more fractured rock, rich in fluid fill (Ibáñez et al., 2012; Murru et al., 1999). Such high *b*-values, as previously observed at Nabro (Figure 5.5), are typical of unrested volcanic settings (Roberts et al., 2015; Wilks et al., 2017; Murru et al., 1999; Ibáñez et al., 2012). Anomalous *b*-values lower than 1 have been observed. Although low *b*-values are generally encountered in tectonic regimes (Jafari, 2008; Nowroozi and Ahmadi, 1986), they have been observed in volcanic settings (Maher and Kendall, 2018; Jay et al., 2012). In such environment, low *b*-values are attributed to a stiff and closed crustal system, with high stress (Maher and Kendall, 2018; Goitom, 2017).

5.2.3 Seismic dataset

In August 2011, a seismic array was deployed around the Nabro Volcano (Figure 5.6) as an emergency response to the unexpected June 2011 eruption. This local array consisted in 8 three-component broadband seismometers (Table 5.1) provided by SEIS-UK (Brisbourne, 2012) and installed on Nabro's flanks, outside the caldera. Although NAB6 station was flooded early on and the GPS of NAB7 was not working properly, the array ran for 14 months with high signal-to-noise ratio (Hammond et al., 2014) and recorded a total of 18,095 events around Nabro and Mallahle volcanoes (Goitom, 2017).

In this work, the events located manually and reviewed by Goitom (2017) are used. The horizontal and vertical errors are $\leqslant$ 2 km and $\leqslant$ 5 km, respectively. The data cloud was then cropped laterally between 13.33 and 13.40 degrees North and 41.66 and 41.72 degrees East to focus on events beneath the Nabro caldera. This is the main swarm of events where the hydrothermal system is likely to be located. This is also a region of high *b*-values, in comparison with the neighbouring Mallahle Volcano (Hamlyn et al., 2014; Goitom, 2017). In addition, only events shallower than 7 km depth are considered. This lower limit was chosen as this is the inferred depth of the magma reservoir, modelled as a Mogi source by analysing radar satellite data (Hamlyn et al., 2014, 2018; Goitom et al., 2015). The brittle-ductile transition zone was also estimated around 7 km depth by analysing petrological data from post 2011 eruption

Table 5.1 Details of eight stations deployed in August 2011 around Nabro volcano. Note the reduction of the sampling frequency after the October 2011 servicing campaign (modified from Goitom, 2017).

Station name	Sensor	Sensor ID	Latitude [°N]	Longitude [°E]	Elavation [m a.s.l.]	Start date	End date	Sample rate [Hz]
NAB1	6T	T6071	13.3873	41.6554	1329	24/08/2011	09/10/2011	100
NAB1	6T	T6071	13.3873	41.6554	1329	09/10/2011	06/10/2012	50
NAB2	6T	T6014	13.4285	41.7146	1207	26/08/2011	10/10/2011	100
NAB2	6T	T6014	13.4285	41.7146	1207	10/10/2011	07/10/2012	50
NAB3	6T	T6035	13.3759	41.7549	1283	27/08/2011	11/10/2011	100
NAB3	6T	T6035	13.3759	41.7549	1283	11/10/2011	08/10/2012	50
NAB4	6T	N/A	13.4786	41.6786	703	23/08/2011	10/10/2011	100
NAB4	6T	N/A	13.4786	41.6786	703	10/10/2011	07/10/2012	50
NAB5	40T	T4A90	13.3151	41.7082	1272	28/08/2011	14/10/2011	100
NAB5	40T	T4A90	13.3151	41.7082	1272	14/10/2011	09/10/2012	50
NAB6	40T	T4A96	13.4352	41.6410	965	22/08/2011	30/08/2011	100
NAB7	6T	T6216	13.4256	41.7562	893	25/08/2011	11/10/2011	100
NAB7	6T	T6216	13.4256	41.7562	893	11/10/2011	01/10/2012	50
NAB8	40T	T4A85	13.3348	41.7983	655	29/08/2011	13/10/2011	100
NAB8	40T	T4A85	13.3348	41.7983	655	13/10/2011	12/10/2012	50

tephra deposits (Donovan et al., 2018). The final dataset contains 1427 events covering the period from 27 August 2011 to 31 December 2011.

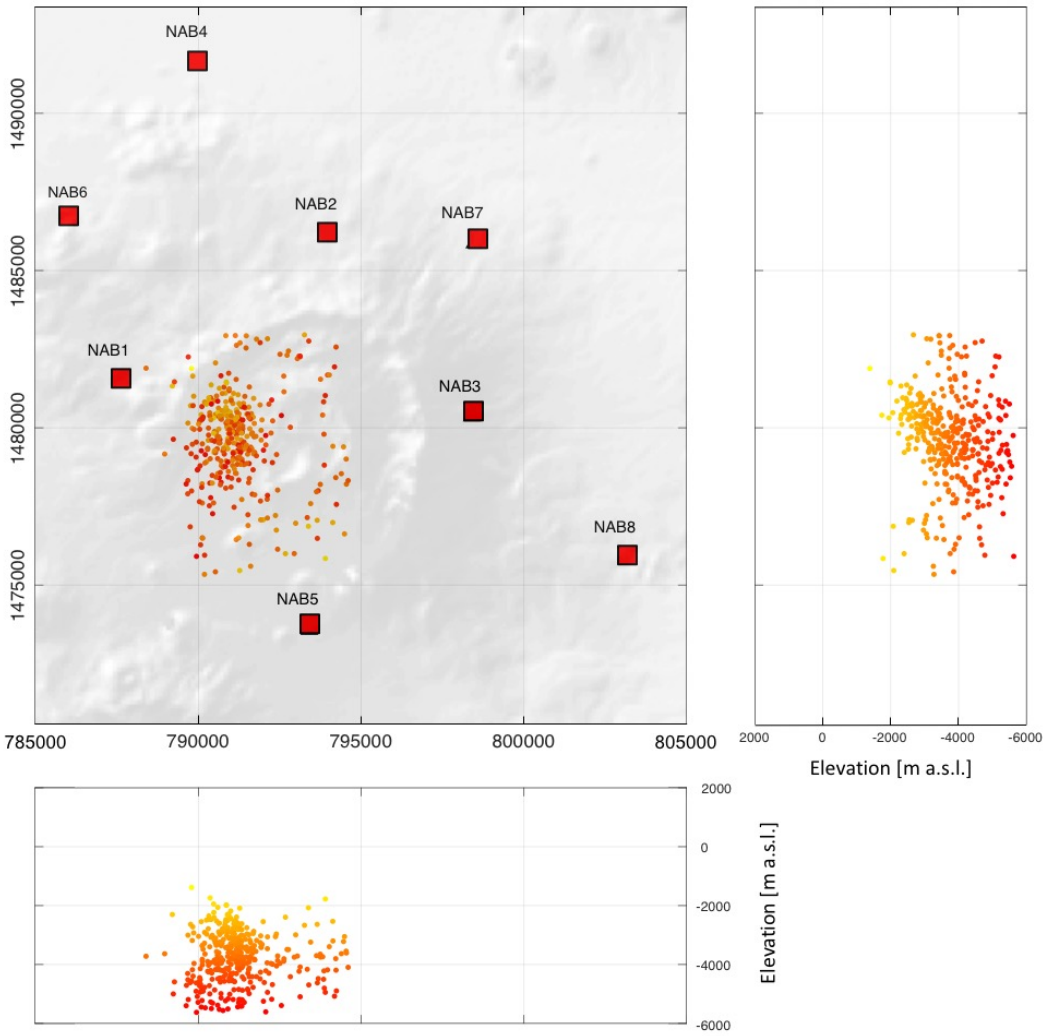

Figure 5.6 Seismic stations around Nabro (red squares) and manually located earthquakes (dots) with raypaths within the shear wave window (incidence angle between 0 and 45 degrees from vertical). Bottom and right panels show the events as a function of altitude (in meters above sea level).

5.3 Results

5.3.1 Depth extent of anisotropy

The splitting parameter, δt, provides an estimate of the strength of anisotropy between the earthquake and the station. Individual results give an average for the raypath variations in

the anisotropy. However, datasets covering a broad range of depths indicate the dependence of anisotropy with travelled distance (Liu et al., 1997, 2008; Thomas and Kendall, 2002; Cochran et al., 2003; Nowacki et al., 2018). The Nabro dataset is composed of events ranged from the near surface to 7 km deep.

In order to evaluate the strength of the anisotropy the amount of splitting is normalised by the distance (D) that the wave travelled between the source and the station:

$$SWA = \left(\frac{\delta t}{D} v_s\right) * 100, \tag{5.4}$$

where SWA is the shear wave anisotropy (in per cent), v_s is the mean shear wave velocity (Maher and Kendall, 2018). Raypath is assumed straight between the source and the station (i.e., constant velocity). This straight-line approximation can lead to significant under-estimations for deep events, but considered as a reliable approximation for shallow earthquakes, where the bending of the ray is minor (Nowacki et al., 2018). Mean velocities (v_s) were extracted from a 1-dimension velocity model of the Afar region (Keir et al., 2009) and previously used for location seismic events at Nabro (Goitom et al., 2015; Hamlyn et al., 2014).

The δt results vary between 0.01 and 0.10 s and the average is 0.05 ± 0.01 s. No trends of δt are discernible, either with depth (Figure 5.7a) or with distance from the source to the station (Figure 5.7b). SWA ranges between 0 and 5% (Figure 5.7c and Figure 5.7d), which is common for fracture-induced anisotropy in the shallow crust (Crampin, 1987; Liu et al., 1997; Nowacki et al., 2018; Baird et al., 2015; Maher and Kendall, 2018). There is a lack of shallow (< 1.5 km) and deep (> 6 km) events. SWS shows a slight decrease with either depth or source-station distance.

No trends in δt and a decrease of SWA with either distance or depth indicates that the source of anisotropy is mainly located in the uppermost layers of the crust (approximately in the first 3 km). In the case of a homogeneous distribution of anisotropy with depth, SWA would

be constant and show no trend with distance (Liu et al., 1997; Thomas and Kendall, 2002), while δt would increase monotonously with depth. The results are in agreements with results from other volcanoes (e.g. Nowacki et al., 2018; Maher and Kendall, 2018; Baird et al., 2015).

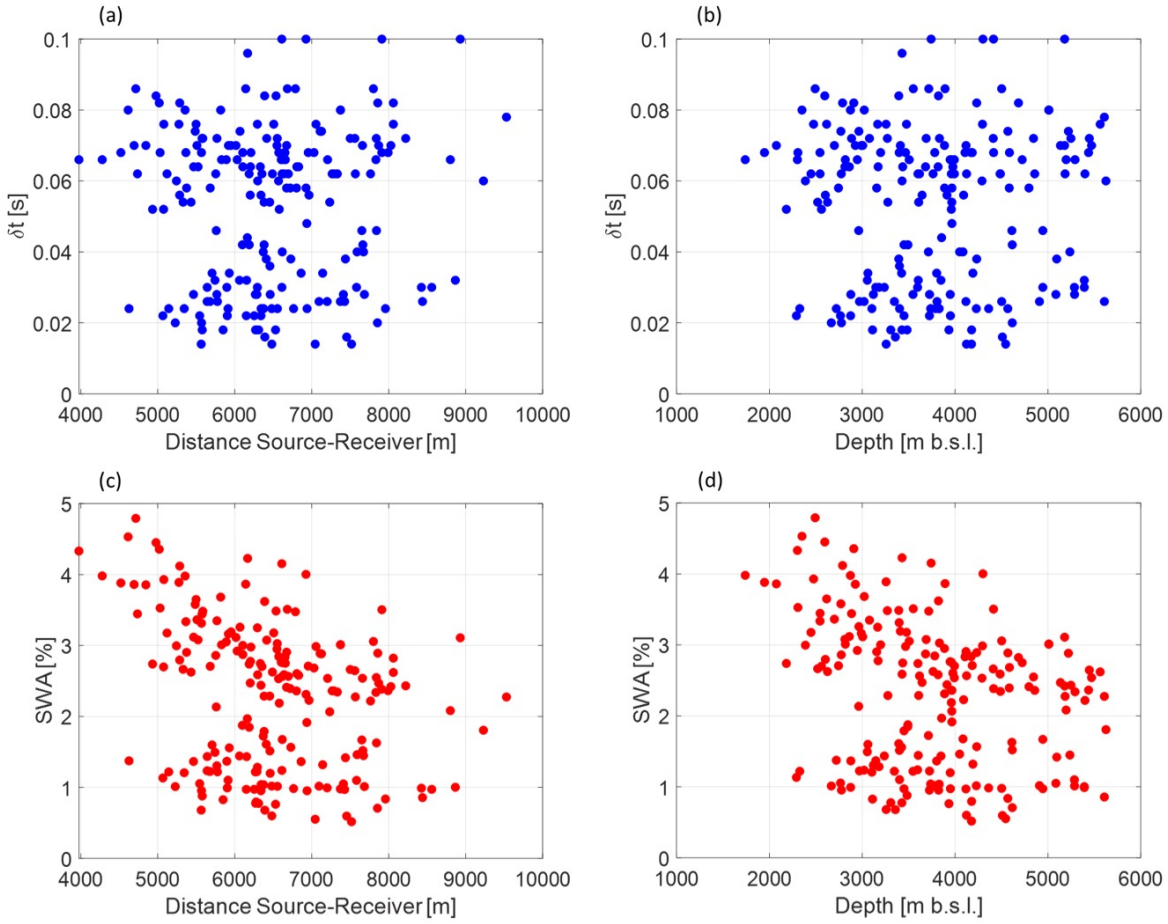

Figure 5.7 Measured amount of splitting for the dataset. (a) Delay time (δt) versus depth, (b) δt versus source-station distance (assuming straight-line raypath), (c) shear wave anisotropy (SWA) versus depth, and (d) SWA versus source-station distance.

There appears to be a bimodal population in δt and SWS, which does not correlate with time. This might reflect variations in terms of stress over wavelength scales.

Finally, no trend with distance to the centre of Nabro caldera was detected, nor lateral variations around the volcano, suggesting that the lateral distribution of anisotropy beneath the caldera is relatively homogeneous.

5.3.2 *b* - value

Local magnitudes at Nabro volcano for the August-December 2011 period range between 0.2 and 3.7 (Figure 5.8a). The frequency distribution shows a magnitude of completeness of M_C = 1.30 and a *b*-value = 1.17 ± 0.06 (Figure 5.8b). These results agree with the range of previous estimation for Nabro volcano. For the same period (August-December 2011), Goitom (2017) assessed *b*-value = 1.14 ± 0.09 (Figure 5.5b), for a data set slightly bigger (1835 events), as the events extend further laterally and deeper in the crust. The slightly bigger *b*-value might be due to a focus on events beneath the caldera, which might be more fractured and fluid-rich than regions below the flanks of the volcano. Hamlyn et al. (2014) calculated *b*-value = 1.30 ± 0.08 for a period of 36 days immediately after the deployment of the local seismic array (Figure 5.5a). This higher *b*-value is likely due to its temporal proximity to the eruption period, suggesting there is more fracturing and fluids in the period immediately following the eruption.

5.3.3 Fast shear wave orientation

Due to the location of the seismic stations with respect to the earthquakes swarm, most of the SWS measurements are made using the NAB1 station (170 of a total of 200 SWS measurements). Over the August-December period, fast shear wave polarisations exhibit an overall NW-SE orientation (Figure 5.9). Any lateral variation in ϕ is investigated by computing fast orientation ϕ for the 4 stations (NAB1, NAB2, NAB3, and NAB5), which recorded reliable SWS measurements (Figure 5.9). The other stations are too distant from the earthquake swarm to record signals within the shear wave window. Although most of the data are constrained around NAB1, the 4 clusters show consistency in their trends of fast orientation, suggesting the source of anisotropy extends evenly beneath the caldera.

This NW-SE orientation is parallel to the Red Sea trend and to the western margin of the Danakil micro-plate, and perpendicular to the direction of opening between the Arabian and Nubian plates (Figure 5.1). This trend is also parallel to the maximum horizontal stress, σ_{Hmax}, in the region as highlighted in the 2016 World Stress Map project (Figure 5.10 ; Zoback, 1992; Heidbach et al., 2018). A series of field- and remote-based observations tends to confirm this

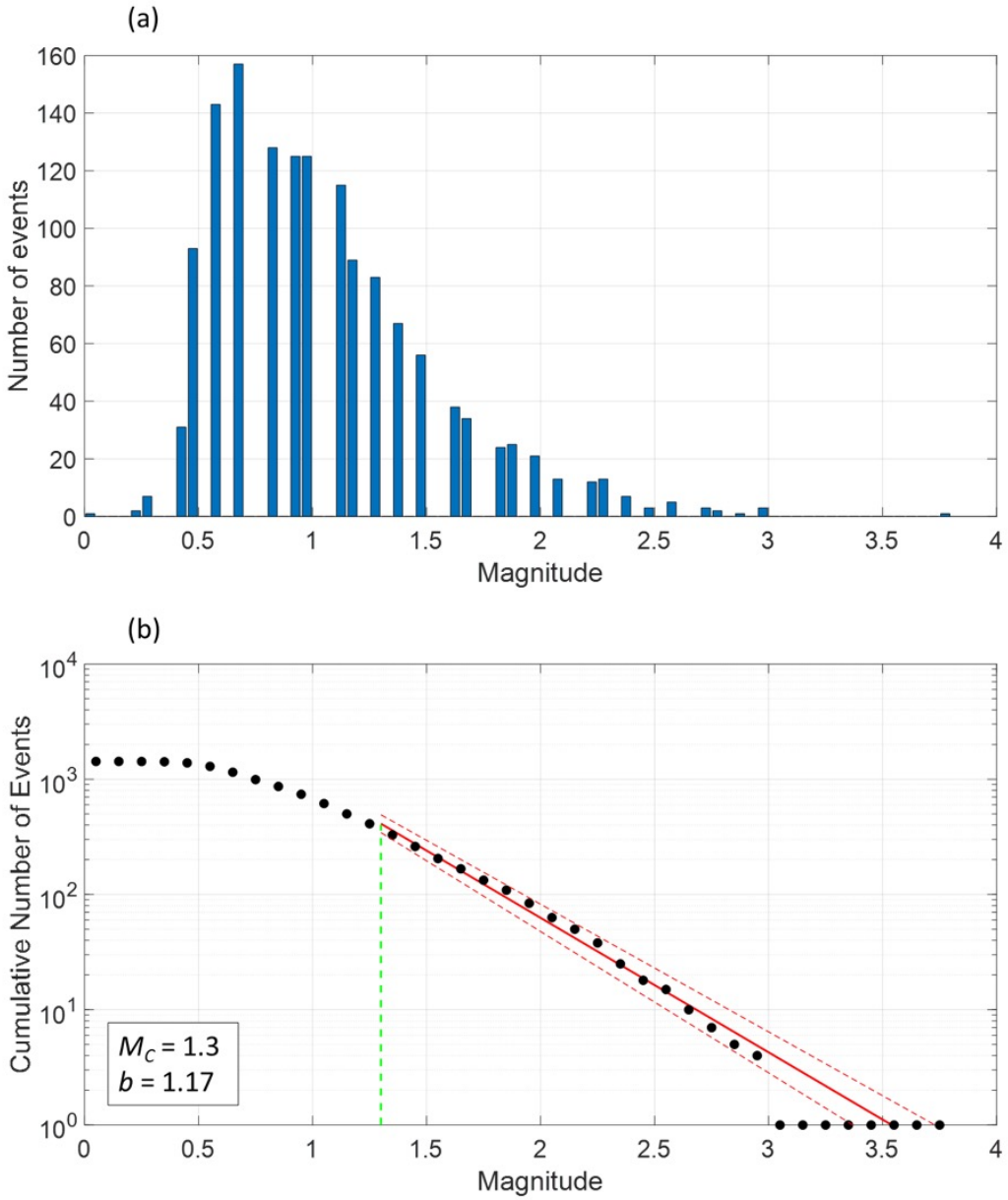

Figure 5.8 Distributions of earthquake magnitudes for the catalog of manually located earthquakes below Nabro. (a) Histogram of the events magnitude (bins are 0.05 magnitude width). (b) Gutenberg-Richter plot for the events. b-value is the solid red line and the 95% of confidence intervals are the dashed red lines. Magnitude of completeness (M_C) is indicated by the dashed vertical green line.

trend, such as the alignment of small pits and volcanic vents along a NW-SE axis (Hamlyn et al., 2014; Goitom et al., 2015). Tensile cracks up to 10 m long outcropping at the surface and

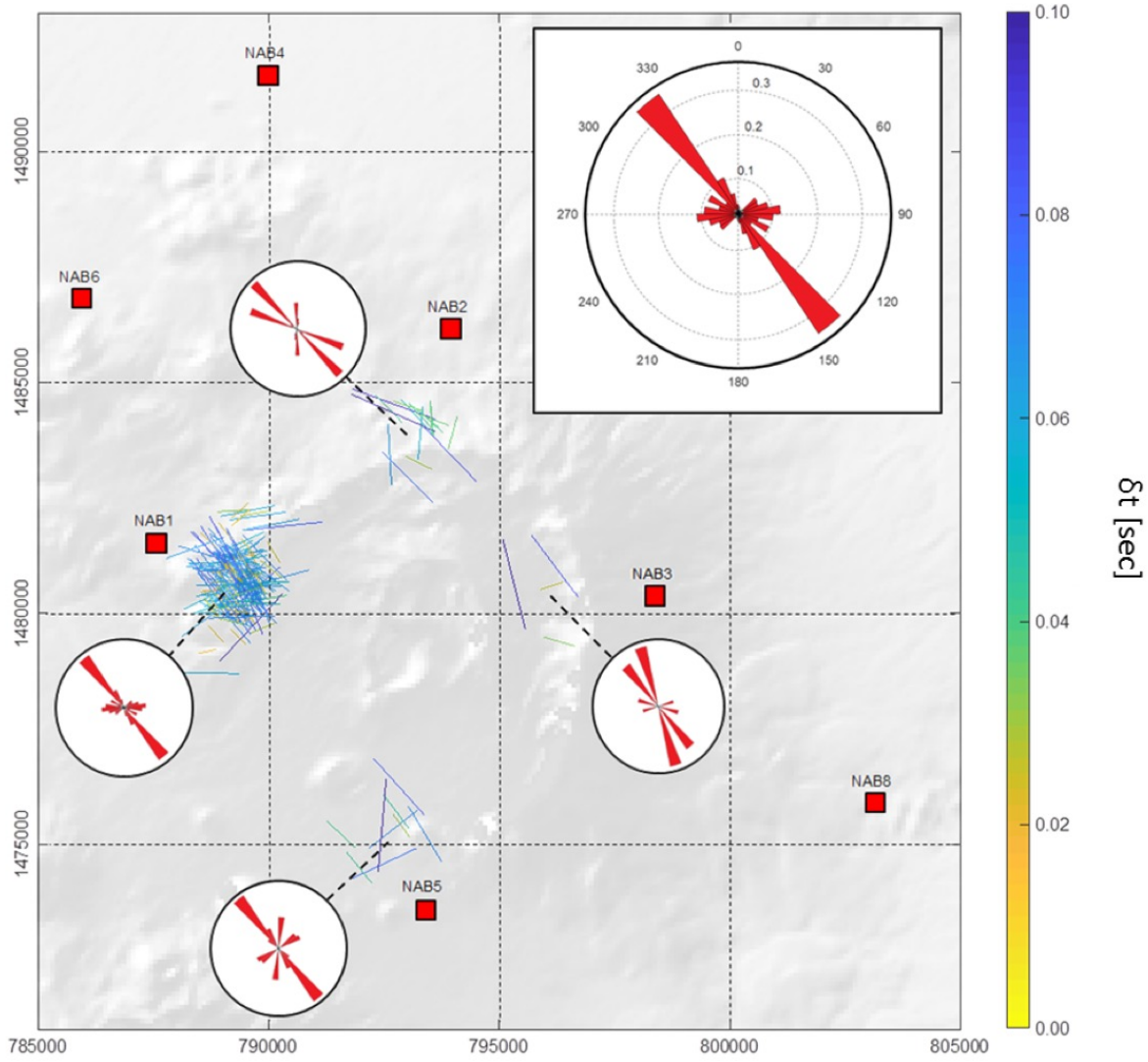

Figure 5.9 Orientation of the fast shear wave polarisation (coloured ticks). The colour and the length of the ticks are proportional to the delay time between the fast and the slow shear waves (δt). Large rose diagram in insert shows the overall trend of ϕ. The 4 rose diagrams on the map show the trends for each cluster related the 4 stations which recorded reliable signals for SWS measurements.

striking NNW-SSE were also reported just after the eruption (Ogubazghi and Goitom, 2014), as well as crustal faults in the region, even if small variations appear locally (Illsley-Kemp et al., 2017).

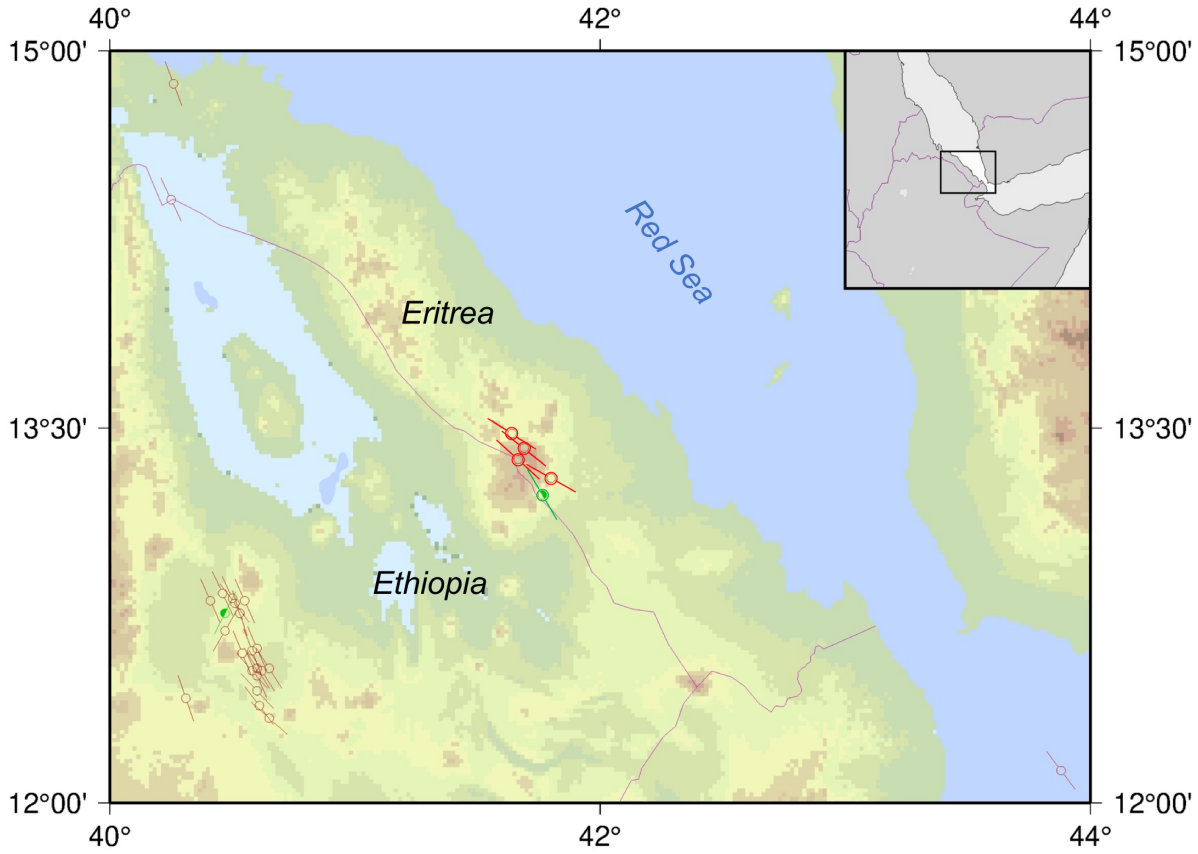

Figure 5.10 Stress map showing the orientation of the maximum horizontal compressional stress σ_{Hmax} (ticks of the symbols) around Nabro volcano. Focal mechanisms show a NW-SE trend of σ_{Hmax}. Green symbols show strike-slip. Red symbols correspond to normal faulting. Modified from the 2016 version of the World Stress Map project (Heidbach et al., 2016).

5.4 Discussion

A change in the orientation of the fast shear polarisation is visible before and after 8 October 2011 (Figure 5.11). For the first period, the ϕ orientation is roughly East-West, with some signal in the NW-SE direction. The second period is clearly dominated by a NW-SE orientation of ϕ, parallel to the Danakil axis.

In order explain the observed delay time and fast polarisation direction, as well as the temporal variation in ϕ, a series of rock physics models based on the additional compliance approach are used to estimate the elastic stiffness tensor (Schoenberg and Sayers, 1995). This

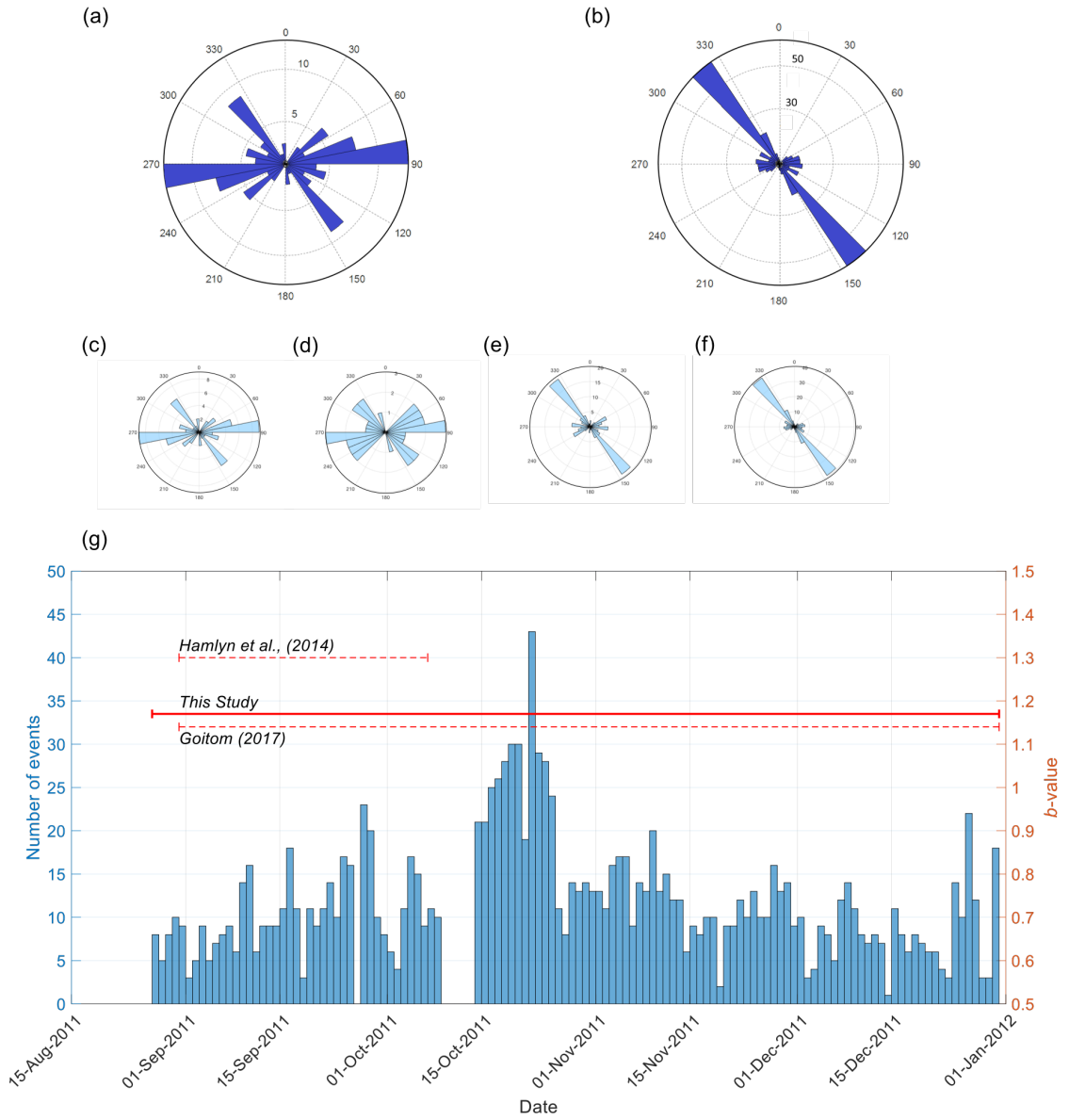

Figure 5.11 Variations in the fast shear wave polarisations with time at Nabro. Dark blue rose diagrams show the orientation of the fast shear wave for the periods (a) before and (b) after the 15 October 2011. Small light blue rose diagrams show 4 subdivisions: (c) 27 August to 15 September 2011, (d) 16 September to 14 October 2011, (e) 15 October to 15 November 2011, (f) 16 November to 31 December 2011. These highlight a transition between an E-W trend to a NW-SE trend. (g) Number of events per day. The lack of data between the 8 October and the 15 October 2011 is due to only three stations working during this period. Solid red line shows the calculated *b*-values for the 4-month period. Red dashed lines indicate average *b*-values from Hamlyn et al. (2014) and Goitom (2017).

method has been used to explain rapid changes in the state of stress that affect the fracture properties, including settings such as hydraulic fracturing (Verdon et al., 2009; Verdon and Wüstefeld, 2013; Baird et al., 2013b), CO_2 storage (Verdon et al., 2011), and mining activity (Wuestefeld et al., 2011a).

The additional compliance introduced by a set of aligned cracks varies as a function of their orientation (strike and dip), density (Hudson et al., 1996), and compliance (Verdon and Wüstefeld, 2013). A series of models composed of one or two sets of vertical cracks with different parameters are tested. A grid search over these parameters is performed to find the model which minimise the difference between the observed and modelled SWS parameters. In each scenario, synthetic SWS are produced using the Christoffel equation and misfit with the observations is calculated, using the Matlab seismic anisotropy toolbox (MSAT; Walker and Wookey, 2012). An isotropic background was also assumed, since sub-vertical raypaths will not be significantly affected by horizontal layering (Kendall et al., 2006).

The best fitting model consists of an isotropic background containing 2 sets of vertically aligned fractures, one oriented NW-SE, and the other oriented NE-SW (Table 5.2). For the first half of the period (before 8 October 2011), $\xi^{(1)} = 0.05$ and $Z_N/Z_T{}^{(1)} = 0.8$ for the NW-SE set, while $\xi^{(2)} = 0.05$ and $Z_N/Z_T{}^{(2)} = 0.75$ for the NE-SW set (Figure 5.12). For the second-half of the period (after 15 October 2011), $\xi^{(1)} = 0.05$, $Z_N/Z_T{}^{(1)} = 1.00$, $\xi^{(2)} = 0.01$, and $Z_N/Z_T{}^{(2)} = 0.2$ (Figure 5.13).

Table 5.2 Parameters of the best fit models at Nabro for the first and second half of the period of interest. Note that the strikes are in degrees from North and positive in the clockwise direction.

Period	Strike$^{(1)}$[°]	$\xi^{(1)}$	$Z_N/Z_T{}^{(1)}$	Strike$^{(2)}$[°]	$\xi^{(2)}$	$Z_N/Z_T{}^{(2)}$
27/08/11 - 08/10/11	130	0.05	0.8	50	0.04	0.7
15/10/11 - 31/12/11	130	0.05	0.9	50	0.01	0.2

The first period shows 2 sets of fractures with similar characteristics. This is highlighted

in the misfit surface which is displayed as a function of the densities of the two fracture sets (Figure 5.12c). The SWS observations from the first period require the two fracture densities to be about the same value.

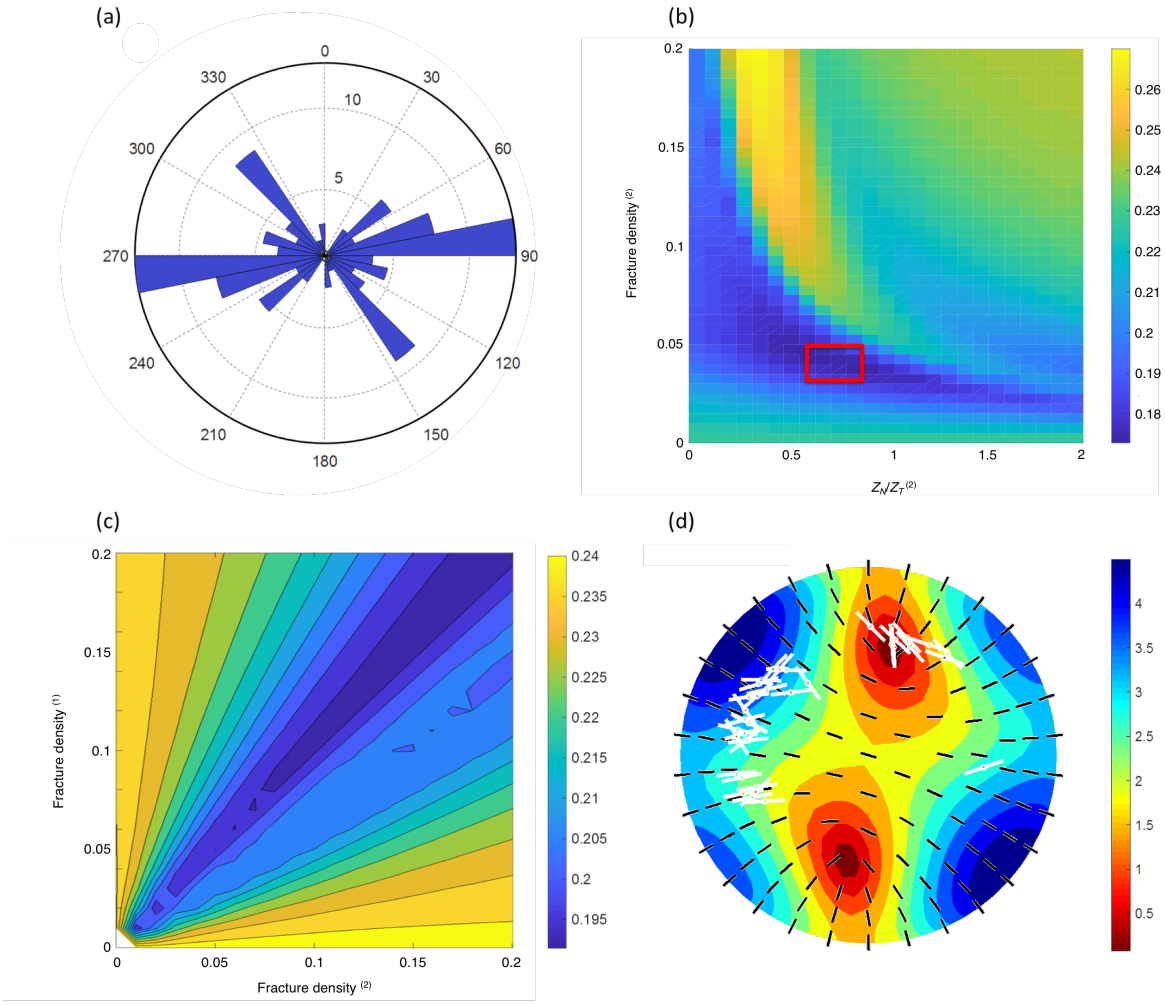

Figure 5.12 Best fitting model for the 27 August to 5 October 2011 period. (a) Rose diagram for the fast shear wave orientation. (b) Misfit surface as a function of crack density ($\xi^{(2)}$) and fracture compliance ratio ($Z_N/Z_T{}^{(2)}$) of the NE-SW fracture set. The minimum misfit is indicated by the red square. (c) Surface plot of the misfit as a function of the crack density of the two fracture sets. (d) Upper hemisphere polar plot of the measured shear-wave splitting results (white ticks). The orientation of the ticks gives ϕ, while their length marks δt. Black ticks indicate the synthetic fast shear polarisation and the filled contours show δt for the best fitting model.

In contrast, during the second half (after 15 October 2011), the NW-SE set tends to be the

dominant one (Figure 5.13). The fracture density for the NW-SE set must be larger than that of the NE-SW set. The extreme reduction in crack density of the second set, $\xi^{(2)}$, which tends to zero, can be assumed to be due to the closure of the cracks in these orientations. Likewise, the decrease of $Z_N/Z_T{}^{(2)}$ represents here a stiffening of the NE-SW fracture set.

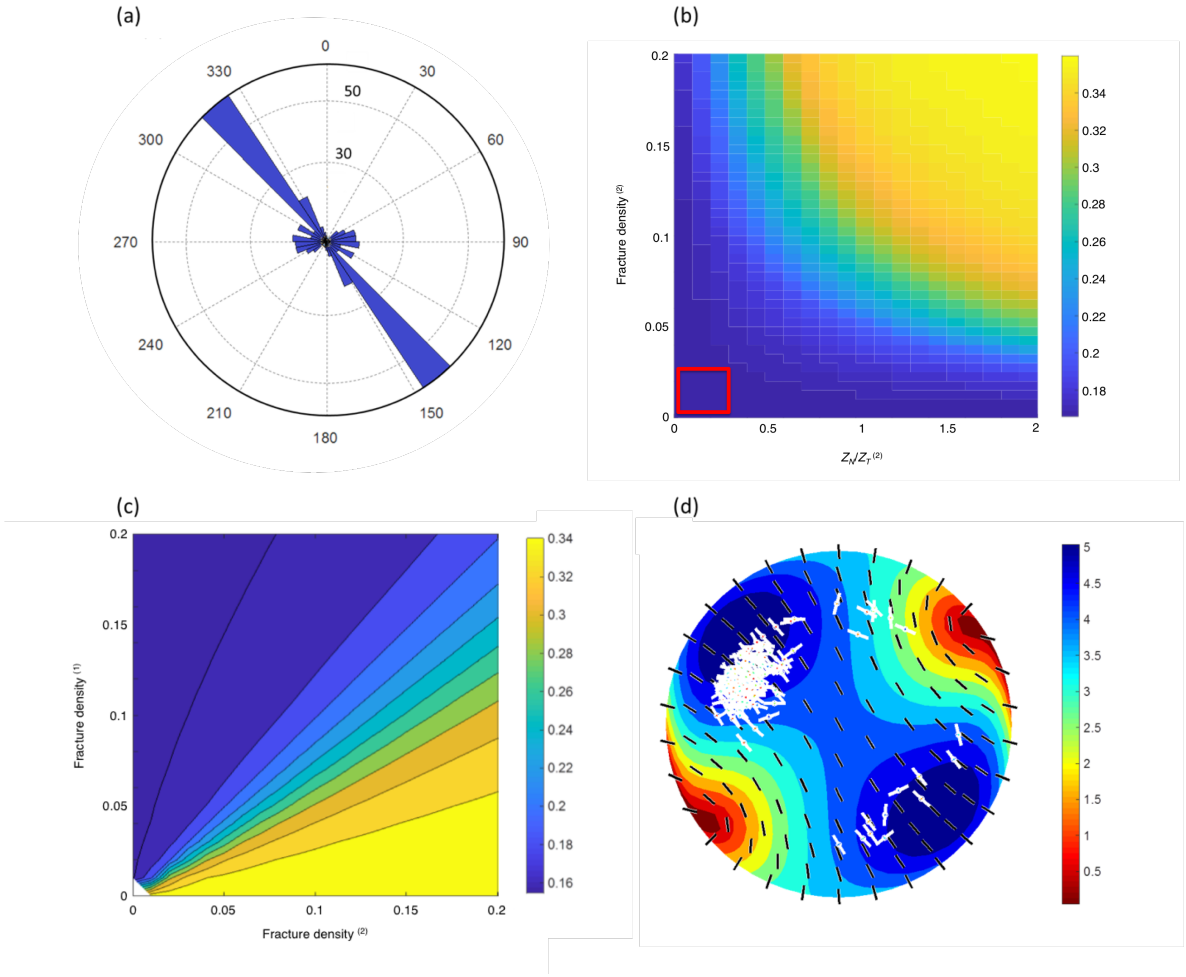

Figure 5.13 Best fitting model for the 6 October to 31 December 2011 period. (a) Rose diagram for the fast shear wave orientation. (b) Misfit surface as a function of crack density ($\xi^{(2)}$) and fracture compliance ratio ($Z_N/Z_T{}^{(2)}$) of the NE-SW fracture set. The minimum misfit is indicated by the red square. (c) Surface plot of the misfit as a function of the crack density of the two fracture sets. (d) Upper hemisphere polar plot of the measured shear-wave splitting results (white ticks). The orientation of the ticks gives ϕ, while their length marks δt. Black ticks indicate the synthetic fast shear polarisation and the filled contours show δt for the best fitting model.

The most plausible source of changes in anisotropy over a short period of time (i.e., few

weeks) is a significant change in the stress field in the medium (Savage, 1999). The most obvious cause of stress variation is the contemporary volcanic activity at Nabro and the related magma intrusion in the shallow crust. Based on inversion modelling of the ground deformation measured by Synthetic Aperture radar (SAR) imagery, a dike striking NW-SE and located 0.3-4.3 km below the caldera has been inferred (Figure 5.14). This dike is aligned with the maximum principal stress in the region (Goitom et al., 2015; Hamiel and Baer, 2016). This is also consistent with the observed vents aligned NW-SE (Goitom et al., 2015).

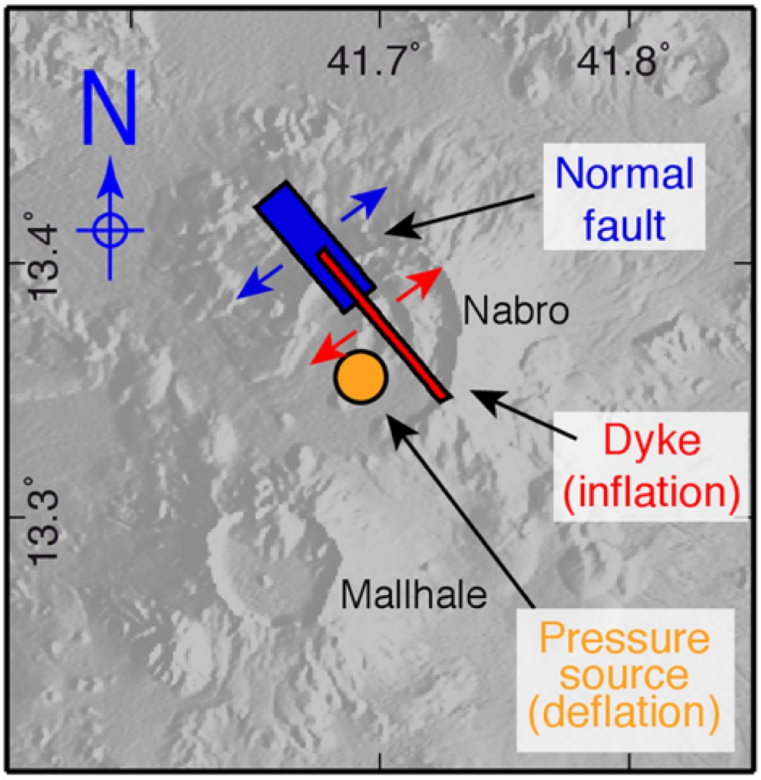

Figure 5.14 Deformation features inferred from SAR analysis of ground displacement at Nabro, including the NW-SE striking dike (red shaded area). This model also includes a NW-SE normal fault (blue shaded area) and a Mogi source (orange dot) located 6.3 km below the surface. Source: Goitom et al., 2015.

Dike injections have been previously described as potential source of stress during volcano unrest, using shear-wave splitting (Gerst and Savage, 2004) and volcano-tectonic seismicity

analysis (Roman et al., 2004; Roman, 2005; Roman and Cashman, 2006; Lehto et al., 2010). As magma is intruded into a vertical dike from a deeper source, the dilatation acts in the direction of the minimum stress component σ_h, increasing its magnitude, and perpendicular to the regional stress σ_{Hmax} (Figure 5.15 ; Parsons and Thompson, 1991; Gerst and Savage, 2004).

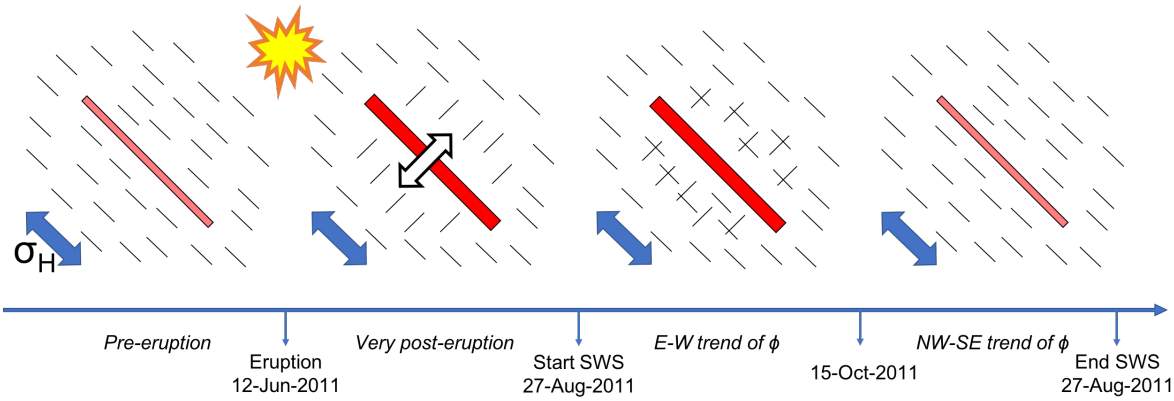

Figure 5.15 Schematic representation of the variation of the local anisotropy below Nabro volcano. The NW-SE striking dike is represented by a red rectangle. Blue arrow shows the maximum stress component. White arrow shows the dike-induced local stress field, perpendicular to the regional σ_H. Black ticks indicate the orientation of fractures. Adapted from Gerst and Savage (2004).

At Nabro, one or several sequences of dike inflation likes occurred during the eruption, causing the local maximum stress component, σ_H, to migrate to a NE-SW trend. As the fast shear orientation transitions back to the regional NW-SE trend by October 2011, the first half of the monitoring period captures the transition between the anomalous NE-SW and the normal regional NW-SE trend. The surveyed period captures the relaxation of the volcanic system under Nabro back to the normal stress setting. This is consistent with observations of continuous surface subsidence measured using satellite imageries during the period following the eruption (Hamlyn et al., 2018).

Since the seismic array was deployed after the eruption period, the exact moment of the rotation of the local stress could not been directly observed. However, it is assumed here that the rotation occurred before the eruption itself, as the magma fills the shallow dike system (Bianco et al., 2006). Monitoring stress variation under active volcanoes using SWS has thus

the potential to help forecast major eruption events on a short- to mid-term basis, as suggested by Gerst and Savage (2004).

This study shows the effectiveness of using a combination of seismic analysis to investigate fractured reservoirs. SWS is useful to map fractures and detect temporal variations in stress and fracturing. In addition, high b-values indicate a fractured and fluid-rich system, typical of volcanic settings, particularly at the start of the recording period, when fluid pressure is high enough to maintain open two orthogonally oriented sets of cracks. Temporal changes in anisotropy might help in forecasting at short time scales. Complementary techniques, such as temperature logs (**?**) and flow-meter measurements (**?**), could bring more information about the hydraulic conductivity of the fractures (Barton et al., 1995), and assess the viability of the reservoir.

5.5 Conclusions

An array of 8 broadband seismometers was deployed on the flanks of Nabro volcano a few weeks after it erupted on 12 June 2011. Shear-wave splitting is measured on a dataset consisting of manually located events detected between the end of August and the end of December 2011. No trend in δt with depth is detected, showing than most of the anisotropy is contained in the shallow subsurface ($<$ 3km).

In general, the polarisation of the fast shear wave, ϕ, aligns with the regional direction of minimum horizontal stress (NW-SE), which is the trend of the Red Sea opening and the western margin of the Danakil micro plate. However, an E-W trend in ϕ is visible early in the monitoring period, but not in the late period. This is explained by involving the presence of two fracture sets, one aligned with the regional stress field and a second orthogonal set aligned with the Nabro-Dubbi volcanic chain. Dike inflation and pressurisation of the hydrothermal system modify the stress field, opening the second set of fractures at the time of eruption. The fast orientation re-orients along the regional horizontal maximum stress after the deflation of the dike and the closure of the orthogonal set of cracks. This study shows the effectiveness

of using SWS to map fractures and detect temporal variations in stress and fracturing. High b-values indicate a fractured and fluid-rich system, typical of volcanic settings, particularly at the start of the recording period, when fluid pressure is high enough to maintain open two orthogonally oriented sets of cracks. Temporal changes in anisotropy might help in forecasting at short time scales.

Acknowledgments

Rapid deployment of the SEIS-UK broadband seismometers was funded by the NERC urgency grant NE/J012297/1.

CHAPTER 6

Conclusions and perspectives

Abstract

Throughout this thesis, the focus has been on imaging and characterising fracture networks using seismic methods. In this chapter, the main outcomes of this work are summarised, covering the three chapters presenting the results: (i) fracture mapping using a UAV, (ii) active seismic experiments at Lilstock, and (iii) fracture characterisation at Nabro volcano using microseismic. From the observations of fracture-induced anisotropy at Lilstock and Nabro, fracture compliances and fracture compliance ratios have been evaluated. The results from chapters 3 and 4 will form the body of a single publication in an international peer-review journal. The results from shear-wave splitting measurements at Nabro will also be submitted for review in an international journal. In addition, potential future work is presented at the end of the chapter.

6.1 Fracture mapping at Lilstock

The Lilstock wave-cut platform is located on the southern margin of the Bristol Channel Basin, UK. The limestone outcropping at the surface is highly fractured. A software-controlled UAV was used to take a series of photographs over a 20 × 25 m outcrop situated on the East-West oriented hinge of an anticline. A mosaic of high spatial resolution was created from these photographs. Fractures and cracks were manually digitised, allowing the characterisation of the joint network within the mapped area. Main results of this mapping campaign are listed below.

- Two sets of joints were detected, the first striking East-West and consisting in long fractures extending up to tens of meters. The second set contains smaller cracks, generally much less than 1 meter long. Although these cracks show some alignment in the North-South direction, they also show populations of orientation at intermediate angles, making the overall orientation trend of these cracks slightly more random than the long East-West fractures.

- The joint network of the mapped outcrop exhibits significant heterogeneity, even over short distances. This is particularly true for the crack intensity and the crack orientation. These two parameters show large variability between the northern and southern parts of the outcrop. Such variability in joint parameters is likely to be related to their position relative to the anticline.

- These quantitative measurements of joint variability highlight the heterogeneity that can be present at a single outcrop and the related heterogeneity in elastic properties, such as fracture compliance. This can help better explain the scattering commonly seen in seismic data that is interpreted in terms of fracture characteristics.

6.2 Seismic experiment at Lilstock

Three pairs of *P*- and *S*-wave seismic surveys were performed on the Lilstock wave-cut platform, at the location of the outcrop mapped using the UAV. The first objective of these surveys was

to recover the orientation of the observed fractures using observations of seismic wave speeds as a function of azimuth. Second, time-lapse seismic surveys were used to detect potential changes in seismic anisotropy due to fractures drainage as the tide recedes. Main findings of the seismic survey are listed below.

- Because of the configuration of the seismic survey and the clearer first arrivals, the P-wave surveys give better results in order to investigate fracture-induced anisotropy. They cover a larger range of azimuths and exhibit a greater difference between the maximum and the minimum values of velocity. Nevertheless, the S_H-wave data help to better constrain the fracture model that best fits the data.

- The measured azimuthal variation in seismic velocities agrees well with the orientation of the E-W fractures mapped at the outcrop surface. P-wave velocities show a maximum in the direction of the strike of the E-W fractures, and a minimum in the N-S direction of propagation. On the other hand, S_H-wave velocity is minimum in the East-West direction, as expected.

- Local anisotropy is controlled by the long East-West fractures. No detectable signal is inferred from the cracks.

- An increase in the seismic velocities up to 8% was detected over time, as the tide retreats. This was mostly pronounced for the case of the P-waves between the first and the second surveys (i.e., before low tide).

Figure 6.1 Compilation of Z_N/Z_T measurements in field settings and for laboratory samples, respectively above and below the dashed red line. The results for Nabro and Lilstock aare shown at the top of the plot.

- Inversion for the normal and tangential fracture compliance was derived from the *P*- and *S*-wave surveys. The fracture compliance ratio at Lilstock varied with the tide. Values of Z_N/Z_T from 0.18 to 0.40 and 0.48 were estimated as the fractures drained. However, the increase in Z_N/Z_T was mostly controlled by a drop of the tangential component, while the normal compliance remains stable (Figure 6.1). A suggested reason for this is a loss of cohesion in the clay filling the fractures.

- Observed fracture length and estimated fracture compliance are consistent with the scaling relationship proposed by Worthington and Lubbe (2007). The Lilstock results are in agreement with previous measurements made on laboratory samples and in the field (Figure 6.2).

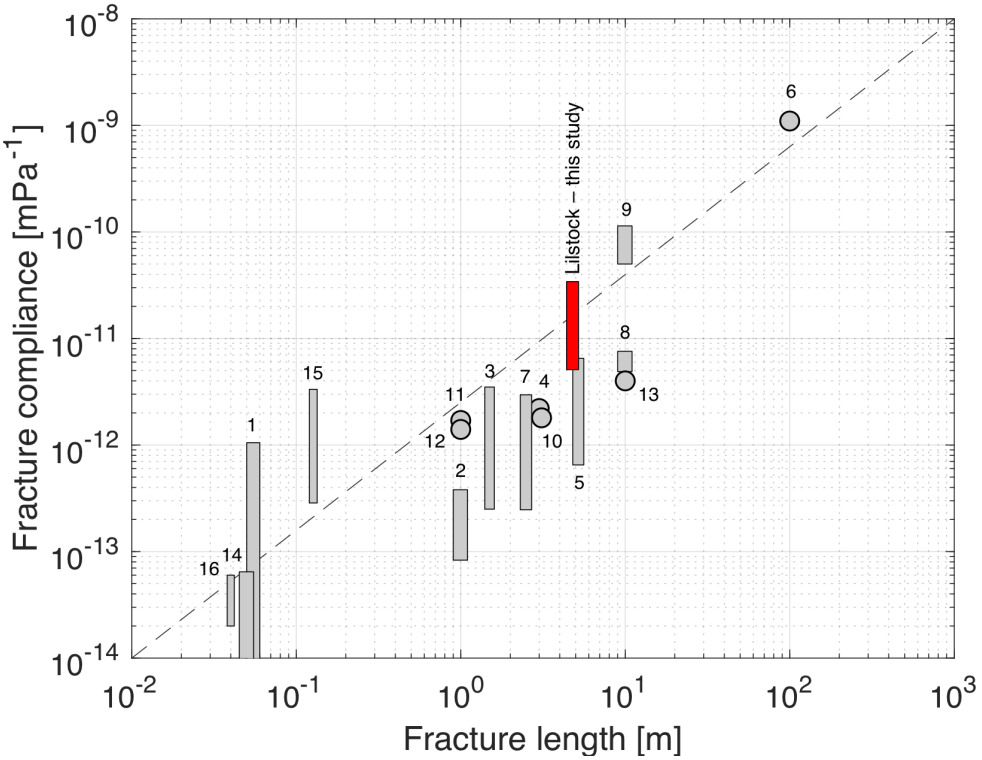

Figure 6.2 Results of individual fracture compliance, B_N and/or B_T, as a function of fracture length for the seismic experiment at Lilstock (red bar). Modified and updated from Worthington and Lubbe (2007); Verdon and Wüstefeld (2013); Foord et al. (2015).

6.3 SWS measurements at Nabro volcano

Nabro volcano, located in Eritrea, erupted on the 12^{th} June 2011. A catalogue of manually located earthquakes recorded by a surface array and covering a period of 4 months was analysed. Shear-wave splitting (SWS) analysis is used to investigate fracture-induced anisotropy. The orientation of the fast shear-wave polarisation, ϕ, is assumed to be dominated by aligned sub-vertical fractures, as commonly observed in hydrothermal systems. In addition, delay times between the fast and the slow shear-waves, δt, indicate the strength of the anisotropy. The splitting parameters are useful to study the spatial and temporal extent of the fracture-induced anisotropy. Main results and conclusions are listed below.

- A b-value of 1.17 was calculated for the period of interest. This result is consistent with previous estimates and indicates a fractured and fluid-rich system.
- Measurements of fast shear-wave polarisation, ϕ, show an overall NW-SE trend, parallel to the Red Sea axis and to the western margin of the Danakil micro-plate. No obvious spatial variations in the fast shear wave polarisation was observed, indicating no lateral heterogeneity in the anisotropy in the upper crust.
- However, the orientation of the fast shear-wave polarisation varies over time. The orientation migrates from an E-W trend between September and October to a NW-SE trend after mid-October. This later trend remains stable during the second half, from mid-October to the end of December.
- A rock-physics based model composed of two distinct fracture sets is used to explain the temporal variations in ϕ. The first set is aligned with the NW-SE regional stress field. The second set is oriented NE-SW along the Nabro-Dubbi volcanic axis and the trend in seismicity during the eruption. Between the end of August and mid-October, the two sets of fractures are both open and show similar densities and compliance ratios. Between mid-October and the end of December, the NE-SW fractures close, while the NW-SE set remains open and dominates the local anisotropy.

- The change in ϕ is caused by a change in the stress regime, which is attributed to the emplacement of a dike beneath the caldera. It strikes NW-SE and aligns with the regional maximum horizontal stress. Over-pressurisation creates a local increase in the NE-SW horizontal stress and opens fractures in this direction.

- An interpretation of these observations is that, between the eruption and mid-October, the fluid pressure is high enough to maintain open two orthogonally oriented fracture sets. After mid-October, the system relaxes back to the ambient state (i.e., pre-eruption conditions), with a dominant NW-SE fracture set, parallel to the maximum horizontal stress.

- An unknown parameter is the timing of the switch in ϕ. It is likely that the switch occurs before the actual eruption. In which case SWS observations have the potential to be used as a short- to mid-term forecasting tool.

- No trend in δt with depth or source-receiver distance is observed. The shear-wave anisotropy shows a decreasing trend with depth (and source-receiver distance), indicating that the source of anisotropy is located in the upper 3 km of the crust.

- Nabro is a promising site for geothermal energy. The splitting parameters provide insight into the fracture network, which is useful information in the development of a geothermal reservoir.

6.4 Z_N/Z_T

The values of Z_N/Z_T measured at Lilstock are relatively low, in comparison with the range of published literature results (Figure 6.1). This is attributed to low connectivity in the joint network on the wave-cut platform. The UAV-derived topology analyses of the mapped joints at Lilstock revealed a high proportion of abutting fractures and cracks. Furthermore, the some small cracks show signs of cementation.

In comparison, values of Z_N/Z_T measured at Nabro volcano are higher. This can be attributed to the hydrothermal system having a well-connected fracture network. Connectivity is enhanced during the eruption.

The inversion approach for Z_N/Z_T described in earlier chapters is tested on data from recently published SWS measurements made on other volcanoes.

Nowacki et al. (2018) measured SWS at Aluto volcano, in the Main African Rift, to characterise the associated hydrothermal system. They found $\phi = 13 \pm 7$ degrees for the overall dataset and measured δt values between 0.01 and 0.23 seconds. They determined the shear-wave anisotropy to range between 0 and 14%. They attributed the seismic anisotropy to the presence of two sets of fractures, being oriented at 12 and 90 degrees from North and having a crack density of 0.15 and 0.0825, respectively.

Maher and Kendall (2018) investigated crustal anisotropy by measuring SWS at Uturuncu Volcano, Bolivia. They found ϕ to show high range of variation, which they attributed to a combination of magmatic and tectonic stresses. They determined an average δt of 0.06 seconds and the shear wave anisotropy to range between 0.25 and 6.2%. They interpret their results by the presence of two orthogonal fault systems, one being oriented NW-SE, and the other NE-SW.

The splitting parameters measured at Aluto and Uturuncu are inverted for fracture compliance ratios. Table 6.1 summarise the results of the inversion Z_N/Z_T at Lilstock, Uturuncu, Nabro and Aluto.

At Aluto, high values of Z_N/Z_T suggest a high connectivity in the hydrothermal system. Nowacki et al. (2018) argued that the fluid pressure is able to activate both fracture sets at the same time. In comparison, such high values ($1 < Z_N/Z_T < 2$) have been also observed during hydraulic fracture stimulation, and attributed to the enhancement of the fracture network (Verdon and Wüstefeld, 2013). Similar effects are likely to occur in volcanic settings with active and fluid-rich hydrothermal system, where the fluid pressure is able of opening new fractures

and holding open existing ones.

At Uturuncu, the estimated values of Z_N/Z_T are low in comparison with Nabro and especially with Aluto. This is particularly true for the NE-SW fracture set. Based on earthquakes recorded between June 2009 and March 2012, Maher and Kendall (2018) calculated unusually low b-values (0.66). This highlights the poorly developed fracture network and the little influence of fluid beneath Uturuncu.

Table 6.1 Fracture compliance ratio at Lilstock (UK), Uturuncu (Bolivia), Nabro (Eritrea) and Aluto (Etiopia). Note that the strikes are in degrees from North and positive in the clockwise direction.

	$Strike^{(1)}$	$Z_N/Z_T^{(1)}$	$Strike^{(2)}$	$Z_N/Z_T^{(2)}$
Lilstock	90	0.18-0.40-0.48*		
Uturuncu	330	0.6	45	0.1
Nabro	130	0.8-0.7**	50	0.9-0.2**
Aluto	12	1.5	90	2.5

*as the tide retreats.
**before-after mid-October.

6.5 Further work and future directions

This section aims to propose potential routes of investigation to extend the work presented throughout this thesis.

- Additional seismic experiments should be carried out on fractured platforms affected by tide. So far, only 2 studies made on such outcrops have been published, although they only consisted of single surveys, not allowing the detection of temporal variations in fracture attributes (Foord et al., 2015; Hobday and Worthington, 2012). These sites represent a unique field laboratory to study fracture networks and develop methods of characterisation. Most of these are easily accessible and have already been structurally investigated (e.g., Donovan and Foster, 1972; Peacock and Sanderson, 1999; Welch et al., 2015). They allow experiments at the reservoir scale in known and varying conditions.

Figure 6.3 shows some examples of fractures outcrops located on the coast line around the UK that could potentially been investigated using seismic refraction surveys.

Figure 6.3 Non-exhaustive list of fractured wave-cut platforms located in the UK.

- Other complementary geophysics surveys could be carried out on these fractured coastal platforms. In particular, measurements of resistivity have the potential to provide insights into fluid saturation (Koster and Harry, 2005; Mack and Degnan, 2003), and bring complementary data to the seismic observations.

- Laboratory analysis of a fractured rock sample from such outcrop formations should provide quantitative information about fracture-induced permeability and porosity. Detailed analysis of the infill material could also give information about the causes of the observed variations in fracture compliance. These data can help constrain the rock physics model used in the inversion approach.

- In the case of Nabro volcano, further effort should be made in locating the events from January to October 2012. The automatic picking of *P*- and *S*-phases does not provide reliable event locations to confidently analyse the seismic signals and measure shear-wave splitting. Although manual picking is a time-consuming process, it is a necessary step to minimise error in the results. Migration methods might provide a more automated alternative.

- Extending the manual picking can also improve the azimuth-offset coverage of the seismic data cloud. This could help in the inversions for fracture characteristics, such as fracture compliance ratio.

- In order to improve future deployments of local seismic arrays on Nabro or other volcanoes, one or more stations should be located above the main swarm of seismic activity (Figure 6.4). This will result in an increase of the number of signals fitting into the shear wave window. It would be hence possible to measure SWS over the whole vertical and lateral extensions of the column of earthquakes. This would lead to a better coverage of the offset and azimuth of the propagation of shear waves (Figure 6.5). Furthermore, this should help better constrain the rock physics models used to identify the source of anisotropy and determine the fracture characteristics.

- Results have the potential to better constrain numerical models of the influence of dike intrusion on the local stress field.

- At Nabro, SWS analysis on distant stations (e.g., NAB4, NAB7 and NAB8) could confirm to what extent is the anisotropy confined to the region beneath the volcano. This would require earthquakes outside the caldera.

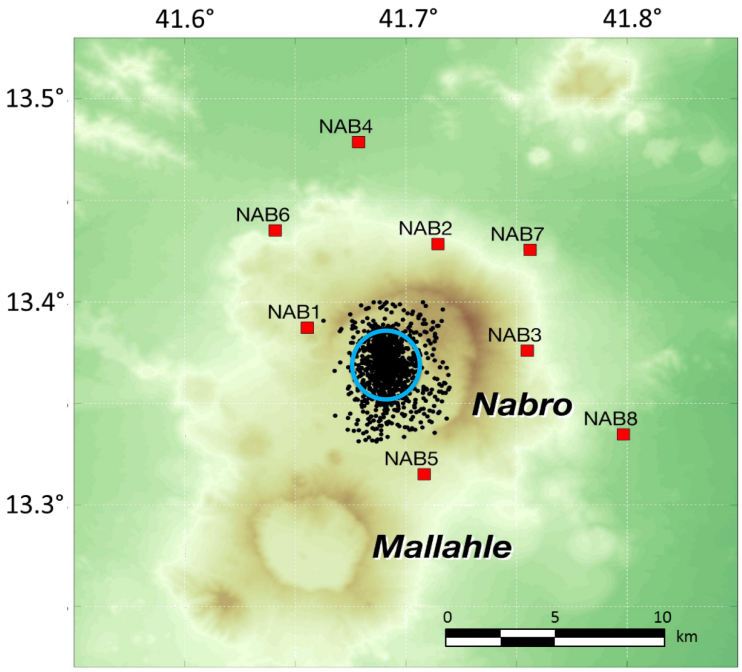

Figure 6.4 Seismic array deployed around Nabro volcano between August 2011 and October 2012 (red squares). The blue circle shows where the deployment of one or more stations should result in the improvement of the SWS analysis.

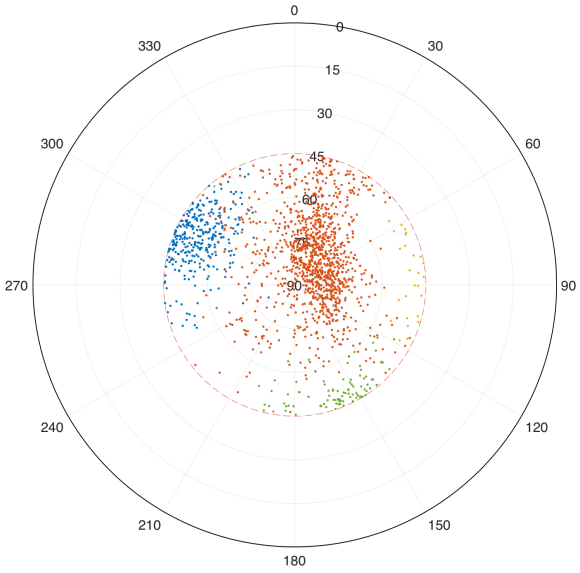

Figure 6.5 Polar plot showing improved coverage of arrivals resulting from the installation of a surface station within the blue circle of Figure 6.4.

APPENDIX A

Shear wave source

Abstract

This appendix describes the shear-wave seismic source designed and built at the University of Bristol. The source was initially used during the seismic survey at Lilstock to generate horizontal shear waves in the fractured limestone (see Chapter 4). It has been used in several subsequent seismic experiments, including fieldwork with students from the School of Earth Sciences.

A.1 Introduction

Near-surface seismic surveys usually employ compressional (P) or horizontally polarised shear-waves (S_H), or a combination of both. These wave types are be easily distinguishable from each other. P-waves are simply generated by striking a horizontal plate or surface. In contrast, S_H require the use of a more elaborated source.

A common way to create S_H-waves require horizontal traction with the ground surface. The resulting S_H-wave energy propagates sub-perpendicular to the strike direction and is then

registered with an array of horizontal geophones. For S_H-wave surveys, both the source and the geophones are oriented perpendicular to direction of propagation of the S_H-wave. Some P- and S_V-waves energy is also generated by such a source but propagate most strongly in the direction parallel to the strike direction. The 360 degrees radiation pattern for an impulsive surface traction source is shown in Figure A.1.

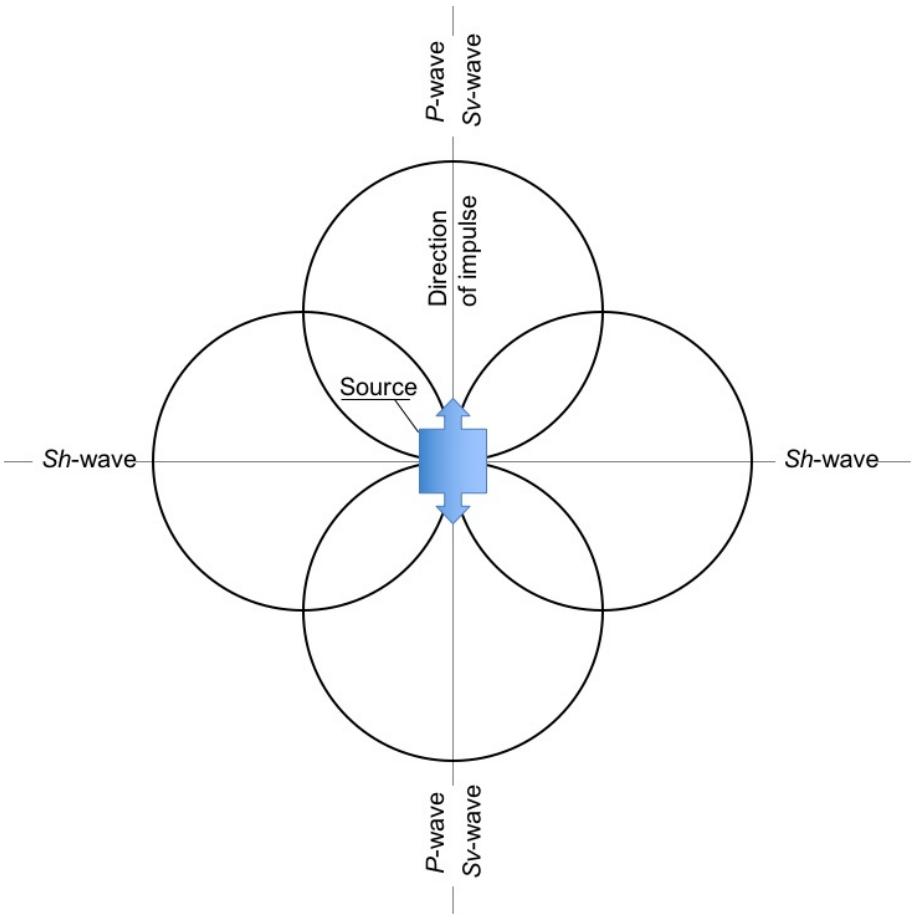

Figure A.1 Radiation pattern induced by a hammer shear-wave source. The blue arrows show the direction of impulse. Modified form Franklin (1979).

A number of sources have been designed in order to perform S_H-wave seismic refraction surveys. The most simple design consists in a wood plank directly placed on the ground (Franklin, 1979). The plank is struck horizontally on its edge with a sledgehammer. Slippage is avoided by fixing the bottom of the plank to the ground (e.g., using iron spikes). Due to the size of the plank, good coupling with the ground is difficult to achieve, especially on bare rock

or outcrop. Hasbrouck (1977) designed the "Kirk source", which is a steel, hammer-impact, shear-wave source. The coupling to the ground is provided by vanes placed under the plate, which can fit into chipped out trenches Due to some complication in using this technique on bare rocks and hard surfaces, they were replaced by removable spikes (Hasbrouck, 1983). The spikes are easier to fit into natural depression, such as fractures, or by drilling holes into the rock. This source is still used on S_H-wave refraction surveys (Ellefsen et al., 2005). Lighter versions of the Kirk source have been developed, mainly by replacing steel parts by aluminium components (Haines, 2007).

An optimal S_H-source has to satisfy a number of technical criteria in order to be efficient to used and generate useful and interpretable data. Franklin (1979) listed 4 characteristics of the ideal S_H-wave source. The first is that it would maximise the amount of energy available for S_H-waves, and minimise the P- and S_V-waves energy. That can be done using a horizontal cross-line source, the resulting S_H-wave being transmitted in the direction perpendicular to the impulse. Furthermore, the source has to be strongly coupled to the surface. Second, the S_H source should produce two waves of opposite polarity, to ease the detection of the first arrivals (Figure A.2). This can be done by performing two strikes at 180 degrees to each other at the same location. Third, it should be easily transportable in the field, including remote locations inaccessible with a vehicle. Finally, the amount of energy must be controllable and adjustable. A hammer-source is limited in terms of incident energy, but the signal can be amplified by stacking traces from repeated shots, reducing noise and increasing the overall data quality.

The source presented here was designed in the frame of this project to fulfil the previously listed requirements and is based on the Kirk design (Hasbrouck, 1977, 1983; Haines, 2007).

A.2 Source design

The shear source was designed in collaboration with the workshop of the School of Earth Sciences of the University of Bristol. The main body of the source consists in two impact discs in either end, and two 1.2 cm thick and L-shaped aluminium plates (Figure A.3). These

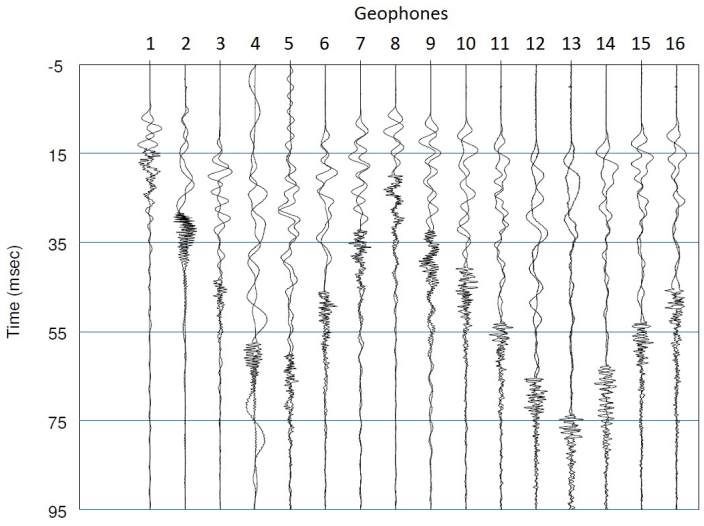

Figure A.2 Raw traces recorded by horizontal geophones during the survey at Lilstock, South West England.

opposite discs allow reverse-polarity shots, which facilitates the identification of the S_H-wave arrivals. In addition, shields made of polyvinyl chloride (PVC) are fixed around the impact discs to provide essential feet protection while hammering.

The source was designed to provide maximum stability of the source on the ground surface, in order to maximise the amount of energy being transferred into the ground. To do so, the user can stand on the plate, increasing the pressure applied on the surface (Figure A.4). In addition, vertical blades and spikes can be screwed on the bottom of the plate to provide further stability and maximise the coupling mechanism, and thus the amount of energy transferred into the ground. Finally, a thin rubber sheet can be fixed under the plate, in order to avoid lateral movement on bare rock and slippery surfaces.

Another important characteristic of the source is that it is easily transportable in the field. The user can use the large handle fixed on the top of the source. The source can also be fixed on a load carrier backpack with an external frame. Alternatively, it can be disassembled in seven different parts: two impacts discs, two aluminium plates, two PVC shields, and one handle.

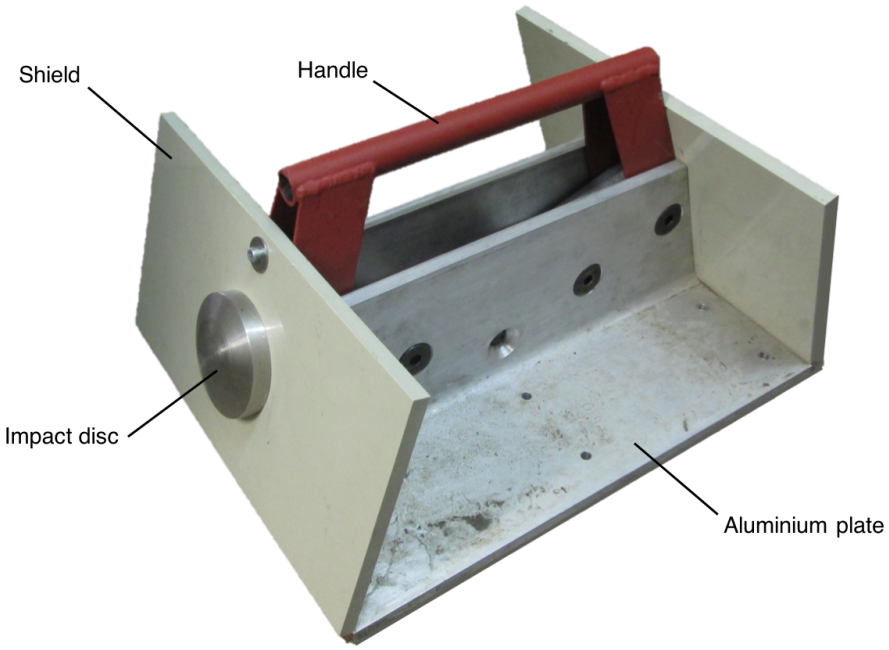

Figure A.3 The Bristol shear-wave source.

Dimensions of the shear-source are indicated on the schematic drawings on Figure A.5.

Figure A.4 Shear source on the field. Photographs courtesy: J.-M. Kendall.

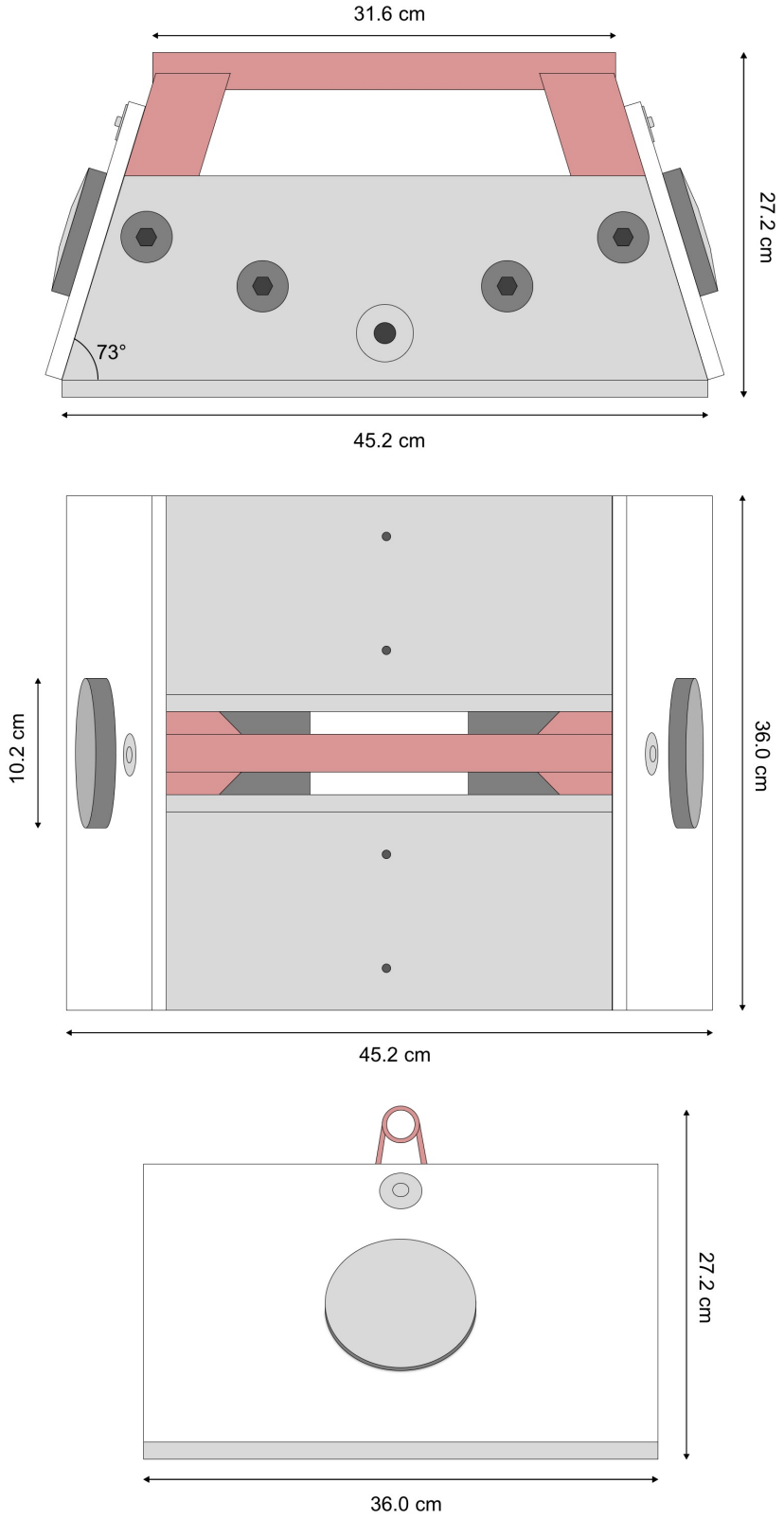

Figure A.5 True to scale sketches of the shear wave source.

APPENDIX B

November 2017 shear wave survey at Lilstock

Abstract

In this section, the configuration of a *S*-wave survey on a rock platform is discussed. It is mainly based on the survey performed at Lilstock on September 2016, as well as another one carried out on the exact same location on November 2017. The aim of this section is to try to describe an ideal *S*-wave survey in the Lilstock settings.

B.1 Introduction

As highlighted by the seismic experiment carried out at Lilstock in September 2016, *P*-wave are easier to work with on the field and when analysing the raw data. They are easier to generate, propagate in every direction without transformation and can be recorded by vertical component geophones, which do not need particular orientation in the horizontal plane. This is particularly true when working on a rock platform, where the geophones need to be glued firmly to the ground and cannot be easily moved or displaced.

On the other hand, *S*-wave require a specific source and geophones with particular orientation.

This is particularly true when doing seismic on bare rock, where geophones cannot simply be driven into the ground.

B.2 November 2017 survey

On 6 November 2017, a *S*-wave survey was carried out at Lilstock, on the outcrop previously investigated (see Chapter 3 and 4). The configuration consists in a quarter circle with 8 branches at regular interval (Figure B.1). Each branch contains three horizontal geophones, oriented perpendicular to the branch, and placed at 5 m interval. Sources are located at the centre of the circle and at the extremity of each branch. Eight pairs of shot are performed (centre + extremity of one branch) with the source oriented perpendicular to the investigated branch. The quarter circle configuration was tested, as a 90 degrees azimuth is representative of the anisotropy controlled by one set of aligned fractures. The aim was to record pure S_H-waves at each branch.

Because of the reduce amount of geophones per angle of propagation and the very localised data, results are not consider reliable enough. Noisy data, such as *S*-waves, require a larger dataset. Foord et al. (2015) manage to generate such large dataset by rotating a straight line of 24 horizontal geophones around a centre point and generating *S*-wave for each angle of rotation. This kind of configuration is hard to set up on a outcrop, as the geophones cannot be displaced so easily.

B.3 Discussion

The quarter circle setup covers a good range of azimuths, but these angles are restricted to one single branch of the star, and do not address the lateral variations that could be present on the outcrop. While with the grid presented in Chapter 4, similar angles of propagation are generated on different locations of the setup.

To tackle these issues, an ideal *S*-wave survey on a rock platform would consist in a grid setup

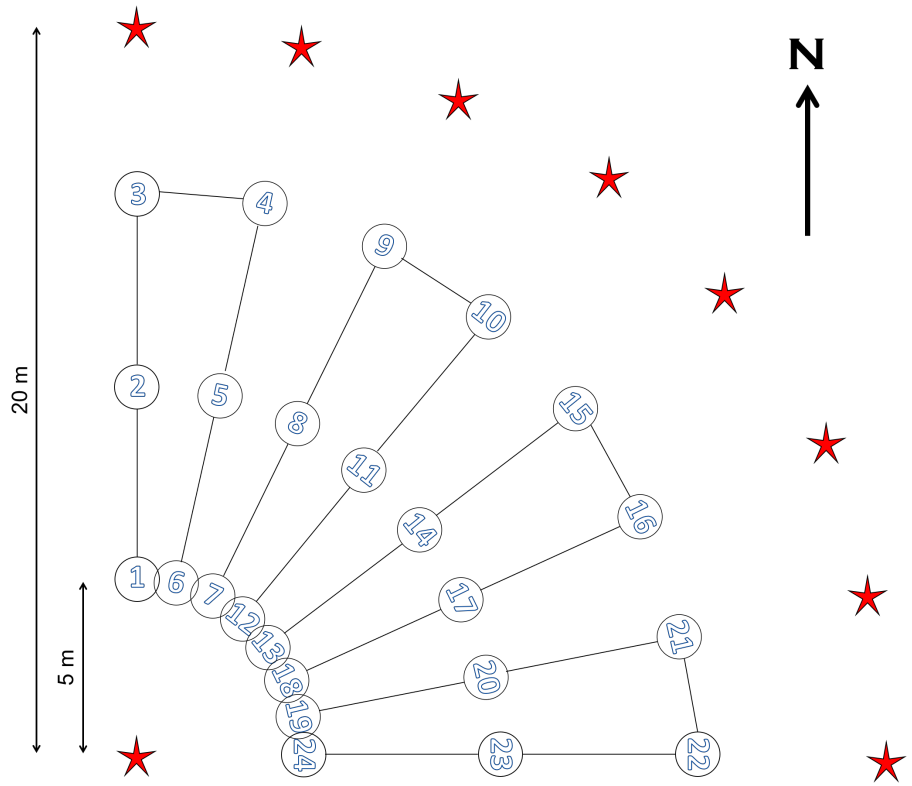

Figure B.1 Configuration of the seismic survey performed at Lilstock on November 2017. Circled numbers mark the position of the horizontal geophones. Red stars indicate the source locations. Note the orientation of the numbers showing the orientation of the horizontal geophones.

with two sets of horizontal geophones, orthogonally oriented. This will ensure a 180 degrees azimuth coverage, and a good lateral representability of the different angles of propagation.

Bibliography

Adelinet, M., Dorbath, C., Calò, M., Dorbath, L., and Le Ravalec, M. (2016). Crack Features and Shear-Wave Splitting Associated with Fracture Extension during Hydraulic Stimulation of the Geothermal Reservoir in Soultz-sous-Forêts. *Oil and Gas Science and Technology*, 71(39):1–22.

Ahmadirouhani, R., Rahimi, B., Karimpour, M. H., Malekzadeh Shafaroudi, A., Afshar Najafi, S., and Pour, A. B. (2017). Fracture mapping of lineaments and recognizing their tectonic significance using SPOT-5 satellite data: A case study from the Bajestan area, Lut Block, east of Iran. *Journal of African Earth Sciences*, 134:600–612.

Aki, K. (1965). Maximum likelihood estimate of b in the formula log N = a-bM and its confidence limits. *University of Tokyo Earthquake Research Institute Bulletin*, 43:237–239.

Al-Harrasi, O. H., Kendall, J. M., and Chapman, M. (2011). Fracture characterization using frequency-dependent shear wave anisotropy analysis of microseismic data. *Geophysical Journal International*, 185(2):1059–1070.

Alehossein, H. and Boland, J. N. (2004). Strength, toughness, damage and fatigue of rock. In *Structural Integrity and Fracture International Conference (SIF'04)*, pages 1–7, Brisbane, Australia. Australia Fracture Group.

Anderson, D. L., Minster, B., and Cole, D. (1974). The Effect of Oriented Cracks on Seismic Velocities DON. *Journal of Geophysical Research*, 79(26):4011–4015.

Angus, D. A., Verdon, J. P., Fisher, Q. J., and Kendall, J.-M. (2009). An audit of dry-core velocity-stress measurements. *Geophysics*, 74(5):193–203.

Anissofira, A. and Latief, F. D. E. (2015). Permeability estimation of crack type and granular type of pore space in a geothermal reservoir using lattice Boltzmann method and Kozeny-Carman relation. In Horne, R. N. and Boyd, T., editors, *World Geothermal Congress 2015*, pages 19–25, Melbourne, Australia. International Geothermal Association.

Awdal, A., Healy, D., and Alsop, G. I. (2016). Fracture patterns and petrophysical properties of carbonates undergoing regional folding: A case study from Kurdistan, N Iraq. *Marine and Petroleum Geology*, 71:149–167.

Backus, G. E. (1962). Long-wave elastic anisotropy produced by horizontal layering. *Journal of Geophysical Research*, 67(11):4427–4440.

Baird, A. F., Kendall, J.-M., and Angus, D. A. (2013a). Frequency-dependent seismic anisotropy due to fractures: Fluid flow versus scattering. *Geophysics*, 78(2):WA111–WA122.

Baird, A. F., Kendall, J. M., Sparks, R. S. J., and Baptie, B. (2015). Transtensional deformation of Montserrat revealed by shear wave splitting. *Earth and Planetary Science Letters*, 425:179–186.

Baird, A. F., Kendall, J. M., Verdon, J. P., Wuestefeld, A., Noble, T. E., Li, Y., Dutko, M., and Fisher, Q. J. (2013b). Monitoring increases in fracture connectivity during hydraulic stimulations from temporal variations in shear wave splitting polarization. *Geophysical Journal International*, 195(2):1120–1131.

Baisch, S., Vörös, R., Weidler, R., and Wyborn, D. (2009). Investigation of fault mechanisms during geothermal reservoir stimulation experiments in the Cooper Basin, Australia. *Bulletin of the Seismological Society of America*, 99(1):148–158.

Bakulin, A. (2003). Intrinsic and layer-induced vertical transverse isotropy. *Geophysics*, 68(5):1708–1713.

Bakulin, A., Grechka, V., and Tsvankin, I. (2000). Estimation of fracture parameters from reflection seismic data - Part I: HTI model due to a single fracture set. *Geophysics*, 65(6):1788–1802.

Bamford, D. and Nunn, K. R. (1979). In situ seismic measurements of crack anisotropy in the carboniferous limestone or Northwest England. *Geophysical Prospecting*, 27(2):322–338.

Barbier, M., Hamon, Y., Callot, J. P., Floquet, M., and Daniel, J. M. (2012). Sedimentary and diagenetic controls on the multiscale fracturing pattern of a carbonate reservoir: The Madison Formation (Sheep Mountain, Wyoming, USA). *Marine and Petroleum Geology*, 29(1):50–67.

Barton, C. A., Zoback, M. D., and Moos, D. (1995). Fluid flow along potentially active faults in crystalline rock. *Geology*, 23(8):683–686.

Barton, N. (2007). Fracture-induced seismic anisotropy when shearing is involved in production from fractured reservoirs. *Journal of Seismic Exploration*, 16(2-4):115–143.

Beach, A., Welbon, A. I., Brockbank, P. J., and McCallum, J. E. (1999). Reservoir damage around faults: Outcrop examples from the Suez rift. *Petroleum Geoscience*, 5(2):109–116.

Belayneh, M. (2003). *Analysis of natural fracture networks in massive and well-bedded carbonate and the impact of these networks on fluid flow in dual porosity modelling.* PhD thesis, Imperial College of Science Technology and Medecine.

Belayneh, M. (2004). Palaeostress orientation inferred from surface morphology of joints on the southern margin of the Bristol Channel Basin, UK. *Geological Society, London, Special Publications*, 231(1):243–255.

Belayneh, M. and Cosgrove, J. W. (2004). Fracture-pattern variations around a major fold and their implications regarding fracture prediction using limited data: an example from the Bristol Channel Basin. In Cosgrove, J. W. and Engelder, T., editors, *The Initiation, Propagation, and Arrest of Joints and Other Fractures.*, number 231, pages 89–102. The Geological Society, London.

Belayneh, M. and Cosgrove, J. W. (2010). Hybrid veins from the southern margin of the Bristol Channel Basin, UK. *Journal of Structural Geology*, 32(2):192–201.

Bianco, F., Scarfi, L., Del Pezzo, E., and Patanè, D. (2006). Shear wave splitting changes associated with the 2001 volcanic eruption on Mt Etna. *Geophysical Journal International*, 167(2):959–967.

Boness, N. L. and Zoback, M. D. (2004). Stress-induced seismic velocity anisotropy and physical properties in the SAFOD Pilot Hole in Parkfield, CA. *Geophysical Research Letters*, 31(15):15–18.

Booth, D. C. and Crampin, S. (1985). Shear-Wave Polarisations on a Curved Wavefront at the free Surface of an Anisotropic Halfspace. *Geoph. Jour. Roy. Astr. Soc.*, 83:31–45.

Bourassa, A. E., Robock, A., Randel, W. J., Deshler, T., Rieger, L. A., Lloyd, N. D., Llewellyn, E. J., and Degenstein, D. A. (2012). Large volcanic aerosol load in the stratosphere linked to Asian monsoon transport. *Science*, 336(6090):78–81.

Bowyer, M. O. N. and Kelly, P. G. (1995). Strain and scaling relationships of faults and veins at Kilve, Somerset. *Geoscience in South-West England*, 8(4):411–415.

Brisbourne, A. (2012). How to store and share geophysical data. *Astronomy and Geophysics*, 53(4):4.19–4.20.

Brooks, M., Trayner, P. M., and Trimble, T. J. (1988). Mesozoic reactivation of Variscan thrusting in the Bristol Channel area, UK. *Journal of the Geological Society*, 145(3):439–444.

Budiansky, B. and O'Connell, R. J. (1976). Elastic moduli of a cracked solid. *International Journal of Solids and Structures*, 12(2):81–97.

Castaing, C., Halawani, M. A., Gervais, F., Chilès, J. P., Genter, A., Bourgine, B., Ouillon, G., Brosse, J. M., Martin, P., Genna, A., and Janjou, D. (1996). Scaling relationships in intraplate fracture systems related to Red Sea rifting. *Tectonophysics*, 261(4):291–314.

Chambers, K., Kendall, J. M., Brandsberg-Dahl, S., and Rueda, J. (2010). Testing the ability of surface arrays to monitor microseismic activity. *Geophysical Prospecting*, 58(5):821–830.

Cheng, C. H. (1993). Crack models for a transversely isotropic medium. *Journal of Geophysical Research*, 98(B1):675–684.

Choi, M.-K., Bobet, A., and Pyrak-Nolte, L. J. (2014). The effect of surface roughness and mixed-mode loading on the stiffness ratio for fractures. *Geophysics*, 79(5):319–331.

Clarisse, L., Coheur, P. F., Theys, N., Hurtmans, D., and Clerbaux, C. (2014). The 2011 Nabro eruption, a SO2 plume height analysis using IASI measurements. *Atmospheric Chemistry and Physics*, 14(6):3095–3111.

Cochran, E. S., Vidale, J. E., and Li, Y.-G. (2003). Near-fault anisotropy following the Hector Mine earthquake. *Journal of Geophysical Research: Solid Earth*, 108(B9):2436–2447.

Crampin, S. (1985). Evaluation of anisotropy by shear-wave splitting. *Geophysics*, 50(1):142–152.

Crampin, S. (1987). Geological and industrial implications of extensive-dilatancy anisotropy. *Nature*, 328:491–496.

Crampin, S. (1994). The Fracture Criticality of Crustal Rocks. *Geophysical Journal International*, 118(2):428–438.

Crampin, S., McGonigle, R., and Bamford, D. (1980). Estimating crack parameters from observations of P-wave velocity anisotropy. *Geophysics*, 45(3):345–360.

Dart, C. J., McClay, K., and Hollings, P. N. (1995). 3D analysis of inverted extensional fault systems, southern Bristol Channel basin, UK. *Geological Society, London, Special Publications*, 88(1):393–413.

De Meersman, K., Kendall, J.-M., and van der Baan, M. (2009). The 1998 Valhall microseismic data set: An integrated study of relocated sources, seismic multiplets, and S-wave splitting. *Geophysics*, 74(5):B183–B195.

Delbecq, F., Downton, J., and Letizia, M. (2013). A Math-free Look at Azimuthal Surface Seismic Techniques. *CSEG Recorder*, (January):20–31.

Dershowitz, W. S. and Einstein, H. H. (1988). Characterizing rock joint geometry with joint system models. *Rock Mechanics and Rock Engineering*, 21(1):21–51.

Donovan, A., Blundy, J., Oppenheimer, C., and Buisman, I. (2018). The 2011 eruption of Nabro volcano, Eritrea: perspectives on magmatic processes from melt inclusions. *Contributions to Mineralogy and Petrology*, 173(1):1–23.

Donovan, R. and Foster, R. (1972). Subaqueous Shrinkage Cracks from the Caithness Flagstone Series (Middle Devonian) of Northeast Scotland. *Journal of Sedimentary*, 42(2):309–317.

Dragoni, M. and Pondrelli, S. (1991). Depth of the brittle-ductile transition in a transcurrent boundary zone. *Pure and Applied Geophysics*, 135(3):447–461.

Duncan, P. M. and Eisner, L. (2010). Reservoir characterization using surface microseismic monitoring. *Geophysics*, 75(5):139–146.

Duxbury, A., White, D., Samson, C., Hall, S. A., Wookey, J., and Kendall, J. M. (2012). Fracture mapping using seismic amplitude variation with offset and azimuth analysis at the Weyburn CO2 storage site. *Geophysics*, 77(6):B295–B306.

Elkibbi, M. and Rial, J. A. (2005). The Geysers geothermal field: Results from shear-wave splitting analysis in a fractured reservoir. *Geophysical Journal International*, 162(3):1024–1035.

Ellefsen, B. K. J., Tuttle, G. J., Williams, J. M., and Lucius, J. E. (2005). S -Wave Refraction Survey of Alluvial Aggregate Scientific Investigations Report 2005-5012. Technical report, United States Geological Survey, Reston, Virginia.

Engelder, T. and Peacock, D. C. P. (2001). Joint development normal to regional compression during flexural-flow folding: The Lilstock buttress anticline, Somerset, England. *Journal of Structural Geology*, 23(2-3):259–277.

Erten, D., Elkibbi, M., and Rial, J. (2001). Shear wave splitting and fracture patterns at the Geysers (California) Geothermal Field. In *Proceedings 26th Workshop on Geothermal Reservoir Engineering, Stanford University, Stanford*, pages 139–147.

Far, M. E., Figueiredo, J. J. S. D., Stewart, R. R., Castagna, J. P., Han, D.-H., and Dyaur, N. (2014). Measurements of seismic anisotropy and fracture compliances in synthetic fractured media. *Geophysical Journal International*, 197(3):1845–1857.

Faulkner, D. R. and Armitage, P. J. (2013). The effect of tectonic environment on permeability development around faults and in the brittle crust. *Earth and Planetary Science Letters*, 375:71–77.

Faulkner, D. R., Mitchell, T. M., Healy, D., and Heap, M. J. (2006). Slip on 'weak' faults by the rotation of regional stress in the fracture damage zone. *Nature*, 444(7121):922–925.

Fee, D., Matoza, R. S., Gee, K. L., Neilsen, T. B., and Ogden, D. E. (2013). Infrasonic crackle and supersonic jet noise from the eruption of Nabro Volcano, Eritrea. *Geophysical Research Letters*, 40(16):4199–4203.

Foord, G., Verdon, J. P., and Kendall, J. M. (2015). Seismic characterization of fracture compliance in the field using P- and S-wave sources. *Geophysical Journal International*, 203(3):1726–1737.

Franciss, F. O. (2010). *Fractured Rock Hydraulics*. CRC Press, London, taylor & f edition.

Franklin, A. (1979). Use of shear waves in seismic refraction surveying. Technical report, U.S. Waterways Experiment Station, Vicksburg, Missourri.

Frazer, L. N. (1990). Dynamic elasticity of microbedded and fractured rocks. *Journal of Geophysical Research*, 95(B4):4821–4831.

Friberg, J., Martinsson, B. G., Sporre, M. K., Andersson, S. M., Brenninkmeijer, C. A., Hermann, M., van Velthoven, P. F., and Zahn, A. (2015). Influence of volcanic eruptions on midlatitude upper tropospheric aerosol and consequences for cirrus clouds. *Earth and Space Science*, 2:285–300.

Frohlich, C. (1993). Teleseismic b Values; Or, Much Ado About 1.0. *Scandinavian Journal of Economics*, 98(B1):631–644.

Fromm, M., Kablick, G., Nedoluha, G., Carboni, E., Grainger, R., Campbell, J., and Lewis, J. (2014). Correcting the record of volcanic stratospheric aerosol impact: Nabro and Sarychev Peak. *Journal of Geophysical Research*, 119(17):10343–10364.

Gardner, G. H. F., Gardner, L. W., and Gregory, A. R. (1974). Formation velocity and density - the diagnostic basics for stratigraphic traps. *Geophysics*, 39(6):770–780.

Gassmann, F. (1951). Uber die elastizitat poroser medien. *Vierteljahresschrift der Naturforschenden Gesellschaft in Zurich*, 96:1–23.

Gelet, R., Loret, B., and Khalili, N. (2013). Thermal recovery from a fractured medium in local thermal non-equilibrium. *International Journal for Numerical and Analytical Methods in Geomechanics*, 37(15):2471–2501.

Gerst, A. and Savage, M. K. (2004). Seismic anisotropy beneath Ruapehu Volcano: A possible eruption forecasting tool. *Science*, 306:1543–1547.

Glen, R. A., Hancock, P. L., and Whittaker, A. (2005). Basin inversion by distributed deformation: The southern margin of the Bristol Channel Basin, England. *Journal of Structural Geology*, 27(12):2113–2134.

Goitom, B. (2017). *The Nabro volcano , tectonic framework and seismic hazard assessment of Eritrea*. PhD thesis, University of Bristol.

Goitom, B., Oppenheimer, C., Hammond, J. O., Grandin, R., Barnie, T., Donovan, A., Ogubazghi, G., Yohannes, E., Kibrom, G., Kendall, J. M., Carn, S. A., Fee, D., Sealing, C., Keir, D., Ayele, A., Blundy, J., Hamlyn, J., Wright, T., and Berhe, S. (2015). First recorded eruption of Nabro volcano, Eritrea, 2011. *Bulletin of Volcanology*, 77(85):1–21.

Gudmundsson, A. (2006). How local stresses control magma-chamber ruptures, dyke injections, and eruptions in composite volcanoes. *Earth-Science Reviews*, 79(1-2):1–31.

Guéguen, Y. and Schubnel, A. (2003). Elastic wave velocities and permeability of cracked rocks. *Tectonophysics*, 370(1-4):163–176.

Gurevich, B., Brajanovski, M., Galvin, R. J., Müller, T. M., and Toms-Stewart, J. (2009). P-wave dispersion and attenuation in fractured and porous reservoirs - Poroelasticity approach. *Geophysical Prospecting*, 57(2):225–237.

Gutenberg, B. and Richter, C. (1942). Earthqauke Magnitude Intensity, Energy and Acceleration. *Bulletin of the Seismological Society of America*, 32(3):163–191.

Haines, S. S. (2007). A Hammer-Impact, Aluminum, Shear-Wave Seismic Source. Open File Report 2007-1406. Technical report, United States Geological Survey, Reston, Virginia.

Hall, S., Kendall, J.-M., and Barkved, O. (2002). Fractured reservoir characterization using P-wave AVOA analysis of 3D OBC data. *The Leading Edge*, 21(8):777–781.

Hall, S. A. (2000). *Rock fractures characterisation and seismic anisotropy: application to ocean bottom seismic data*. PhD thesis, University of Bristol.

Hall, S. A., Kendall, J. M., Maddock, J., and Fisher, Q. (2008). Crack density tensor inversion for analysis of changes in rock frame architecture. *Geophysical Journal International*, 173(2):577–592.

Hamiel, Y. and Baer, G. (2016). Crustal deformation associated with the 2011 eruption of the Nabro volcano, Eritrea. *Tectonophysics*, 691(September):257–262.

Hamlyn, J., Wright, T., Walters, R., Pagli, C., Sansosti, E., Casu, F., Pepe, S., Edmonds, M., McCormick Kilbride, B., Keir, D., Neuberg, J., and Oppenheimer, C. (2018). What causes subsidence following the 2011 eruption at Nabro (Eritrea)? *Progress in Earth and Planetary Science*, 5(31):1–15.

Hamlyn, J. E., Keir, D., Wright, T. J., Neuberg, J. W., Goitom, B., Hammond, J. O., Pagli, C., Oppenheimer, C., Kendall, J. M., and Grandin, R. (2014). Seismicity and subsidence following the 2011 Nabro eruption, Eritrea: Insights into the plumbing system of an off-rift volcano. *Journal of Geophysical Research: Solid Earth*, 119(11):8267–8282.

Hammond, J. O., Hamlyn, J. E., Kendall, J. M., and Goitom, B. (2014). Monitoring the Nabro volcanic eruption (August 2011 - October 2012). Technical report, NERC.

Han, D.-H., Nur, A., and Morgan, D. (1986). Effects of porosity and clay content on wave velocities in sandstones. *Geophysics*, 51(11):2093–2107.

Harbert, W., Daley, T. M., Bromhal, G., Sullivan, C., and Huang, L. (2016). Progress in monitoring strategies for risk reduction in geologic CO2 storage. *International Journal of Greenhouse Gas Control*, 51:260–275.

Hardin, E. L., Cheng, C. H., Paillet, F. L., and Mendelson, J. D. (1987). Fracture characterization by means of attenuation and generation of tube waves in fractured crystalline rock at Mirror Lake, New Hampshire (USA). *Journal of Geophysical Research*, 92(B8):7989–8006.

Harris, S. D., Fisher, Q. J., Karimi-Fard, M., Vaszi, A. Z., and Wu, K. (2005). Modelling the Effects of Faults and Fractures on Fluid Flow in Petroleum Reservoirs. *Transport Phenomena in Porous Media III*, pages 441–476.

Hasbrouck, W. P. (1977). Working drawings of a Kirk shear wave source: U.S. Geological Survey Open-File Report 77-622. Technical report, United States Geological Survey.

Hasbrouck, W. P. (1983). Sketches of a hammer-impact, spiked-base, shear-wave source. Technical report, United States Geological Survey, Golden, Colorado.

Healy, D., Rizzo, R. E., Cornwell, D. G., Farrell, N. J., Watkins, H., Timms, N. E., Gomez-Rivas, E., and Smith, M. (2016). FracPaQ: A MATLAB toolbox for the quantification of fracture patterns. *Journal of Structural Geology*, 95:1–16.

Hebel, L. C., Christensen, E. L., Donath, F. A., Falconer, W. E., Lidofsky, L. J., Moniz, E. J., Moss, T. H., Pigford, R. L., Pigford, T. H., Rochlin, G. I., Silsbee, R. H., Wrenn, M. E., Frauenfelder, H., Cairns, T. L., Panofsky, W. K. H., and Simmons, M. G. (1978). Report to the American Physical Society. by the study group on nuclear fuel cycles and waste management. *Reviews of Modern Physics*, 50(1):S1–S185.

Heidbach, O., Rajabi, M., Cui, X., Fuchs, K., Müller, B., Reinecker, J., Reiter, K., Tingay, M., Wenzel, F., Xie, F., Ziegler, M. O., Zoback, M. L., and Zoback, M. (2018). The World Stress Map database release 2016: Crustal stress pattern across scales. *Tectonophysics*, 744(July):484–498.

Herwanger, J. V., Worthington, M. H., Lubbe, R., Binley, A., and Khazanehdari, J. (2004). A comparison of cross-hole electrical and seismic data in fractured rock. *Geophysical Prospecting*, 52(2):109–121.

Herzog, H. (2009). Carbon Dioxide Capture and Storage. In Helm, D. and Hepburn, C., editors, *The Economics and Politics of Climate Change*, chapter Carbon Dio, pages 263–283. University of Oxford, Oxford, oxford edition.

Hess, H. (1964). Seismic anisotropy in the uppermost mantle under oceans. *Nature*, 203:629–631.

Hesselbo, S. and Jenkyns, H. (1998). Bristish lower jurassic sequence stratigraphy. In de Gracansky, P.-C., Hardenbol, J., Jacquin, T., and Vail, P. R., editors, *Mesozoic and Cenozoic Sequence Stratigraphy of European Basins*, volume 60, pages 561–581. SEPM Special Publication.

Hobday, C. and Worthington, M. H. (2012). Field measurements of normal and shear fracture compliance. *Geophysical Prospecting*, 60(3):488–499.

Hoenig, A. (1978). The behavior of a flat elliptical crack in an anisotropic elastic body. *International Journal of Solids and Structures*, 14(11):925–934.

Holford, S. P. and Turner, J. P. (2005). Reconstructing the Mesozoic,ÄìCenozoic exhumation history of the Irish Sea basin system using apatite fission track analysis and vitrinite reflectance data. In Doré, A. and Vining, B., editors, *Petroleum Geology: North-West Europeand Global Perspectives - Proceedings of the 6th Petroleum Geology Conference*, pages 1095–1107, London. Geological Society.

Hooker, J. N., Gale, J. F., Gomez, L. A., Laubach, S. E., Marrett, R., and Reed, R. M. (2009). Aperture-size scaling variations in a low-strain opening-mode fracture set, Cozzette Sandstone, Colorado. *Journal of Structural Geology*, 31(7):707–718.

Hornby, B. (1994). *The elastic properties of shales*. PhD thesis, Cambridge University.

Hsu, C.-J. and Schoenberg, M. (1993). Elastic waves through a simulated fractured medium. *Geophysics*, 58(7):964–977.

Huang, S., Zhang, Y., Zheng, X., Zhu, Q., Shao, G., Cao, Y., Chen, X., Yang, Z., and Bai, X. (2017). Types and characteristics of carbonate reservoirs and their implication on hydrocarbon exploration: A case study from the eastern Tarim Basin, NW China. *Journal of Natural Gas Geoscience*, 2(1):73–79.

Hudson, J. A. (1980). Overall properties of a cracked solid. *Math Proc Camb Philos Soc*, 88(1952):371–384.

Hudson, J. A. (1981). Wave speeds and attenuation of elastic waves in material containing cracks. *Geophysical Journal of the Royal Astronomical Society*, 64:133–150.

Hudson, J. A. and Liu, E. (1999). Effective elastic properties of heavily faulted structures. *Geophysics*, 64(2):479–485.

Hudson, J. A., Liu, E., and Crampin, S. (1996). The mechanical properties of materials with interconnected cracks and pores. *Geophysical Journal International*, 124:105–112.

Hudson, J. A., Pointer, T., and Liu, E. (2001). Effective-medium theories for fluid-saturated materials with aligned cracks. *Geophysical Prospecting*, 49(5):509–522.

Ibáñez, J. M., De Angelis, S., Díaz-Moreno, A., Hernández, P., Alguacil, G., Posadas, A., and Pérez, N. (2012). Insights into the 2011-2012 submarine eruption off the coast of El Hierro (Canary Islands, Spain) from statistical analyses of earthquake activity. *Geophysical Journal International*, 191(2):659–670.

Illsley-Kemp, F., Savage, M. K., Keir, D., Hirschberg, H. P., Bull, J. M., Gernon, T. M., Hammond, J. O., Kendall, J. M., Ayele, A., and Goitom, B. (2017). Extension and stress during continental breakup: Seismic anisotropy of the crust in Northern Afar. *Earth and Planetary Science Letters*, 477:41–51.

Iñigo, J. F., Laubach, S. E., and Hooker, J. N. (2012). Fracture abundance and patterns in the Subandean fold and thrust belt, Devonian Huamampampa Formation petroleum reservoirs and outcrops, Argentina and Bolivia. *Marine and Petroleum Geology*, 35(1):201–218.

Inks, T. L., Engelder, T., Jenner, E., Golob, B., Hocum, J. S., and O'Brien, D. G. (2015). Marcellus fracture characterization using P-wave azimuthal velocity attributes: Comparison with production and outcrop data. *Interpretation*, 3(3):SU1–SU15.

Jafari, M. (2008). The distribution of b-value in different seismic provinces of Iran. In *14th World Conference on Earthquake Engineering*, Beijing, China.

Jay, J., Pritchard, M. E., West, M. E., Christensen, D., Haney, M., Minaya, E., Sunagua, M., McNutt, S. R., and Zabala, M. (2012). Shallow seismicity, triggered seismicity, and ambient noise tomography at the long-dormant Uturuncu Volcano, Bolivia. *Bulletin of Volcanology*, 74(4):817–837.

Johansen, T. A., Ruud, B. O., and Jakobsen, M. (2004). Effect of grain scale alignment on seismic anisotropy and reflectivity of shales. *Geophysical Prospecting*, 52(2):133–149.

Johnson, J. H. and Poland, M. P. (2013). Seismic detection of increased degassing before Kilauea's 2008 summit explosion. *Nature Communications*, 4:1666–1668.

Julian, B. R., Foulger, G. R., Monastero, F. C., and Bjornstad, S. (2010). Imaging hydraulic fractures in a geothermal reservoir. *Geophysical Research Letters*, 37(7):1–5.

Jupe, A. J., Jones, R. H., Wilson, S. A., and Cowles, J. F. (2003). Microseismic monitoring of geomechanical reservoir processes and fracture-dominated fluid flow. *Geological Society, London, Special Publications*, 209(1):77–86.

Kamerling, P. (1979). The geology and hydrocarbon habitat of the bristol Channel basin. *Journal of Petroleum Geology*, 2(1):75–93.

Keats, B. S., Johnson, J. H., and Savage, M. K. (2011). The Erua earthquake cluster and seismic anisotropy in the Ruapehu region, New Zealand. *Geophysical Research Letters*, 38(16):1–6.

Keir, D., Bastow, I. D., Whaler, K. A., Daly, E., Cornwell, D. G., and Hautot, S. (2009). Lower crustal earthquakes near the Ethiopian rift induced by magmatic processes. *Geochemistry, Geophysics, Geosystems*, 10(6):1–10.

Kendall, J.-M., Fisher, Q. J., Crump, S. C., Maddock, J., Carter, A., Hall, S. A., Wookey, J., Valcke, S. L. A., Casey, M., Lloyd, G., and Ismail, W. B. (2007). Seismic anisotropy as an indicator of reservoir quality in siliciclastic rocks. *Geological Society, London, Special Publications*, 292(1):123–136.

Kendall, J.-M., Pilidou, S., Keir, D., Bastow, I., Stuart, G., and Ayele, A. (2006). Mantle upwellings, melt migration and the rifting of Africa: insights from seismic anisotropy. *Geological Society, London, Special Publications*, 259(1):55–72.

Kendall, J.-M., Verdon, J. P., Baird, A., Wuestefeld, A., and Rutledge, J. T. (2012). Microseismic Monitoring of Fracture Networks During Hydraulic Stimulation: Beyond Event Locations. In *Society of Petroleum Engineers*, Vienna.

Kendall, J.-m., Verdon, J. P., and Baird, A. F. (2014). Evaluating fracture-induced anisotropy using borehole microseismic data. *CSEG Recorder*, 39(2):56–63.

Khelifa, C., Zeddouri, A., and Djabes, F. (2014). Influence of natural fractures on oil production of unconventional reservoirs. *Energy Procedia*, 50:360–367.

King, M. S., Myer, L. R., and Rezowalli, J. J. (1986). Experimental studies of elastic-wave propagation in a columnar-jointed rock mass. *Geophysical Prospecting*, 34:1185–1199.

Koster, J. W. and Harry, D. L. (2005). Effects of Water Saturation on a Resistivity Survey of an Unconfined Fluvial Aquifer in Columbus , MS. In *Hydrology days*, number 970, pages 111–120.

Lamur, A., Kendrick, J. E., Eggertsson, G. H., Wall, R. J., Ashworth, J. D., and Lavallée, Y. (2017). The permeability of fractured rocks in pressurised volcanic and geothermal systems. *Scientific Reports*, 7(1):1–9.

Latief, F. D. E. and Feranie, S. (2014). Three-dimensional visualization and characterization of cracks in geothermal reservoir rock using image analysis of reconstructed micro CT images: A preliminary study. In *AIP Conference Proceedings*, pages 120–123.

Le Garzic, E., de L'Hamaide, T., Diraison, M., Géraud, Y., Sausse, J., Nancy, M. D., and Lorr, U. D. (2011). Scaling and geometric properties of extensional fracture systems in the proterozoic basement of Yemen. Tectonic interpretation and fluid flow implications. *Journal of Structural Geology*, 33(4):519–536.

Le Goc, R., Darcel, C., and Davy, P. (2017). Advanced DFN Models from Multi-Support Data for Underground Facilities. *Procedia Engineering*, 191:1015–1022.

Lehto, H. L., Roman, D. C., and Moran, S. C. (2010). Temporal changes in stress preceding the 2004-2008 eruption of Mount St. Helens, Washington. *Journal of Volcanology and Geothermal Research*, 198(1-2):129–142.

Lisjak, A., Figi, D., and Grasselli, G. (2014). Fracture development around deep underground excavations: Insights from FDEM modelling. *Journal of Rock Mechanics and Geotechnical Engineering*, 6(6):493–505.

Liu, E. and Martinez, A. (2013). *Seismic Fracture Characterization: Concepts and Practical Applications*. EAGE Publications bv, Houten, The Netherlands.

Liu, Y., Crampin, S., and Main, I. (1997). Shear-wave anisotropy: Spatial and temporal variations in time delays at Parkfield, Central California. *Geophysical Journal International*, 130(3):771–785.

Liu, Y., Pellikka, P. K., Li, H., and Fang, X. (2019). Detection of the dispersion and residence of volcanic SO2 and sulfate aerosol from Nabro in 2011. *Atmospheric Environment*, 197:34–44.

Liu, Y., Zhang, H., Thurber, C., and Roecker, S. (2008). Shear wave anisotropy in the crust around the San Andreas fault near Parkfield: Spatial and temporal analysis. *Geophysical Journal International*, 172(3):957–970.

Lloyd, G. E. and Kendall, J. M. (2008). Petrofabric-derived seismic properties of a mylonitic quartz simple shear zone: implications for seismic reflection profiling. *Geological Society, London, Special Publications*, 240(1):75–94.

Lomax, D. R., De la Salle, P., Massare, J. A., and Gallois, R. (2018). A giant Late Triassic ichthyosaur from the UK and a reinterpretation of the Aust Cliff dinosaurian bones. *PLoS ONE*, 13(4):1–16.

Long, M. D. and Silver, P. G. (2009). Shear wave splitting and mantle anisotropy: Measurements, interpretations, and new directions. *Surveys in Geophysics*, 30(4-5):407–461.

Lou, M. and Rial, J. A. (1997). Characterization of geothermal reservoir crack patterns using shear-wave splitting. *Geophysics*, 62(2):487–494.

Lubbe, R., Sothcott, J., Worthington, M. H., and Mccann, C. (2008). Laboratory estimates of normal and shear fracture compliance. *Geophysical Prospecting*, 56:239–247.

Lubbe, R. and Worthington, M. H. (2006). A field investigation of fracture compliance. *Geophysical Prospecting*, 54(3):319–331.

Lynn, H. and Thomsen, L. (1990). Reflection Shear-Wave Data Along the Principal Axes of Aximuthal Anisotropy. *Geophysics*, 55(2):147–156.

Macbeth, C. and Schuett, H. (2007). The stress dependent elastic properties of thermally induced microfractures in aeolian Rotliegend sandstone. *Geophysical Prospecting*, 55:323–332.

Mack, T. J. and Degnan, J. R. (2003). Geophysical Characterization of Fractured Bedrock at Site 8 , Former Pease Air Force Base , Newington , New Hampshire. Technical report, U.S. Geological Survey, Pembroke, New Hampshire.

Maher, S. and Kendall, J.-M. (2018). Crustal anisotropy and state of stress at Uturuncu Volcano , Bolivia , from shear-wave splitting measurements and magnitude ‚Äì frequency distributions in seismicity. *Earth and Planetary Science Letters*, 495:38–49.

Mansour, K., Omar, K., Ali, K., and Abdel Zaher, M. (2018). Geophysical characterization of the role of fault and fracture systems for recharging groundwater aquifers from surface water of Lake Nasser. *NRIAG Journal of Astronomy and Geophysics*, 7:99–106.

Manzocchi, T. (2002). The connectivity of two-dimensional networks of spatially correlated fractures. *Water Resources Research*, 38(9):1–20.

Martel, S. J. (2004). Mechanics of landslide initiation as a shear fracture phenomenon. *Marine Geology*, 203(3-4):319–339.

Mateshvili, N., Fussen, D., Mateshvili, G., Mateshvili, I., Vanhellemont, F., Kyrola, E., Tukiainen, S., Kujanpää, J., Bingen, C., Robert, C., Tétard, C., and Dekemper, E. (2013). Nabro volcano aerosol in the stratosphere over Georgia, South Caucasus from ground-based spectrometry of twilight sky brightness. *Atmospheric Measurement Techniques*, 6(10):2563–2576.

Matoza, R. S. and Fee, D. (2018). The Inaudible Rumble of Volcanic Eruptions. *Acoustics Today*, 14(1):17–25.

Matsuyama, K., Yamada, M., and Ohtsu, M. (2010). On-site measurement of delamination and surface crack in concrete structure by visualized NDT. *Construction and Building Materials*, 24(12):2381–2387.

Matthäi, S. K. and Belayneh, M. (2004). Fluid flow partitioning between fractures and a permeable rock matrix. *Geophysical Research Letters*, 31(7):1–5.

Mauldon, M., Dunne, W. M., and Rohrbaugh, M. B. (2001). Circular scanlines and circular windows: New tools for characterizing the geometry of fracture traces. *Journal of Structural Geology*, 23(2-3):247–258.

Maxwell, S. C. (2010). Micoseismic: Growth born from success. *The Leading Edge*, 29(3):338–343.

Maxwell, S. C. and Urbancic, T. I. (2001). The role of passive microseismic monitoring in the instrumented oil field. *The Leading Edge*, 20(6):636–639.

Mignan, A. and Woessner, J. (2012). Estimating the magnitude of completeness for earthquake catalogs. *Community Online Resource for Statistical Seismicity Analysis,*, Available.

Miller, V. (2002). Changes in Seismic Anisotropy After Volcanic Eruptions: Evidence from Mount Ruapehu. *Science*, 293(5538):2231–2233.

Mitchell, T. M. and Faulkner, D. R. (2009). The nature and origin of off-fault damage surrounding strike-slip fault zones with a wide range of displacements: A field study from the Atacama fault system, northern Chile. *Journal of Structural Geology*, 31(8):802–816.

Möllhoff, M., Bean, C. J., and Meredith, P. G. (2010). Rock fracture compliance derived from time delays of elastic waves. *Geophysical Prospecting*, 58(6):1111–1122.

Murru, M., Montuori, C., Wyss, M., and Privitera, E. (1999). The locations of magma chambers at Mt. Etna, Italy, mapped by b-values. *Geophysical Research Letters*, 26(16):2553–2556.

Myer, L. R., Hopkins, D., Peterson, J., and Cook, N. (1995). Seismic wave propagation across multiple fracture. In Myer, L. R., Cook, N. G., Goodman, R., and Tsang, C., editors, *Fractured and Jointed Rock Masses*, pages 105–110, Rotterdam. Balkema.

Nascimento Da Silva, C. C., De Medeiros, W. E., De Sá, E. F. J., and Neto, P. X. (2004). Resistivity and ground-penetrating radar images of fractures in a crystalline aquifer: A case study in Caiçara farm - NE Brazil. *Journal of Applied Geophysics*, 56(4):295–307.

Nemčok, M., Gayer, R., and Miliorizos, M. (1995). Structural analysis of the inverted Bristol Channel Basin: implications for the geometry and timing of fracture porosity. *Geological Society, London, Special Publications*, 88(1):355–392.

Noh, Y. M., Shin, D. H., and Müller, D. (2017). Variation of the vertical distribution of Nabro volcano aerosol layers in the stratosphere observed by LIDAR. *Atmospheric Environment*, 154:1–8.

Nowacki, A., Wilks, M., Kendall, J. M., Biggs, J., and Ayele, A. (2018). Characterising hydrothermal fluid pathways beneath Aluto volcano, Main Ethiopian Rift, using shear wave splitting. *Journal of Volcanology and Geothermal Research*, 356:331–341.

Nowroozi, A. A. and Ahmadi, G. (1986). Analysis of Earthquake Risk in Iran based on seismotectonic provinces. *Tectonophysics*, 122:89–114.

Nunn, K., Barker, R., and Bamford, D. (1983). In situ seismic and electrical measurements of fracture anisotropy in the Lincolnshire Chalk. *Quarterly Journal of Engineering Geology and Hydrogeology*, 16:187–195.

Odling, N. E. (1997). Scaling and connectivity of joint systems in sandstones from western Norway. *Journal of Structural Geology*, 19(10):1257–1271.

Odling, N. E., Gillespie, P., Bourgine, B., Castaing, C., Chiles, J. P., Christensen, N. P., Fillion, E., Genter, A., Olsen, C., Thrane, L., Trice, R., Aarseth, E., Walsh, J. J., and Watterson, J. (1999). Variations in fracture system geometry and their implications for fluid flow in fractures hydrocarbon reservoirs. *Petroleum Geoscience*, 5(4):373–384.

Odom, I. E. (1984). Smectite clay Minerals: Properties and Uses. *Philosophical Transactions of the Royal Society of London A*, 311:391–409.

Ogubazghi, G. and Goitom, B. (2014). Relocation of the 31 March 2011 Earthquake in the Nabro Volcanic Range of Southern Eritrea. *Eritrean Jouranl of Science and Engineering*, 1(1):93–102.

Ohno, K. and Ohtsu, M. (2010). Crack classification in concrete based on acoustic emission. *Construction and Building Materials*, 24(12):2339–2346.

Paillet, F. and Kapucu, K. (1989). Fracture characterization and fracture-permeability estimates from geophysical logs in the Mirror Lake watershed, New Hampshire. Technical report, U.S. Geological Survey, Lakewood, Colorado.

Parsons, T. and Thompson, G. (1991). Role of magma overpressure in suppressing earthquakes and topography: Worldwide examples. *Science*, 253:1399–1402.

Peacock, D. C., Nixon, C. W., Rotevatn, A., Sanderson, D. J., and Zuluaga, L. F. (2016). Glossary of fault and other fracture networks. *Journal of Structural Geology*, 92:12–29.

Peacock, D. C. P. (2004). Differences between veins and joints using the example of the Jurassic limestones of Somerset. In Cosgrove, J. W. and Engelder, T., editors, *The Initiation, Propagation, and Arrest of Joints and Other Fractures.*, number 3, pages 209–221. Geological Society of London, London, geological edition.

Peacock, D. C. P. and Mann, A. (2005). Evaluation of the controls on fracturing in reservoir rocks. *Journal of Petroleum Geology*, 28(4):385–396.

Peacock, D. C. P. and Sanderson, D. J. (1999). Deformation history and basin-controlling faults in the Mesozoic sedimentary rocks of the Somerset coast. *Proceedings of the Geologists' Association*, 110, Part(1):41–52.

Peacock, D. C. P. and Sanderson, D. J. (2018). Structural analyses and fracture network characterisation: Seven pillars of wisdom. *Earth-Science Reviews*.

Perrin, C., Manighetti, I., Ampuero, J.-P., Cappa, F., and Gaydemer, Y. (2016). Location of largest earthquake slip and fast rupture controlled by along-strike change in fault structural maturity due to fault growth. *Journal of Geophysical Research: Solid Earth*, 121:3666–3685.

Pinto, J. P., Turco, R. P., and Toon, O. B. (1989). Self-limiting physical and chemical effects in volcanic eruption clouds. *Journal of Geophysical Research*, 94(D8):11165–11174.

Pointer, T., Liu, E., and Hudson, J. A. (2000). Seismic wave propagation in cracked porous media. *Geophysical Journal International*, 142(1):199–231.

Pollard, D. D. and Aydin, A. (1988). Progress in understanding jointing over the past century. *Geological Society Of America Bulletin*, 100:1181–1204.

Pollard, D. D. and Fletcher, R. C. (2005). *Fundamentals of Structural Geology*. Cambridge University Press, Cambridge.

Price, N. (1966). *Fault and Joint Development in Brittle and Semi-brittle Rock.* Oxford, pergamon p edition.

Price, N. and Cosgrove, J. W. (1990). *Analysis of geological structures.* Cambridge University Press, Cambridge.

Priest, S. D. and Hudson, J. A. (1981). Estimation of discontinuity spacing and trace length using scanline surveys. *International Journal of Rock Mechanics and Mining Sciences and*, 18(3):183–197.

Prioul, R., Donald, A., Koepsell, R., Marzouki, Z. E., and Bratton, T. (2007). Forward modeling of fracture-induced sonic anisotropy using a combination of borehole image and sonic logs. *Geophysics*, 72(4):E135–E147.

Prioul, R., Jocker, J., and Montaggioni, P. (2008). Fracture compliance estimation using a combination of image and sonic logs. In *SEG Annual Meeting*, pages 314–318, Las Vegas.

Procter, A. and Sanderson, D. J. (2017). Spatial and layer-controlled variability in fracture networks. *Journal of Structural Geology*, 108:52–65.

Pruess, K. and Doughty, C. (2010). Thermal single-well injection-withdrawal tracer tests for determining fracture-matrix heat transfer area. *35th Workshop on Geothermal Reservoir Engineering*, pages 351–359.

Pyrak-Nolte, L. J., Myer, L. R., and Cook, N. G. W. (1990). Transmission of seismic waves across single natural fractures. *Journal of Geophysical Research*, 95(B6):8617–8638.

Rathore, J. S. and Fjaer, E. (1994). P- and S-wave anisotropy of a synthetic sandstone with controlled crack geometryl. *Geophysical Prospecting*, 43:711–728.

Rawnsley, K. D., Peacock, D. C. P., Rives, T., and Petit, J.-P. (1998). Joints in the Mesozoic sediments around the Bristol Channel Basin. *Journal of Structural Geology*, 20(12):1641–1661.

Renshaw, C. E. (1997). Mechanical controls on the spatial density of opening-mode fracture networks. *Geology*, 25(10):923–926.

Rial, J. A., Elkibbi, M., and Yang, M. (2005). Shear-wave splitting as a tool for the characterization of geothermal fractured reservoirs: Lessons learned. *Geothermics*, 34(3):365–385.

Rives, T., Rawnsley, K. D., and Petit, J.-P. (1994). Analogue simulation of natural orthogonal joint set formation in brittle varnish. *Journal of Structural Geology*, 16(3):419–429.

Roberts, N. S., Bell, A. F., and Main, I. G. (2015). Are volcanic seismic b-values high, and if so when? *Journal of Volcanology and Geothermal Research*, 308:127–141.

Robock, A. (2000). Volcanic eruptions and climate. *Reviews of Geophysics*, 38(2):191–219.

Rohrbaugh, J. B., Dunne, W. M., and Mauldon, M. (2002). Estimating fracture trace intensity, density, and mean length using circular scan lines and windows. *AAPG Bulletin*, 86(12):2089–2104.

Roman, D. C. (2005). Numerical models of volcanotectonic earthquake triggering on non-ideally oriented faults. *Geophysical Research Letters*, 32(2):1–4.

Roman, D. C. and Cashman, K. V. (2006). The origin of volcano-tectonic earthquake swarms. *Geology*, 34(6):457–460.

Roman, D. C., Moran, S. C., Power, J. A., and Cashman, K. V. (2004). Temporal and Spatial Variation of Local Stress Fields before and after the 1992 Eruptions of Crater Peak Vent, Mount Spurr Volcano, Alaska. *Bulletin of the Seismological Society of America*, 94(6):2366–2379.

Rydelek, P. and Sacks, I. S. (1989). Testing the completeness of earthquake catalogues and the hypothesis of self-similarity. *Nature*, 337(19):1989.

Sanderson, D. J. and Nixon, C. W. (2015). The use of topology in fracture network characterization. *Journal of Structural Geology*, 72:55–66.

Sanderson, D. J. and Nixon, C. W. (2018). Topology, connectivity and percolation in fracture networks. *Journal of Structural Geology*, 115:167–177.

Santer, B. D., Solomon, S., Bonfils, C., Zelinka, M. D., Painter, J. F., Beltran, F., Fyfe, J. C., Johannesson, G., Mears, C., Ridley, D. A., Vernier, J. P., and Wentz, F. J. (2015). Observed multivariable signals of late 20th and early 21st century volcanic activity. *Geophysical Research Letters*, 42(2):500–509.

Savage, M. (1999). Seismic anisotropy and mantle deformation: What have we learned from shear wave splitting? *Reviews of Geophysics*, 37(1):65–106.

Sawamura, P., Vernier, J. P., Barnes, J. E., Berkoff, T. A., Welton, E. J., Alados-Arboledas, L., Navas-Guzmán, F., Pappalardo, G., Mona, L., Madonna, F., Lange, D., Sicard, M., Godin-Beekmann, S., Payen, G., Wang, Z., Hu, S., Tripathi, S. N., Cordoba-Jabonero, C., and Hoff, R. M. (2012). Stratospheric AOD after the 2011 eruption of Nabro volcano measured by lidars over the Northern Hemisphere. *Environmental Research Letters*, 7(3):1–9.

Sayers, C. M. (1999). Stress-dependent seismic anisotropy of shales. *Geophysics*, 64(1):93–98.

Sayers, C. M. and den Boer, L. D. (2012). Characterizing production-induced anisotropy of fractured reservoirs having multiple fracture sets. *Geophysical Prospecting*, 60(5):919–939.

Sayers, C. M. and Han, D.-h. (2002). The effect of pore fluid on the stress-dependent elastic wave velocities in sandstones. In *SEG Int'l Exposition and 72nd Annual Meeting*, pages 11–14, Salt Lake City, Utah.

Sayers, C. M. and Kachanov, M. (1995). Microcrack-induced elastic wave anisotropy of brittle rocks. *Journal of Geophysical Research*, 100(B3):4149–4156.

Sayers, C. M., Taleghani, A. D., and Adachi, J. (2009). The effect of mineralization on the ratio of normal to tangential compliance of fractures. *Geophysical Prospecting*, 57(3):439–446.

Schlaphorst, D., Kendall, J. M., Baptie, B., Latchman, J. L., and Tait, S. (2017). Gaps, tears and seismic anisotropy around the subducting slabs of the Antilles. *Tectonophysics*, 698:65–78.

Schleicher, A. M., Van Der Pluijm, B. A., Solum, J. G., and Warr, L. N. (2006). Origin and significance of clay-coated fractures in mudrock fragments of the SAFOD borehole (Parkfield, California). *Geophysical Research Letters*, 33:1–5.

Schoenberg, M. and Douma, J. (1988). Elastic wave propagation in media with parallel fractures and aligned cracks. *Geophysical Prospecting*, 36:571–590.

Schoenberg, M. and Sayers, C. M. (1995). Seismic anisotropy of fractured rock. *Seismic and acoustic velocities in reservoir rocks*, 19(1):161–168.

Scholz, C. H. (2015). On the stress dependence of the earthquake b value. *Geophysical Research Letters*, 42(5):1399–1402.

Shin, D., Müller, D., Lee, K., Shin, S., Kim, Y. J., Song, C. K., and Noh, Y. M. (2015). Lidar observations of Nabro volcano aerosol layers in the stratosphere over Gwangju, Korea. *Atmospheric Chemistry and Physics Discussions*, 15(1):1171–1191.

Silver, P. G. and Chan, W. W. (1991). Shear Wave Splitting and Sub continental Mantle Deformation. *Journal of Geophysical Research*, 96:429–454.

Simms, M. J., Chidlaw, M., Morton, N., and Page, K. N. (2004). British Lower Jurassic stratigraphy: an introduction. *Geological Conservation Review Series*, 30(30):458pp.

Singh, U. (2013). Carbon capture and storage: An effective way to mitigate global warming. *Current Science*, 105(7):914–922.

Stork, A. L., Verdon, J. P., and Kendall, J. M. (2015). The microseismic response at the In Salah Carbon Capture and Storage (CCS) site. *International Journal of Greenhouse Gas Control*, 32:159–171.

Szalai, S., Szokoli, K., Novák, A., Tóth, Á., Metwaly, M., and Prácser, E. (2014). Fracture network characterisation of a landslide by electrical resistivity tomography. *Natural Hazards and Earth System Sciences Discussions*, 2(6):3965–4010.

Tandon, G. P. and Weng, G. J. (1984). The effect of aspect ratio of inclusions on the elastic properties of unidirectionally aligned composites. *Polymer composites*, 5(4):327–333.

Tang, C., Rial, J. A., and Lees, J. M. (2005). Shear-wave splitting: A diagnostic tool to monitor fluid pressure in geothermal fields. *Geophysical Research Letters*, 32(21):1–3.

Tang, C., Rial, J. A., and Lees, J. M. (2015). Observations and Analyses of Shear-Wave Splitting in the Geothermal Field at Hengill , Iceland. *Seismological Research Letters*, 86(April):1–7.

Teanby, N., Kendall, J.-M., Jones, R. H., and Barkved, O. (2004a). Stress-induced temporal variations in seismic anisotropy observed in microseismic data. *Geophysical Journal International*, 156(3):459–466.

Teanby, N., Kendall, J.-M., and van der Baan, M. (2004b). Automation of shear-wave splitting measurements using cluster analysis. *Bulliten of the Seismological Society of America*, 94(2):453–463.

Tembe, S., Lockner, D. A., and Wong, T. F. (2010). Effect of clay content and mineralogy on frictional sliding behavior of simulated gouges: Binary and ternary mixtures of quartz, illite, and montmorillonite. *Journal of Geophysical Research: Solid Earth*, 115:1–22.

Testa, S. (2017). Historic Development of Well Stimulation and Hydraulic Fracturing Technologies. In *AAPG Pacific Section and Rocky Mountain Section Joint Meeting*, number 60053, pages 1–46, Las Vegas. Testa Environmental Corporation.

Theys, N., Campion, R., Clarisse, L., Brenot, H., van Gent, J., Dils, B., Corradini, S., Merucci, L., Coheur, P.-F., Van Roozendael, M., Hurtmans, D., Clerbaux, C., Tait, S., and Ferrucci, F. (2013). Volcanic SO2 fluxes derived from satellite data: a survey using OMI, GOME-2, IASI and MODIS. *Atmospheric Chemistry and Physics*, 13(12):5945–5968.

Thomas, C. and Kendall, J. M. (2002). The lowermost mantle beneath northern Asia,ÄîII. Evidence for lower-mantle anisotropy. *Geophysical Journal International*, 151:296–308.

Thomsen, L. (1986). Weak elastic anisotropy. *Geophysics*, 51(10):1954–1966.

Thomsen, L. (1995). Elastic anisotropy due to aligned cracks in porous rock. *Geophysical Prospecting*, 43:805–829.

Tryggvason, A., Rögnvaldsson, S. T., and Flóvenz, Ó. G. (2002). Three-dimensional imaging of the P- and S-wave velocity structure and earthquake locations beneath Southwest Iceland. *Geophysical Journal International*, 151(3):848–866.

Tveite, H. (2015). The QGIS Line Direction Histogram Plugin.

Uchino, O., Sakai, T., Nagai, T., Nakamae, K., Morino, I., Arai, K., Okumura, H., Takubo, S., Kawasaki, T., Mano, Y., Matsunaga, T., and Yokota, T. (2012). On recent (2008-2012) stratospheric aerosols observed by lidar over Japan. *Atmospheric Chemistry and Physics*, 12(24):11975–11984.

Uncles, R. J. and Cox, C. S. (1981). A Numerical Simulation of the Vertical and Horizontal M2 Tide in the Bristol Channel and Comparisons with Observed Data. *Limnology and Oceanography*, 26(3):571–577.

Valcke, S. L. A., Casey, M., Lloyd, G. E., Kendall, J. M., and Fisher, Q. J. (2006). Lattice preferred orientation and seismic anisotropy in sedimentary rocks. *Geophysical Journal International*, 166(2):652–666.

van der Pluijm, B. A. and Marshak, S. (2004). *Earth structure. An introduction to structural geology and tectonics*. New York, w.w. norto edition.

Van Hoorn, B. (1987). The south Celtic Sea/Bristol Channel Basin: origin, deformation and inversion history. *Tectonophysics*, 137(1-4):309–334.

Verdon, J. (2010). *Microseismic monitoring and geomechanical modeling of CO2 storage in subsurface reservoirs*. PhD thesis, University of Bristol.

Verdon, J. P., Angus, D. A., Kendall, J. M., and Hall, S. A. (2008). The effect of microstructure and nonlinear stress on anisotropic seismic velocities. *Geophysics*, 73(4):D41–D51.

Verdon, J. P. and Kendall, J. M. (2011). Detection of multiple fracture sets using observations of shear-wave splitting in microseismic data. *Geophysical Prospecting*, 59(4):593–608.

Verdon, J. P., Kendall, J.-M., Stork, A. L., Chadwick, R. A., White, D. J., and Bissell, R. C. (2013). Comparison of geomechanical deformation induced by megatonne-scale CO2 storage at Sleipner, Weyburn, and In Salah. *Proceedings of the National Academy of Sciences of the United States of America*, 110(30):E2762–2671.

Verdon, J. P., Kendall, J. M., White, D. J., and Angus, D. A. (2011). Linking microseismic event observations with geomechanical models to minimise the risks of storing CO2 in geological formations. *Earth and Planetary Science Letters*, 305(1-2):143–152.

Verdon, J. P., Kendall, J. M., and Wüstefeld, A. (2009). Imaging fractures and sedimentary fabrics using shear wave splitting measurements made on passive seismic data. *Geophysical Journal International*, 179:1245–1254.

Verdon, J. P. and Wüstefeld, A. (2013). Measurement of the normal/tangential fracture compliance ratio (ZN/ZT) during hydraulic fracture stimulation using S-wave splitting data. *Geophysical Prospecting*, 61(Suppl. 1):461–475.

Vlahovic, G., Elkibbi, M., and Rial, J. A. (2002). Shear-wave splitting and reservoir crack characterization: The Coso geothermal field. *Journal of Volcanology and Geothermal Research*, 120(1-2):123–140.

Vlahovic, G., Elkibbi, M., and Rial, J. A. (2003). Shear-wave splitting and reservoir crack characterization: The Coso geothermal field. *Journal of Volcanology and Geothermal Research*, 120(1-2):123–140.

Walker, A. M. and Wookey, J. (2012). MSAT-A new toolkit for the analysis of elastic and seismic anisotropy. *Computers and Geosciences*, 49:81–90.

Walpole, J., Wookey, J., Kendall, J. M., and Masters, T. G. (2017). Seismic anisotropy and mantle flow below subducting slabs. *Earth and Planetary Science Letters*, 465:155–167.

Walter, M. and Joswig, M. (2008). Seismic monitoring of fracture processes generated by a creeping landslide in the Voralberg Alps. *First Break*, 26(6):131–135.

Watkins, H., Bond, C. E., Healy, D., and Butler, R. W. (2015). Appraisal of fracture sampling methods and a new workflow tocharacterise heterogeneous fracture networks at outcrop. *Journal of Structural Geology*, 72:67–82.

Watkins, H., Healy, D., Bond, C. E., and Butler, R. W. H. (2018). Implications of heterogeneous fracture distribution on reservoir quality; an analogue from the Torridon Group sandstone, Moine Thrust Belt, NW Scotland. *Journal of Structural Geology*, 108:180–197.

Weiss, M. (2008). Techniques for estimating fracture size: A comparison of methods. *International Journal of Rock Mechanics and Mining Sciences*, 45(3):460–466.

Welch, M., Souque, C., Davies, R., and Knipe, R. J. (2015). Using mechanical models to investigate the controls on fracture geometry and distribution in chalk. *Geological Society, London, Special Publications*, 406(1):281–309.

White, J. A. and Foxall, W. (2016). Assessing induced seismicity risk at CO2 storage projects: Recent progress and remaining challenges. *International Journal of Greenhouse Gas Control*, 49:413–424.

Whitmarsh, L., Nash, N., Upham, P., Lloyd, A., Verdon, J. P., and Kendall, J. M. (2015). UK public perceptions of shale gas hydraulic fracturing: The role of audience, message and contextual factors on risk perceptions and policy support. *Applied Energy*, 160:419–430.

Wiart, P. and Oppenheimer, C. (2005). Large magnitude silicic volcanism in north Afar: The Nabro Volcanic Range and Ma'alalta volcano. *Bulletin of Volcanology*, 67(2):99–115.

Wiemer, S. and Wyss, M. (2000). Minimum magnitude of completeness in earthquake catalogs: Examples from Alaska, the Western United States, and Japan. *Bulletin of the Seismological Society of America*, 90(4):859–869.

Wilks, M., Kendall, J. M., Nowacki, A., Biggs, J., Wookey, J., Birhanu, Y., Ayele, A., and Bedada, T. (2017). Seismicity associated with magmatism, faulting and hydrothermal circulation at Aluto Volcano, Main Ethiopian Rift. *Journal of Volcanology and Geothermal Research*, 340:52–67.

Wise, D. (1974). Sub-continental sized fracture systems etched into the topography of New England. In Hodgson, R., Parker Gray, S., and Benjamins, J., editors, *Proceedings of th First*

International Conference on the New Basement Tectonics, pages 416–422, Salt Lake City, Utah. Utah Geological Association.

Worthington, M. (2007). The compliance of macrofractures. *The Leading Edge*, 26(9):1118–1122.

Worthington, M. H. (2000). Fault properties from seismic Q. *Geophysical Journal International*, 143:937–944.

Worthington, M. H. and Lubbe, R. (2007). The scaling of fracture compliance. In Lonergan, L., Jolly, L., Rawnsley, R., and Sanderson, D., editors, *Fractured Reservoirs*, volume 270, pages 73–82. Geological Society of London, London.

Wuestefeld, A., Kendall, J. M., Verdon, J. P., and Van As, A. (2011a). In situ monitoring of rock fracturing using shear wave splitting analysis: An example from a mining setting. *Geophysical Journal International*, 187(2):848–860.

Wuestefeld, A., Verdon, J. P., Kendall, J. M., Rutledge, J., Clarke, H., and Wookey, J. (2011b). Inferring rock fracture evolution during reservoir stimulation from seismic anisotropy. *Geophysics*, 76(6):WC157–WC166.

Xia, J., Falconer, R. A., and Lin, B. (2010). Impact of different tidal renewable energy projects on the hydrodynamic processes in the Severn Estuary, UK. *Ocean Modelling*, 32(1-2):86–104.

Yohannes, E. (2009). Geothermal exploration in Eritrea - Estatus report. In *Short Course IV on Exploration for Geothermal Resources, Lake Naivasha, Kenya, November 1-22, 2009*, pages 1–15, Lake Naivashka, Kenya.

Yohannes, E. (2012). Geothermal Development in Eritrea: A Country Update Ermias. In *Proceedings 4th African Rift Geothermal Conference*, number November, pages 1–8, Nairobi, Kenya.

Yohannes, E. (2013). Geothermal Exploration in Eritrea Status Report and Discussion. In *Short Course VIII on Exploration for Geothermal Resources*, pages 1–15, Lake Bogoria and Lake Naivasha, Kenya.

Yohannes, E. (2015). Geothermal Exploration in Eritrea: Country Update. In *Proceedings World Geothermal Congress*, number April, pages 1–7, Melbourne, Australia.

Yu, C. (2016). *Microseismic Inversion for Anisotropic Velocity Model in Unconventional Reservoirs*. PhD thesis, Freien Universität Berlin.

Zeeb, C., Gomez-Rivas, E., Bons, P. D., and Blum, P. (2013). Evaluation of sampling methods for fracture network characterization using outcrops. *AAPG Bulletin*, 97(9):1545–1566.

Zhang, Q., Wang, Q., Chen, J., Li, Y., and Ruan, Y. (2016). Estimation of mean trace length by setting scanlines in rectangular sampling window. *International Journal of Rock Mechanics and Mining Sciences*, 84:74–79.

Zhang, Y., Wang, G., Jiang, Y., Wang, S., Zhao, H., and Jing, W. (2017). Acoustic emission characteristics and failure mechanism of fractured rock under different loading rates. *Shock and Vibration*, 2017:1–13.

Zhao, J., Turco, R. P., and Toon, O. (1995). A model simulation of Pinatubo volcanic aerosols in the stratosphere. *Journal of Geophysical Research*, 100(D4):7315–7328.

Zoback, M. D., Barton, C. A., Brudy, M., Castillo, D. A., Finkbeiner, T., Grollimund, B. R., Moos, D. B., Peska, P., Ward, C. D., and Wiprut, D. J. (2003). Determination of stress orientation and magnitude in deep wells. *International Journal of Rock Mechanics and Mining Sciences*, 40(7-8):1049–1076.

Zoback, M. L. (1992). First- and second-order patterns of stress in the lithosphere: The World Stress Map Project. *Journal of Geophysical Research*, 97(B8):11703–11728.